Defense Nuclear Agency
Alexandria, VA 22310-3398

DNA-TR-93-4

Numerical Simulation of Shock Interaction with Above-Ground Structures

Joseph D. Baum
Science Applications Intl Corp
P.O. Box 1303
McLean, VA 22102

May 1994

Technical Report

CONTRACT No. DNA 001-89-C-0098

Destroy this report when it is no longer needed. Do not return to sender.

PLEASE NOTIFY THE DEFENSE NUCLEAR AGENCY, ATTN: CSTI, 6801 TELEGRAPH ROAD, ALEXANDRIA, VA 22310-3398, IF YOUR ADDRESS IS INCORRECT, IF YOU WISH IT DELETED FROM THE DISTRIBUTION LIST, OR IF THE ADDRESSEE IS NO LONGER EMPLOYED BY YOUR ORGANIZATION.

DISCLAIMER NOTICE

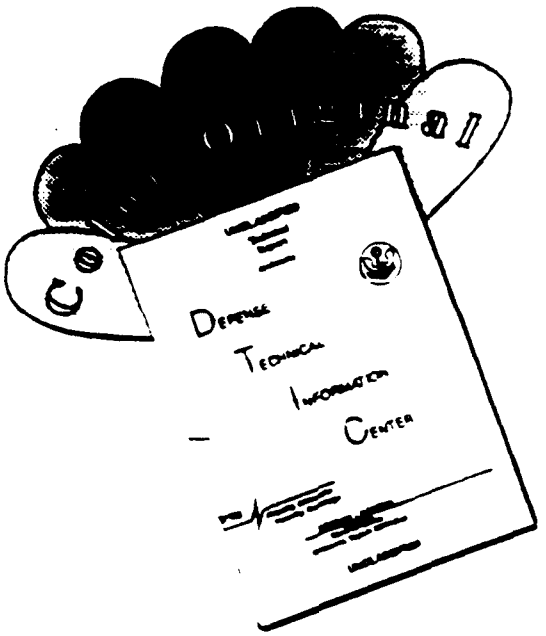

THIS DOCUMENT IS BEST QUALITY AVAILABLE. THE COPY FURNISHED TO DTIC CONTAINED A SIGNIFICANT NUMBER OF COLOR PAGES WHICH DO NOT REPRODUCE LEGIBLY ON BLACK AND WHITE MICROFICHE.

DISTRIBUTION LIST UPDATE

This mailer is provided to enable DNA to maintain current distribution lists for reports. (We would appreciate your providing the requested information.)

NOTE:
Please return the mailing label from the document so that any additions, changes, corrections or deletions can be made easily.

☐ Add the individual listed to your distribution list.

☐ Delete the cited organization/individual.

☐ Change of address.

NAME: _____

ORGANIZATION: _____

OLD ADDRESS	CURRENT ADDRESS
_____	_____
_____	_____
_____	_____

TELEPHONE NUMBER: ( ) _____

DNA PUBLICATION NUMBER/TITLE	CHANGES/DELETIONS/ADDITIONS, etc. *(Attach Sheet if more Space is Required)*
_____	_____
_____	_____
_____	_____

DNA OR OTHER GOVERNMENT CONTRACT NUMBER: _____

CERTIFICATION OF NEED-TO-KNOW BY GOVERNMENT SPONSOR (if other than DNA):

SPONSORING ORGANIZATION: _____

CONTRACTING OFFICER OR REPRESENTATIVE: _____

SIGNATURE: _____

CUT HERE AND RETURN

DEFENSE NUCLEAR AGENCY
ATTN: TITL
6801 TELEGRAPH ROAD
ALEXANDRIA, VA 22310-3398

DEFENSE NUCLEAR AGENCY
ATTN: TITL
6801 TELEGRAPH ROAD
ALEXANDRIA, VA 22310-3398

REPORT DOCUMENTATION PAGE

Form Approved
OMB No. 0704-0188

1. AGENCY USE ONLY (Leave blank)	2. REPORT DATE	3. REPORT TYPE AND DATES COVERED
	940501	Technical 890515 – 921231

4. TITLE AND SUBTITLE
Numerical Simulation of Shock Interaction with Above-Ground Structures

5. FUNDING NUMBERS
C - DNA 001-89-C-0098
PE - 62715H
PR - RS
TA - RC
WU - DH092120

6. AUTHOR(S)
Joseph D. Baum
Rainald Lohner (George Washington University)

7. PERFORMING ORGANIZATION NAME(S) AND ADDRESS(ES)
Science Applications Intl Corp
P.O. Box 1303
McLean, VA 22102

8. PERFORMING ORGANIZATION REPORT NUMBER

9. SPONSORING/MONITORING AGENCY NAME(S) AND ADDRESS(ES)
Defense Nuclear Agency
6801 Telegraph Road
Alexandria, VA 22310-3398
SPSD/Pyle

10. SPONSORING/MONITORING AGENCY REPORT NUMBER
DNA-TR-93-4

11. SUPPLEMENTARY NOTES
This work was sponsored by the Defense Nuclear Agency under RDT&E RMC Code B4694D RS RC 00226 SPSD 4300A 25904D.

12a. DISTRIBUTION/AVAILABILITY STATEMENT
Approved for public release; distribution is unlimited.

12b. DISTRIBUTION CODE

13. ABSTRACT *(Maximum 200 words)*

This final report for DNA contract DNA 001-89-C-0098 for the time period May 15, 1989 to Dec 31, 1992 describes the results of several of the computations conducted under this research effort. The numerical simulations conducted simulated shock wave diffraction phenomenon about complex-geometry two-dimensional and three-dimensional structures. Since a significant part of this effort was composed of parametric studies that have been delivered to the sponsors, the Defense Nuclear Agency and the Air Force Ballistic Missile Organization (BMO), and conducted under the now defunct Rail Garrison project, we included in this report a detailed description of the results of the major computations, and a brief summary of all the repetitive computations.

The final report is divided into three sections. Chapter 1 describes in detail the two-dimensional numerical methodology and typical two-dimensional computation, i.e., the application of the numerical methodology to the simulation of shock interaction with a typical 2-D train (a 2-D cut at the center of a 3-D train). Chapter 2 describes the numerical development of a passive shock reflector, a major effort undertaken in this project. The objective of this effort was to design a passive device that, while allowing the ventilation of the enclosure

14. SUBJECT TERMS

Shock Diffraction
Blast Waves
Adaptive Refinement
Finite Elements Schemes

15. NUMBER OF PAGES
90

16. PRICE CODE

17. SECURITY CLASSIFICATION OF REPORT	18. SECURITY CLASSIFICATION OF THIS PAGE	19. SECURITY CLASSIFICATION OF ABSTRACT	20. LIMITATION OF ABSTRACT
UNCLASSIFIED	UNCLASSIFIED	UNCLASSIFIED	SAR

CLASSIFIED BY:
N/A since Unclassified.

DECLASSIFY ON:
N/A since Unclassified.

7. PERFORMING ORGANIZATION NAME(S) AND ADDRESS(ES) (Continued)

George Washington University
School of Eng & Applied Sciences
2121 I Street NW
Washington, DC 20052

13. ABSTRACT (Continued)

under steady conditions, will prevent blast waves impinging on the wall from entering the enclosure when the structure is impacted by a shock. The passive reflector ("grill") was designed to take advantage of two basic fluid dynamic processes: shock diffraction around sharp corner, and vortex shedding from sharp corners. Finally, Chapter 3 includes a detailed description of a recently developed three-dimensional adaptive shock capturing methodology, and the applications of this methodology under this program to the simulation of shock diffraction around complex-geometry three-dimensional structures, such as a typical modern main battlefield tank, a T-62 tank, and a ballistic missile in flight.

CONVERSION TABLE

U.S. Customary	Conversion Factor	Metric (SI) Unit
Kiloton	4.184	terajoules
foot	3.048 000 times E-1	meter (m)
degree (angle)	1.745 320 times E-2	radian (rad)
pound-force/inch^2 (psi)	6.894 757	kilo pascal (kPa)

TABLE OF CONTENTS

FIGURES

Figure **Page**

FIGURES (Continued)

Figure **Page**

FIGURES (Continued)

Figure **Page**

FIGURES (Continued)

Figure **Page**

SECTION 1
NUMERICAL SIMULATION OF 2-D FLOWS USING A 2-D ADAPTIVE FINITE ELEMENT SCHEME

A transient, two-dimensional, finite-element shock-capturing scheme on unstructured grids was applied to the study of a shock diffracting around a 2-D structure, representing a 2-D cut of a 3-D train, suspended above the rails and a rigid elevated surface. The area between the train and the surface was partially blocked by the rails, resulting in complex shock diffraction processes. The results demonstrate the capability of the developed adaptive refinement/coarsening algorithm to properly adapt to weak shocks, expansions and contact discontinuities, and highlight the resulting excellent resolution of the captured flow features. In addition to interesting shock diffraction and propagation phenomena, the results demonstrate the capability of the new code to capture, and define in great detail, vortex sheets shed from sharp corners. We show that the baroclinic effect, an inviscid process, controls the shedding phenomenon during the diffraction phase. Hence, the Eulerian model is able to correctly predict this process.

1.1 INTRODUCTION.

During the past ten years the CFD community has experienced a proliferation of shock capturing schemes whose ultimate objective is the sharp, *nonoscillatory* capturing of transient shocks, even those that have propagated great distances [1-3]. The practical objective of these methodologies is to predict the loads exerted by shocks, initiated by nuclear or High-Explosive bursts, on stationary or moving structures located a long distance from burst point. The results of such simulations should help improve targeting specification requirements (for offensive purposes) or hardening criteria (for defensive objectives). From the numerical algorithm development point of view, the long propagation times and distances that the shocks are likely to transverse from burst to impact point, pose significantly greater demands than required from traditional shock capturing schemes, which are only intended to produce steady, sharp, nonoscillatory shocks on airfoils, etc. [4-6] to yield the steady lift and drag forces. Past simulations of shock wave propagation over long distances relied on either fixed-mesh structured grid approach [2] or sliding refined zones, intended to continously surround the shocks with a finer mesh than elsewhere in the domain [7]. The first approach yielded coarser, diffused shocks after some propagation distance, since even for two-dimensional calculations it is not economically feasible, even with present day class VI computers, to grid a domain of several hundreds or thousands of meters with 1 cm size cells. The second approach was much more economical, as only part of the domain was finely refined. Nevertheless, the computational resources required for two-dimensional computations (both memory and computational time) were

very high, while three-dimensional computations would have been prohibitively expensive for production-type runs. Hence, the objective of the present effort was a natural evolution of past deficiencies, i.e., develop a numerical scheme capable of dynamically adapting to traveling shocks and other flow discontinuities. This approach allows us to use coarse grid resolution everywhere in the computational domain where flow gradients are low, while applying very fine grid resolution wherever better flow resolution is required. Hence, shocks should always advance into finely refined zones, while grid coarsening should be obtained in areas already traversed by the shocks.

The section will first describe the CFD Methodology employed, starting with the design criteria used for the flow-solver. Thereafter, the adaptive refinement scheme employed is presented, followed by an extensive description of the results obtained for the shock-train case studied. The accent of the section is on the results obtained under the project rather than on the algorithms employed (which were not developed under this effort). Therefore, the exposition of the algorithms is kept to a sufficient, but not exhaustive, depth.

1.2 CFD METHODOLOGY.

The objective of the present effort was to simulate many 2-D and 3-D shock diffraction processes around complex-geometry structures. Thus, the flow solver employed must:

1) Be based on grid systems that can discretize domains of arbitrary complexity;

2) Be able to simulate moving or stationary shocks without spurious overshoots;

3) Be able to allocate in the most efficient manner the degrees of freedom or equivalent computational resources during the course of a simulation. In the present case, these three design criteria are met as follows:

1) In order to discretize domains of arbitrary complexity, *unstructured grids* in conjunction with Finite-Element Methods are used.

2) In order to simulate accurately the strong shocks present in the flowfields, a high-resolution monotonicity-preserving algorithm for unstructured grids is used. The method, called FEM-FCT, is based on Zalesak's [8] generalization of the Flux-Corrected Transport (FCT) algorithms of Boris and Book [9,10] to multidimensional problems.

3) In order to allocate in the most efficient manner the degrees of freedom of the mesh, an efficient adaptive refinement technique for transient problems is employed.

1.2.1 The Flow Solver: FEM-FCT.

As stated above, high-resolution monotonicity-preserving schemes must be developed to simulate the strong nonlinear discontinuities present in the flows under consideration. A number of these schemes have been developed over the last years [4-6,11,12]. The scheme

used here is based on Zalesak's generalization [8] of the 1-D FCT schemes of Boris and Book [9,10]. Parrot and Christie [13] first analyzed FCT schemes in the context of Finite Element Methods, and Löhner et al. [14,15] extended these ideas further to include the solution of systems of equations and the consistent-mass matrix that yields high temporal accuracy.

Consider a set of conservation laws given by a system of partial differential equations of the form

$$\frac{\partial U}{\partial t} + \frac{\partial F_a^i}{\partial x^i} = \frac{\partial F_v^i}{\partial x^i}, \tag{1.1}$$

where the advective fluxes $F_a = F_a(U)$ dominate the viscous fluxes $F_v = F_v(U)$. For flows described by Eq. 1.1, discontinuities in the variables may arise (e.g., shocks or contact discontinuities). Any numerical scheme of order higher than unity will produce overshoots or ripples at such discontinuities (the so-called Godunov theorem). Very often, particularly for mildly nonlinear systems, these overshoots can be tolerated. However, for the class of problems studied here, overshoots will eventually lead to numerical instability, and will therefore have to be suppressed.

The FCT algorithm combines a high-order scheme with a low-order scheme in such a way that in regions where the variables under consideration vary smoothly (so that a Taylor expansion makes sense) the high-order scheme is used, whereas in those regions where the variables vary abruptly, the low-order scheme is favored.

The temporal discretization of Eq. 1.1 yields

$$U^{n+1} = U^n + \Delta U, \tag{1.2}$$

where ΔU is the increment of the unknowns obtained for a given scheme at time $t = t^n$. Our aim is to obtain a ΔU of as high an order as possible without introducing overshoots. To this end, we rewrite Eq. 1.2 as

$$U^{n+1} = U^n + \Delta U^l + (\Delta U^h - \Delta U^l), \tag{1.3}$$

or

$$U^{n+1} = U^l + (\Delta U^h - \Delta U^l). \tag{1.4}$$

Here ΔU^h and ΔU^l denote the increments obtained by some high- or low-order scheme, whereas U^l is the (ripple-free) solution at time $t = t^{n+1}$ of the low-order scheme. The idea behind FCT is to limit the second term on the right side of Eq. 1.4:

$$U^{n+1} = U^l + lim(\Delta U^h - \Delta U^l), \tag{1.5}$$

in such a way that no new overshoots or undershoots are created. In addition, strict conservation on the discrete level must be maintained. The simplest way to guarantee strict conservation for node-centered schemes (only these are considered here) is by constructing schemes for which the sum of the contributions of each individual element (cell) to its surrounding nodes vanishes ("all that comes in goes out"). This means that the limiting process (Eq. 1.5) will have to be carried out in the elements (cells). Further details may be found in References 14 and 15.

1.2.2 Transient Adaptive Refinement.

A very attractive feature of schemes based on unstructured grids is the ease with which they incorporate adaptive refinement. The addition of further degrees of freedom does not destroy any previous structure. Thus, the flow solver requires no further modifications when operating on an adapted grid. For many practical problems, the regions that need to be refined are extremely small compared with the overall computational domain. Therefore, storage and CPU requirements are typically reduced by a factor of 10 to 100 when compared to an overall fine-resolution fixed mesh [16-22]. It has been our experience that, for production runs, adaptive refinement has been the crucial element necessary to perform simulations at an acceptable level of accuracy in a reasonable amount of time. The simulation presented in this section is a typical example of such runs.

Several authors have studied adaptive refinement schemes [7,16,23-25]. When developing an efficient adaptation methodology for transient problems, further constraints have to be considered: a) The method must be conservative, i.e., a mesh change should not result in the production or loss of mass, momentum or energy, as this will produce erroneous shock propagation speed or will diffuse shocks or contact-discontinuities; b) The method should not produce elements that are too small, as this will significantly reduce the allowable time step of the explicit flow solver; c) The method must be fast, as the grid is modified many times during the computation. In particular, it should lend itself to some degree of parallelism; and d) The method must not be memory (storage) intensive.

These constraints are met by: a) Applying strict conservation on the discrete level and conducting the limiting process of FCT on the elements; b) Using classical h-enrichment/coarsening, as it does not require a major storage overhead and, due to its simplicity, lends itself easily to vectorization; c) Allowing only one level of refinement/coarsening per mesh change in order to minimize the logic involved and thus CPU requirements, and d) Avoiding successive subdivision of a triangle into two.

1.2.3 Grid Logic.

When constructing the algorithm to refine or coarsen the grid, one faces the usual decision of speed versus storage. The more information from the previous grid is stored, the faster the new grid may be constructed. As storage requirement minimization was one of the goals of the present research, we tried to keep only the essential information needed between mesh changes without sacrificing an excessive amount of CPU time. In the present case, six integer locations per element are kept in order to identify the "parent" and "son" elements of any element.

The first three integers store the new three neighbor elements ("sons") of an element that has been subdivided into four (the center element of the four is kept as "parent"). If the element has been subdivided into two elements, the neighbor element is stored in the first integer, whereas the remaining second and third integer locations for this element are set to zero.

The element from which the present element originated (the parent element) is stored in the fourth integer. If the parent element has been subdivided into two, the negative parent element number is stored, allowing the distinction between the 1:2 and 1:4 refinement cases.

The fifth integer denotes the local side of the parent element from which this element came.

Finally, in the sixth integer location the refinement level is remembered. These six integer locations per element are sufficient to construct further refinements or to reconstruct the original grid.

1.2.4 Error Indicator.

Many possible error indicators have been suggested in the literature [15-19, 23-25]. Numerical experience indicates that all perform similarly. However, the following requirements must be met for the present application: a) The error indicator must be fast; b) The error indicator should be dimensionless, so that more than one 'key-variable' [19] can be monitored simultaneously; c) To be applicable to a large class of problems, the error estimator should be bounded (independent of the solution), so that preset refinement/coarsening tolerances can be employed; d) As the feature may move only very slowly or come to a standstill (e.g., a shock entering a very dense region), the error indicator must also be reliable for steady state applications; and e) The error indicator should mark for refinement not only regions with strong shocks, but also regions of weak shocks, contact discontinuities and other weak features in the flow.

A classic interpolation estimates [19] used for steady state computations [20-22] has

been modified to meet these requirements. These estimators make use of an appropriate seminorm for the detection of those regions needing further refinement or coarsening, e.g., the H2-seminorm [16,20-22,24,25]

$$\|u - u^h\|_0 \leq c \cdot h^2 \cdot |u|_2, \tag{1.6}$$

where u denotes the exact and u^h the approximate solution, c is a mesh-size independent constant, h is the characteristic mesh size, and

$$|u|_2 = \sqrt{\int_\Omega \sum_{i,j} \left[\frac{\partial^2 u}{\partial x^i \partial x^j}\right]^2 d\Omega}. \tag{1.7}$$

Second derivatives are justified here because the shape functions used in the finite element discretization are linear. Numerically, the second derivatives at the nodes are evaluated first via a variational statement the integral (7) is approximated conservatively by evaluating for each element the maximum second derivative at the associated nodes. For linear elements of constant length h in 1-D, one obtains for the first step at the nodes:

$$e_I = h^{-2} \cdot |U_{I+1} - 2 \cdot U_I + U_{I-1}|. \tag{1.8}$$

This error indicator is dimensional, and thus is not bounded a priori. A major defect noted in numerical experiments was that this error indicator tends to favor strong shocks. This results from the fact that second derivatives of a key variable u were utilized. Since the objective of the present study is to develop a methodology that accurately simulates weak shocks and contact discontinuities, the interpolation theory error indicator given by Eq. (1.8) was modified as follows:

$$E_I = \frac{|U_{I+1} - 2 \cdot U_I + U_{I-1}|}{|U_{I+1} - U_I| + |U_I - U_{I-1}| + \theta} \tag{1.9}$$

where

$$\theta = \epsilon \left[|U_{I+1}| + 2 \cdot |U_I| + |U_{I-1}|\right].$$

Dividing the second derivatives by the absolute value of the first derivatives yields an error indicator that is bounded ($0 \leq E_I < 1$), dimensionless, and prevents the eating up effect of strong shocks. In addition, the non-dimensional error indicator permits the use of several critical parameters simultaneously. Thus, it is possible to use both density and vorticity for problems requiring the simultaneous tracking of shocks and vortices. The

terms following ϵ in Eq. 1.9 are added as a noise filter in order not to refine wiggles or ripples that appear due to loss of monotonicity. The value for ϵ thus depends on the algorithm chosen to solve the PDEs that model the physical process investigated. The multidimensional form of this error indicator is given by

$$E^I = \sqrt{\frac{\sum_{k,l}(\int_\Omega N^I_{,k} N^J_{,l} d\Omega \cdot U_J)^2}{\sum_{k,l}(\int_\Omega |N^I_{,k}| \left[|N^J_{,l} U_J| + \epsilon \left(|N^J_{,l}||U_J|\right)\right] d\Omega)^2}}, \tag{1.10}$$

where N^I denotes the shape-function of node I.

After the values of the error indicators in the elements are determined, all elements lying above a preset threshold value are refined, while all elements lying below a preset threshold value are coarsened.

1.3 RESULTS.

The transient, two-dimensional, finite-element shock-capturing scheme on unstructured grids described above was applied in this research effort to the study of a shock interacting with a train suspended above a rigid elevated surface. The area between the train and the surface was partially blocked by the rails.

Figures 1-1 through 1-11 show combinations of computational mesh, grid refinement levels, pressure, density, vorticity and Mach number contours at several times. The grid was adapted every seven time steps. Density was chosen as the key variable for the error indicator. The incident weak shock travels from left to right, with a shock Mach number of 1.3. The color contour plots presented used 256 contours, with blue representing the lowest value and magenta the highest. With respect to the mesh refinement procedure, one level of mesh refinement is defined as the division of a triangle into four, performed by connecting the mid-faces. The color designations for the mesh refinement levels are blue for the original grid, and green, yellow, red, magenta, and cyan for one, two, three, four, and five refinement levels, respectively. Two parameters control mesh refinement: a) the maximum number of refinement levels desired (five levels for this example), and b) the minimum normal height allowed below which the grid may not be further refined. Thus, near the train where the original grid has fine resolution, only two or three refinement levels were obtained. Conversely, five refinement levels will be obtained at zones of coarse initial grid, such as far above the train.

Figure 1-1 shows the mesh, mesh refinement levels, and pressure contours for the complete computational domain and for an expanded view around the train at t=0. A highly refined mesh was obtained only in the immediate vicinity of the shock. These figures indicate the futility of any attempt to grid such a computational domain, which is several hundred meters in each direction, with a uniform fine resolution grid that will yield captured shock wave thickness of less than 0.6 cm (about the average shock thickness obtained in this computation).

A regular Mach reflection from the ramp is observed at t=0.4 (Figure 1-2). The well resolved slip line (shown in the density data, Figure 1-2b) demonstrates one of the advantages of employing density rather than pressure as the critical refinement parameter. A comparison of the predicted pressure values behind the Mach stem with available experimental data showed very good agreement. The incident shock hits the train at t=0.46.

The solution around the complete train at t=0.6 (Figure 1-3) shows a curved shock reflection from the top-upstream corner of the train, followed closely by an expansion fan. An expanded view of pressure contours near the bottom of the train at t=0.5 (Figure 1-4a) shows the non-perturbed incident shock (shock 1a), the main shock reflection from the upstream surface of the train (shock 1), the rarefaction waves expanded from the upstream bottom corner of the train (wave 5) and the upstream top corner of the elevation (wave 4) after the main shock passage, the reflected ramp shock (shock 2), and the curved Mach stem (shock 3) that was further weakened by the interaction with the rarefaction wave 4. The expanded view under the train at t=0.6 (Figure 1-4b), shows the primary reflected shock from the train (shock 1), its reflection from the top of the elevation (shock 1a); the rarefaction wave centered at the upstream bottom corner of the train (wave 5); the reflected ramp (shock 2), its reflection from the train (shock 2a), and the rarefaction wave produced upon the impact of this wave on the train's upstream bottom corner (wave 2b); the incident Mach stem under the train (shock 3); and the expansion wave (wave 4) centered at the upstream corner of the ramp.

A comparison of the adapted mesh and mesh refinement levels at t=0.8 (Figures 1-5a and 1-5b) with the pressure results (Figure 1-5c) demonstrates the ability of the grid adaptation routine to adapt to all density gradients. Due to the initially finer grid under the train, only three refinement levels were obtained there. In contrast, five refinement levels were observed away from the train, where the initial grid was fairly coarse. The pressure results at this time indicate that the shock diffraction over the top upstream curved corner of the train produced a triple point connecting the incident shock, a Mach stem, and a curved reflected shock (Figure 1-5c). Ramp shock reflection (shock 2 in Figure 1-4b) from the front surface of the train formed a high-amplitude Mach stem traversing the front surface of the train.

Complex flow processes were observed under the train. Examination of the expanded views under the train at t=0.7 (Figure 1-4c) and t=0.8 (Figure 1-4d) show many interesting shock diffraction processes. At t=0.7, the incident Mach stem has just cleared the upstream support beam (shock 1). The reflection of the incident shock from the beam has propagated upstream (shock 3 at t=0.7 and shock 1a at t=0.8) and, due to its curvature, partially reflected from the bottom of the train (shock 1b at t=0.8). The diffracted incident Mach stem (shock 1) downstream of the beam has impacted on the top of the elevation at t=0.7, and was reflected as shock 3 at t=0.8. Immediately behind it, and partially merged, is shock 2d, which is the transmitted part (across the beam) of shock 2a at t=0.6. The ramp shock and its reflection from the train (shocks 2 and 2a in Figure 1-4b) are shocks 2 and 2a; the expanding rarefaction waves 2b and 5 at t=0.6 (Figure 1-4b) are waves 2b and 5 at t=0.7, and waves 2c and 2b, respectively, at t=0.8; the reflection of the main shock (shock 1 in Figure 1-4b) from the top of the elevation is shock 1a at t=0.7, and 7a at t=0.8, while the reflection of shock 2a at t=0.6 (which is the reflection of the reflected ramp shock from the train) is shock 2c at t=0.7, and shock 7b at t=0.8. The evolution of these shocks is important in determining the vibrations on the train. Shock 1a at t=0.7 has partially reflected from the upstream beam (shock 5 at t=0.8, which has also reflected from the bottom of the train as shock 5a), and partially transmitted as shock 4 at t=0.8, which has reflected from both the bottom of the train (shock 4a) and the top of the elevation (shock 4b). Similarly, shock 2c has expanded up and downsteam (shock 6), and reflected from the bottom of the train (shock 6a). The low pressure zone near the top of the beam indicates a high velocity zone created as a result of flow acceleration around the top of the beam and the attached vortex sheet, which has just begun its roll-up process.

While the incident shock continued propagating above the train, the triple point height grew linearly with time, and the circular expansion waves from both the bottom and top upstream corners also continued growing linearly with time (Figures 1-3, 1-5c, 1-6a and 1-7c), the most interesting shock evolution processes occurred under the train. Examination of the pressure contour results under the train at t=0.9 (Figure 1-4e) and t=1.0 (Figure 1-4f) shows the virtual separation of the shock system between the support beams and the reflected shocks upsteam of the beams; a separation resulting from the growing vortex near the upstream support beam which will accelerate and break any approaching shock. The leading shock (shock 1) has been completely merged with shock 4 at t=0.8. Meanwhile, we observe the formation and rise of the triple point between shocks 1 and 3, and Mach stem 1m. Shock 3 resulted from the merging of shocks 3 and 4b at t=0.8, an almost completed merger as two shocks are observed to reflect from the bottom of the train at t=0.9 (shocks 3a and 4b). Nevertheless, a single reflected shock is observed after the shocks were reflected again from the top of the elevation (t=1.0). Another shock system observed between the support beams are shock 6 (at t=0.9), which evolved from shock 6a at t=0.8,

and its reflection from the top of the elevation, shock 6a (t=1.0)

Shock wave reflection upstream is characterized both by shock wave reverberation between the bottom of the train and the top of the elevation and shock interaction with the vortex emanating from the upstream bottom corner of the train. As an example we point to shock 1b at t=0.8 (which has just reflected from the bottom of the train), propagating down, and reflecting from the top of the elevation as shock 1c (t=0.9), and reflecting again from the bottom of the train as shock 1d (t=1.0). Similar reflection pattern was observed for shock 5a.

Typical shock-vortex interaction can be observed in Figures 1-4e and 1-4f (t=0.9 and 1.0, respectively). The reflection of the curved shock 1a from the bottom of the train (shock 1b) resulted in the formation of a triple point, with increased height from the surface. At t=0.82, the Mach stem near the surface and the two shocks (shock 1a and 1b) interact with the vortex attached to the upstream bottom corner of the train. The result is an acceleration and diffusion of the shock near the surface of the train; both effects decrease with increased distance from the surface. These processes result in the upstream acceleration and diffusion of compression wave 1d between t=0.8 and t=1.0. The next shock wave system, shocks 5 and 5a, experience similar though weaker processes, perhaps due to the weakening of the vortex.

The very low pressure zone near the upstream support beam indicates the rapid roll-up of a vortex sheet anchored at the top-upstream corner of the beam (Figure 1-5c and Figures 1-4e through 1-4i). The vortex roll-up process was enhanced by vortex interaction with the system of curved reflected shocks reverberating between the bottom of the train and the top of the elevation. A much weaker vortex sheet has also been formed near the upstream bottom corner of the train. Mach number results at t=0.8 and later (Figures 1-6b and 1-6d at t=1.0 and t=1.2, respectively) demonstrate strong flow acceleration due to the vortex roll-up and the reduction of the effective flow area between the top of the elevation and the bottom of the train, with the highest velocities above the inner-most vortex.

Since vortex dynamics is a phenomenon normally associated with viscous flow processes, while the present numerical scheme only solves the Euler equations, the source of this vorticity deserves further discussion.

Vorticity production, as modeled in the Bjerknes Theorem [26], incorporates both viscous and inviscid contributions, and is expressed as:

$$\frac{D\vec{\xi}}{Dt} = -\nabla\left(\frac{1}{\rho}\right) \times \nabla P + \nu\nabla^2\vec{\xi}, \tag{1.11}$$

where $\vec{\xi}$ = Vorticity; ν = Kinematic Viscosity; p= Pressure; and ρ= Density. A time-scale and order-of-magnitude analysis of these terms indicates that the current vorticity production is controlled by the baroclinic effect (i.e., the first term in the equation, which represents the non-alignment of pressure and density gradients), and thus can be predicted by the inviscid code. Laser-schilieren shadowgraph data produced in a similar shock-train interaction experiment conducted using a sub-scale model in a shock tube facility demonstrated vortex sheet roll-up within a few microseconds after the shock diffracted around the corner, a time period too short for viscous processes to significantly affect the flow. The numerical predictions for this experiment were in excellent agreement with the experimental data. Due to lack of space they will be presented in a future publication.

The incident shock propagated past the downstream support beam at t=1.03. Results at t=1.1 and t=1.2 (Figures 1-4g and 1-4h, respectively) show that similar to the shock diffraction process over the upstream beam (Figure 1-4d at t=0.8), incident shock diffraction around the downstream beam resulted in the formation of curved diffracted and reflected shocks; shocks 1 and 1a are the transmitted shock wave and its reflection from the top of the elevation, respectively, while shocks 2 and 2a are the reflected shock and its reflection from the bottom of the train. The merged shock formed of shocks 3 and 6 (at t=1.0) has been partially transmitted as shock 6 (t=1.1) and was later reflected from the top of the elevation as shock 6c (t=1.2), and partially reflected from the beam as shock 6d (at t=1.1 and t=1.2). Shocks 4 and 6a at t=1.0 continued to reverberate and produce shocks 4, 6a and 6b at t=1.1, and shocks 4, 4a and 4b (beam reflection), and 6b at t=1.2. The vorticity contour plots, Figures 1-6c and 1-6e, at t=1.0 and t=1.2, respectively, indicate significant enhancement of the rolled-up vortex sheet behind the upstream beam due to the interaction with the family of curved reflected shocks, and the initiation of a vortex sheet behind the downstream beam.

The successful continued grid adaptation is demonstrated again at t=1.4. A comparison of the computational grid (Figure 1-7a), grid refinement level (Figure 1-7b), and pressure, Mach number and vorticity contours (Figures 1-7c, 1-7d and 1-7e, respectively) demonstrate the ability of the new methodology to adapt to both strong and weak density gradients.

The shocks that propagated under the train emerged at t=1.22. The higher stagnation pressure under the train resulted in faster propagation speed than above, and thus the incident shock propagating below has emerged a short time earlier. Pressure results at t=1.4 (Figure 1-4i) indicate that four primary shocks emerged: the incident shock (shock 1); its reflection from the top of the elevation (shock 1a); shock 6c; and shock 6, which has been weakened by its upward expansion and broken due to its interaction with the stronger shocks 1a and 6c. The expansion of these shocks around the bottom downstream corner of

the train and the corner of the elevation resulted in the immediate formation of a counter-clockwise rotating vortex sheet anchored at the corner and a cylindrical expansion wave. The bottom-produced expansion could not propagate upstream beyond the downstream beam, due to the transonic flow between the beam and the bottom of the train.

Among the upstream reflected shocks observed are the primary reflection from the train upstream surface, reflections of the Mach stem from the train, and several shock reflections from the upstream support beam. The system of shocks between the beams continued reverberating and producing new shocks. The interactions between these curved shocks with the rolled-up vortex attached to the upstream beam resulted in the break-up of this sheet, as observed at t=1.4 (Figure 1-7e) and t=1.6 (Figure 1-8a).

Figure 1-8 shows vorticity contours at several times. While vorticity production was fairly low for shock diffraction over the rounded *upper* downstream corner of the train, the system of shock waves reverberating between the support beams and between the top of the elevation and the bottom of the train both enhanced and broke up the rolled-up vortices attached to the support beams, as shown in Figures 1-8a, 1-8b, 1-8c, 1-8d and 1-8e at t=1.6, 1.8, 2.0, 2.2 and 2.4, respectively. Meanwhile, the vortices attached to the bottom corners of the train continued their roll-up process; the one attached to the downstream corner rolled up about four times at t=2.4 (Figure 1-8e).

The shocks diffracting around the downstream side of the train interacted with the opposite corners at t=2.6. The computational grid, the grid adaptation levels, and the pressure and Mach number contour results at t=2.4 (Figures 1-9a through 1-9d) demonstrate the excellent shock adaptation capabilities of the developed methodology, even after propagating long distances. The large disparity between the long shock propagation distance and the small size of the resolved vortices or the captured shocks thickness clearly demonstrates the economical advantage of applying an adaptive refinement/coarsening scheme as compared to a fixed-mesh scheme.

The shock that has diffracted over the top interacted at t=2.6 with the vortex sheet anchored at the bottom downstream corner (Figure 1-8f). Since this curved diffracted shock carried vorticity of opposite sign and of about equal magnitude to the vorticity of the attached vortex sheet, the interaction caused the eventual detachment of the vortex sheet from the corner and its downstream convection. Flow area constriction due to the vortices shed from both the upstream and downstream beams (Figures 1-7d and 1-9d) resulted in flow acceleration to supersonic velocities, specifically, downstream of the downstream beam (M=1.28). The instantaneous local flow area expansion near the downstream bottom corner of the train resulted in the formation of a normal shock attached to that corner, and a deceleration to M=0.65. Further downstream, effective flow-area constriction between the vortex attached to this corner and the vortex attached to the downstream beam accelerated

the flow to M=1.2, which was further followed by an oblique shock as the effective flow-area increased again.

The downward-propagating shock downstream of the train hit the bottom bevel at t=3.1 and reflected upward. Meanwhile, the shock that emerged from under the train continued its downstream-and-up propagation, though shock propagation upward was inhibited by the transonic flow above the train. This blockage effect temporarily trapped a relatively high pressure zone downstream of the train, which could not be relieved through the channel under the train due to the transonic flow in this zone. Meanwhile, the vortices shed from the downstream beam and bottom corner were convected downstream by the flow, as shown in Figures 1-8g, 1-8h, 1-8i, 1-8j and 1-8k, at t=3.2, 3.6, 4.2, 5.0 and 6.0, respectively. These results also show the break-up of the vortex sheet attached to downstream beam, the roll-up of the broken sheet into a weak, clockwise-rotating vortex (Figure 1-8h), and the rolling of the pair of counter-rotating vortices by the flow (Figures 1-8i, 1-8j and 1-8k).

The computation was continued to t=8.0, long after the system of shocks cleared the train. At this time the flow above the train was still transonic after reaching a maximum Mach number of $M = 1.35$ at t=4.5. Thus, the upward propagation of the shock reflected from the downstream bevel was delayed, and its influence was still felt on the top of the train at t=6.0 (Figure 1-10). All shocks had propagated very long distances, but were still captured as sharp, nonoscillatory discontinuities. The captured shocks' thickness has not changed over the past several thousand steps, as all shocks were still captured over two to three elements, while the element size around the shock has not changed due to the adaptive procedure. These results demonstrate, at least for the present application, the advantage of adaptive-mesh schemes over fixed-grid schemes. Achieving similar shock resolution with a fixed-mesh methodology would have required maintaining a fine grid virtually everywhere in the computational domain, at a significantly (perhaps prohibitively) higher computational cost. Grid refinement was observed as the shocks propagated into new areas, while grid coarsening was observed in areas already traversed by the shocks. Finally, it should be noted that the solution obtained above the train at later times indicates a compression wave rather than a shock. This is the correct physical solution as the initial reflected shock above the train (Figure 1-5a at t=1.0 and Figure 1-7a at t=1.4) was significantly weakened by the strong expansion over the train (Figure 1-9c at t=2.4). Results obtained in other simulations using significantly stronger shocks demonstrated a reflected shock above the train, even at very late times.

Comparisons of experimental pressure and impulse time histories and the corresponding numerical predictions are shown in Figures 1-11 at selected stations around the train. Stations **a** and **b** were located on the upstream surface of the train, station **c** on top,

stations **d** and **e** on the downstream surface and stations **f** and **g** on the bottom. The experimental data were obtained in a large shock tube facility. Since the experimental model spanned a significant portion of the width of the shock tube, it was appropriate to model this flow with a two-dimensional algorithm. The numerical pressure-time histories and impulses (temporally integrated pressures) are shown as thicker lines to t=8.0. The experimental pressure and impulse data are shown in thinner lines to t=10.0. Very good agreement is demonstrated at all locations. Physical processes controlled by shock physics were predicted extremely well. For instance, very good agreement is demonstrated between the predicted and measured pressure-time histories at stations six and seven, located under the train; these stations exhibit a multi-shock system that resulted from the repetitive shock reflection from the top of the elevation, the support beams, and the bottom of the train. In contrast, the late-time experimental data (well past the diffraction phase) for stations on the train top and back indicate periodic 3-D vortex shedding, a physical process that cannot be properly modeled by the present 2-D model.

A final note relating to the computational performance of the code: computation time for approximately 6800 time steps consumed approximately six hours of CPU time on a Cray 2/8-128 computer (single processor). Computation time was approximately 60 microseconds per node per time step.

1.4 SUMMARY AND CONCLUSIONS.

A new transient, two-dimensional, finite-element shock capturing scheme on unstructured grids was applied to the study of shock interaction with a train suspended above a rigid elevated surface. The area between the train and the surface was partially blocked by the train support beams, resulting in complex shock diffraction processes. The results demonstrate the ability of the new adaptive refinement/coarsening algorithm to resolve shocks in a sharp-nonoscillatory manner. In addition to interesting shock wave propagation and interaction processes, the results demonstrate the capability of the new code to capture, and define in great detail, vortices shed from sharp corners.

Among the more interesting shock propagation processes observed were shock diffraction around sharp corners and the immediate formation of vortices, no doubt due to the baroclinic effect; interaction of diffracted curved shocks with vortex sheets carrying vorticity of identical or opposite sign, resulting in either vortex enhancement or break-up; containment of the high pressure zone (i.e., blockage of upward propagation of shocks) on the downstream side of the train by the supersonic/transonic flow above the train; and the blockage of the upstream propagation of the rarefaction wave in the channel under the train due to the transonic flow above the downstream support beam.

1.5 REFERENCES.

[1] P. Woodward and P. Colella - The Numerical Simulation of Two-Dimensional Fluid Flow with Strong Shocks; *J. Comp. Phys.* 54, 115-173 (1984).

[2] H.M. Glaz, P. Colella, I.I. Glass and R.L. Deschambault - A Numerical Study of Oblique Shock-Wave Reflections with Experimental Comparisons; *Proc. Roy. Soc. Lond.* A 398, 117-140 (1985).

[3] M. Fry, J. Tittsworth, A. Kuhl, D.L. Book, J.P. Boris and M. Picone - Transport Algorithms with Adaptive Gridding; *Proc. 13th Int. Symp. on Shock Tubes and Waves* (C.E. Treanor and J.G. Hall eds.), 376-384 (1982).

[4] P.L. Roe - Approximate Riemann Solvers, Parameter Vectors and Difference Schemes; *J. Comp. Phys.* 43, 357-372 (1981).

[5] A. Harten - High Resolution Schemes for Hyperbolic Conservation Laws; *J. Comp. Phys.* 49, 357-393 (1983).

[6] P.K. Sweby - High Resolution Schemes Using Flux Limiters for Hyperbolic Conservation Laws; *SIAM J. Num. Anal.* 21, 995-1011 (1984).

[7] M.J. Berger and J. Oliger - Adaptive Mesh Refinement for Hyperbolic Partial Differential Equations; *J. Comp. Phys.* 53, 484-512 (1984).

[8] S.T. Zalesak - Fully Multidimensional Flux-Corrected Transport Algorithm for Fluids; *J. Comp. Phys.* 31, 335-362 (1979).

[9] J.P. Boris and D.L. Book - Flux-corrected Transport. I. SHASTA, a Transport Algorithm that works; *J. Comp. Phys.* 11, 38 (1973).

[10] J.P. Boris and D.L. Book - Flux-corrected Transport. III. Minimal-Error FCT Algorithms; *J. Comp. Phys.* 20, 397-431 (1976).

[11] H. Paillere and K. Powel - A Wave-Model-Based Refinement Criterion for Adaptive-Grid Computation of Compressible Flows; AIAA-92-0322 (1992).

[12] I. Parpia and D. Michalek - A Nearly Monotone Genuinely Multidimensional Scheme for the Euler Equations; AIAA-92-0325 (1992).

[13] A.K. Parrott and M.A. Christie - FCT Applied to the 2-D Finite Element Solution of Tracer Transport by Single Phase Flow in a Porous Medium; *Proceedings of the ICFD-Conf. on Numerical Methods in Fluid Dynamics*, Reading, Academic Press, 1986.

[14] R. Löhner, K. Morgan, M. Vahdati, J.P. Boris and D.L. Book - FEM-FCT: Combining Unstructured Grids with High Resolution; *Comm. Appl. Num. Meth.* 4, 717-730 (1988).

[15] R. Löhner, K. Morgan, J. Peraire and M. Vahdati - Finite Element Flux-Corrected Transport (FEM-FCT) for the Euler and Navier-Stokes Equations; *Int. J. Num. Meth. Fluids* 7, 1093-1109 (1987).

[16] I. Babuska et.al. (eds.) - *Accuracy Estimates and Adaptive Refinements in Finite Element Computations*; J. Wiley and Sons (1986).

[17] B. Palmerio and A. Dervieux - Application of a FEM Moving Node Adaptive Method to Accurate Shock Capturing; *Proc. First Int. Conf. on Numerical Grid Generation in CFD*, Landshut, W. Germany (1986).

[18] W. Schönauer, K. Raith and K. Glotz - The Principle of Difference Quotients as a Key to the Self-Adaptive Solution of Nonlinear Partial Differential Equations; *Comp. Meth. Appl. Mech. Eng.* 28, 327-359 (1981).

[19] J.F. Dannenhoffer and J.R. Baron - Robust Grid adaptation for Complex Transonic Flows; AIAA-86-0495 (1986).

[20] R. Löhner, K. Morgan and O.C. Zienkiewicz - An Adaptive Finite Element Procedure for High Speed Flows; *Comp. Meth. Appl. Mech. Eng.* 51, 441-465 (1985).

[21] R. Löhner and K. Morgan - Improved Adaptive Refinement Strategies for Finite Element Aerodynamic Computations; AIAA-86-499 (1986).

[22] J. Peraire, M. Vahdati, K. Morgan and O.C. Zienkiewicz - Adaptive Remeshing for Compressible Flow Computations; *J. Comp. Phys.* 72, 449-466 (1987).

[23] M.D. Smooke and M.L. Koszykowsky - Two-Dimensional Fully Adaptive Solutions of Solid-Solid Alloying Reactions; *J. Comp. Phys.* 62, 1-25 (1986).

[24] J.T. Oden, P. Devloo and T. Strouboulis - Adaptive Finite Element Methods for the Analysis of Inviscid Compressible Flow: I. Fast Refinement/Unrefinement and Moving Mesh Methods for Unstructured Meshes; *Comp. Math. Appl. Mech. Eng.* 59, 327-362 (1986).

[25] R. Löhner - An Adaptive Finite Element Scheme for Transient Problems in CFD; *Comp. Meth. Appl. Mech. Eng.* 61, 323-338 (1987).

[26] V. Bjerknes, J. Bjerknes, T. Bergeron and H. Solberg - *Physikalische Hydrodynamik*, Springer Verlag, Berlin, 1933.

SECTION 2
NUMERICAL DESIGN OF A PASSIVE SHOCK REFLECTOR

A recently developed transient, two-dimensional finite-element shock-capturing scheme on unstructured grids, was applied to the study of a shock interacting with a passive shock reflector placed at an opening of a vented enclosure. The objective of this effort was to design a passive device that, while allowing the ventilation of the enclosure under steady conditions, will prevent blast-waves impinging on the wall from entering the enclosure when the structure is impacted by a shock. A passive reflector ("grill") was designed to take advantage of two basic fluid dynamic processes: shock diffraction around sharp corners, and vortex shedding from sharp corners. As the shock propagated through the grill, shock diffraction around several corners resulted in an order-of-magnitude shock amplitude reduction, while transforming the steep-fronted shock into a compression wave. The vortex shedding process significantly reduced the effective flow area, and limited the quasi-steady flow behind the shock from entering the enclosure. From the numerical point of view, the results demonstrate the capability of the developed adaptive refinement/coarsening algorithm to properly adapt to weak shocks, rarefaction waves and other weak flow gradients, and the resultant excellent resolution of the captured flow features. In addition to interesting shock diffraction and propagation phenomena, the results demonstrate the capability of the new code to capture, and define in great detail, vortex sheets shed from sharp corners. Finally, the results demonstrate that when a design project is based on the understanding and application of basic fluid-dynamic mechanisms, it is possible to obtain significant improvements in performance, specifically, an order-of-magnitude reduction of shock amplitude entering the enclosure.

2.1 INTRODUCTION.

During the past ten years, the CFD community has experienced a proliferation of a multitude of shock capturing schemes whose ultimate objective is the sharp, nonoscillatory capturing of transient shocks, even after propagating long distances [1-3]. The practical objective of these methodologies is to predict the loads exerted by shocks, initiated by nuclear or High-Explosive (HE) bursts, on stationary or moving structures located a long distance from the burst point. The results of such simulations should help improve targeting specification requirements (for offensive purposes) or hardening criteria (for defensive objectives). From the numerical algorithm development point of view, the large propagation times and distances that the shocks are likely to traverse from burst to impact point pose significantly greater demands than required from traditional shock capturing schemes. These schemes are only intended to produce steady, sharp, nonoscillatory shocks

on airfoils, etc. [7] to yield the steady lift and drag forces. Past simulations of shock wave propagation over long distances relied on either the fixed-mesh structured grid approach [1,2] or sliding refined zones [20], intended to continuously surround the shocks with a finer mesh than elsewhere in the domain. The first approach yielded coarser, diffused shocks after some propagation distance, since even for two-dimensional calculations it is not economically feasible, even with present day class VI computers, to grid a domain of several hundreds or thousands of meters with *1 cm size cell.* Worse yet, in this investigation it is necessary to compute flow diffraction around a grill with small gaps, which requires ***millimeter-scale resolution.*** The second approach was much more economical, as only part of the domain was finely refined. Nevertheless, the computational resources required for two-dimensional computations (both memory and computational time) were very high and required knowledge of the primary shock location, while three-dimensional computations would have been prohibitively expensive for production-type runs. Therefore, the approach employed here was a natural evolution of past deficiencies, i.e., employ a numerical scheme capable of dynamically adapting to traveling shocks and other flow discontinuities. This approach allows us to use coarse grid resolution everywhere in the computational domain where flow gradients are low, while applying very fine grid resolution wherever better flow resolution is required. Hence, shocks should always advance into finely refined zones, while grid coarsening should be obtained in areas already traversed by the shocks.

The objective of this study was to use the recently developed adaptive grid methodology on unstructured grids [11] to evaluate the effectiveness of candidate passive shock reflector devices. This device was placed at an opening in the wall of a semi-enclosed room. A radiator, or another heat-exchange device, was placed adjacent to the grill within the room. The shock reflector is supposed to allow free exchange of air during normal operations, while preventing blast waves from entering the enclosure when the structure is impacted by a shock. A simplified schematic of the structure and the shock reflector (often referred to as "grill") composed of simple, readily available, 90° chevrons is shown in Figure 2-1. Three layers of chevrons were employed in this specific design. A series of flat-plates was placed in front of the chevrons to block the flow from entering the spacing between the chevrons.

2.2 NUMERICAL RESULTS.

The transient, two-dimensional finite-element shock-capturing adaptive scheme on unstructured grids described in Section 1 (FEFLO27) was applied to the study of a shock interaction with a passive shock reflector placed at an opening of a vented enclosure (Figure 2-1). The computational parameters used in the simulation included:

- Number of time steps per refinement: seven
- Number of refinement levels: five
- Minimum normal size allowed: 25 μm
- Key variable for the error indicator: density
- Courant number: 0.4

The color contour results have 256 contours, where blue represents the lowest instantaneous local value and magenta the highest. The color designations for the mesh refinement levels are blue for the original mesh, and green, yellow, red, magenta and cyan for one, two, three, four and five refinement levels, respectively: one level of mesh refinement is defined as the division of a triangle into four, performed by connecting the mid-faces. Two parameters controlled mesh refinement: a) the maximum number of levels desired: five levels for this simulation; and b) the minimum normal height allowed: here, 25 μm, compared with the length of the computational domain (approximately five meters). A similarly resolved fixed-mesh methodology would require approximately $1.2*10^{10}$ nodes – an impossible task.

The initial conditions and the geometric details of this problem are shown in Figure 2-1, which shows both the initial pressure contours for the complete computational domain and for an expanded view near the middle of the grill. The incident weak shock, a step function with an amplitude of 10 psi overpressure (a value chosen for demonstration purposes only), was placed at t=0 to the left of the enclosed chamber. The shock propagated from left to right. The flow behind the shock was locally subsonic, while the shock Mach number was about 1.4. Figure 2-1 actually shows 2-D side-view schematics of the structure and the shock reflector (which will be referred to henceforth as the "grill"). Three layers of simple, readily available 90° chevrons were employed in this specific design. An array of bars (flat plates) was placed in front of the chevrons to block the flow from entering the spacing between the chevrons. This design was intended to: a) force the shock penetrating between the chevrons to diffract at large angles to optimize shock wave damping by the rarefaction waves originating at the corners; b) optimize shock deflection on direct impact at any angle; and c) produce vorticity behind the sharp corners that will reduce the effective flow area through the choking of the flow between the chevrons.

In the following analysis of the results, we will initially describe the large-scale, multiple shock-diffraction processes from initiation to the end of the simulation; we will then re-examine flow expansion around the top of the bar, and conclude with the discussion of the flow around the upstream corner of the first chevron. To enhance understanding of the physical processes and better exhibit the micro-scale physics, rather than show flow results for the complete computational domain, we will show expanded views of only one row of bar and chevrons combination located near the center of the grill; the lower quarter

of the grill shown in Figure 2-1b. Thus, both the top and the bottom boundaries of this domain are actually planes of symmetry. For convenience sake, they will be referred to in the following discussion as the top and bottom planes, while waves transmitted from the other side of the boundary will be referred to as reflected waves.

Figures 2-1 through 2-11 show combinations of computational mesh, grid refinement levels, pressure, vorticity and Mach number contours at several times. Figure 2-2 shows the mesh refinement levels, density and Mach number contours at t=0.125 ms. To better appreciate the dimensions of the physical processes simulated and the accuracy of the numerical scheme, it is noted that the thickness of the bar was 1 cm, or 10,000 μm. Excellent mesh adaptation to the incident and reflected shocks, as well as the large recirculation areas on top of the bar, are demonstrated. The Mach number of the flow accelerating around the corners is 0.95, increasing with time. At t=0.15 ms, the flow Mach number above the bar was already 1.05. The importance of this fact will be highlighted later in the discussion.

Rarefaction wave expansion from both corners is clearly shown in both Figures 2-2a-c (t=0.125 ms), and Figure 2-2d (t=0.18 ms), at which time the rarefaction wave originated at the upstream corner of the bar reflected from the bottom plane (or, since this is really a plane of symmetry, the arrival of the rarefaction wave from the opposite side of the bar). This process is vividly demonstrated by the transition of the planar reflection (Figure 2-2c) to a curved reflected shock (Figure 2-3b). The incident shock impinged on the first chevron at t=0.21 ms. Simultaneously, the curved, incident shock that has diffracted around the downstream corner of the bar, has reflected from the bottom plane. The upstream-propagated initial reflection from the bar has reflected from the top plane (actually, the reflected wave from the adjacent bar above). The Mach number results (Figure 2-3b) show that the flow above the bar has reached M=1.25. These results also show the merging of the two recirculating zones above the bar, incident shock reflection from the upstream front of the first chevron, the instantaneous initiation of rarefaction waves at both corners, and the simple shock reflection produced as the incident shock propagated toward the convex center of the first chevron (an obvious wave focusing point). Figure 2-3c (t=0.245 ms) shows the continued evolution of these processes: the incident shock has diffracted around the upstream corner of the first chevron; two rarefaction waves have emanated from the two upstream corners of the first chevron, the one from the bottom corner was fairly cylindrical, while the one from the top corner was contained within the reflected flattened shock. Incident shock wave diffraction over the 90° corners of the front bar, followed by its diffraction around the 135° corner of the first chevron, resulted in significant pressure amplitude reduction of the shock penetrating past the first chevron – only about 3.5 psi at this time.

The density and Mach number results at t=0.27 ms, shown in Figures 2-3d and e, respectively, show the continued growth of the merged vortices at the top of the front bar, where the single vortex was anchored at the upstream corner; the reflection of the shock that originally reflected from the first chevron, from the bottom plane; and the eminent interaction of the incident-shock reflection from the bottom plane with the two vortices (the one anchored at the top upstream corner of the bar and the one anchored at the upstream bottom corner of the first chevron).

Shock wave focusing at the convex center of the first chevron occurred at t=0.315 ms. The computational grid, mesh refinement levels, density and Mach number contours at t=0.35 ms, shown in Figures 2-4a-d, respectively, demonstrate the following: the excellent shock adaptation; the very small ratio of area well refined (i.e., occupied by the shocks) to the complete computational domain; the supersonic flow over the first layer of chevrons (M=1.24 at this time); the successful mesh coarsening after shock passage; and finally, the large amplitude of the reflected shock from the center of the first chevron (about 65 psi), much higher than would have been obtained for a regular shock reflection. The large amplitude reflected shock will be shown at later times (Figures 2-5 to 2-8) to create a high-pressure reflected jet that will persist for a very long time. Incidently, from a practical point of view, the large pressure will not damage this chevron as the pressure decays exponentially within 2-3 ms, and hence, the integrated impulse is below bending failure level. *Both the mesh refinement and density contours show systems of weak-amplitude* shocks (shocklets) emanating from the large separation zones near the corners. We will expand on the importance of this subject later in the discussion.

The downstream-propagated weakened incident shock expanded over the second layers of chevrons at t=0.45 ms (Figure 2-5a). While the incident shocks focused at the convex center of the second chevron at t=0.42 ms, forming another fairly-high amplitude reflected wave (about 18 psi at t=0.45 ms) that will help in blocking the incoming flow, the incident shock expanded over another pair of 90° corners, and was further weakened by another pair of cylindrical rarefaction waves expanded from both corners of the second chevron (especially the downstream corner). Generally, the diffraction processes around the second and third layers of chevrons were very similar to the diffraction around the first chevron, i.e., shock wave focusing toward the center of the chevron, instantaneous localized pressure increase, and a much larger amplitude (due to wave focusing) reflected shock. Nevertheless, the incident and reflected pressure amplitudes decreased drastically from layer to layer (about 65 psi for the first, 22 psi for the second and about 4.5 psi for the third). numbers

The incident wave impacted on the third layer of chevrons at about t=0.47 ms, and on its middle at t=0.52 ms. At t=0.50 ms (Figures 2-5b and c), the amplitude of the incident shock about to impact on the third chevron was only about 2.2 psi, resulting from the

multiple diffraction processes it had experienced. The shock that has diffracted around the third layer of chevrons was further weakened by another 135° diffraction process. In fact, energy dissipation of the incident shock by interaction with eight different rarefactions waves (i.e., propagating past eight corners), resulted in very strong attenuation of the incident 10 psi shock wave to a mere compression wave, with an amplitude of about 1.7 psi. The results at this time (Figure 2-5c) also show the system of shocks emanating from the complex separated vortex downstream of the front bar. This multiple-shock system resulted from the interaction between the mean supersonic flow between the bar and the first chevrons, and the convoluting vortex. This shock system evolves in time as the vortex breaks down.

The vortex roll-up process was enhanced by vortex interaction with the system of curved reflected shocks reverberating between the bar and the first chevron, and similarly, at other times, between the various chevrons. Since vortex dynamics is a phenomenon normally associated with viscous flow processes while the present numerical scheme only solves the Euler equations, the source of this vorticity must be addressed.

Vorticity production, as modeled in the Bjerknes Theorem [24], incorporates both viscous and inviscid contributions, and is expressed as:

$$\frac{D\vec{\xi}}{Dt} = -\nabla\left(\frac{1}{\rho}\right) \times \nabla P + \nu\nabla^2\vec{\xi}, \tag{2.1}$$

where $\vec{\xi}$ = Vorticity; ν = Kinematic Viscosity; P = Pressure; and ρ = Density. A time-scale and order-of-magnitude analysis of these terms indicates that the current vorticity production is controlled by the baroclinic effect (i.e., the first term in the equation that represents the non-alignment of pressure and density gradients), and thus can be predicted by the inviscid code. Past experience with shock-train interaction [25] demonstrated vortex sheet roll-up within a few microseconds after the shock diffracted around the corner, a time period too short for viscous processes to significantly affect the flow. It must be noted that we are fully aware of the contribution of numerical viscosity to the vortex production process. Nevertheless, based on past experience with similar computations and comparisons to experimental data, which were in excellent agreement [26], we believe this effect to be of secondary importance.

The computational mesh, mesh refinement levels, density and Mach number contours at t=0.6 ms, are shown in Figures 2-6a-d, respectively. These results, and the density results shown later at t=0.65 ms (Figure 2-7), demonstrate that the wave entering the enclosed chamber is a *weakened compression wave, not a steep- fronted shock wave.* The distinction is important not only because of the amplitude difference, but because the two waves would stagnate to vastly different pressure values. In addition, structural response

to the instantaneous loading of a shock is significantly more severe than the slower loading of a compression wave. Hence, if a heat exchange device would have been placed beyond the third layer of chevrons, the difference between a shock and a compression wave would have meant the difference between system survival and destruction. In addition, this figure shows, in great detail, the excellent adaptation of the multiple shock-wave system and the sharpness of the shocks. The refinement level tolerance for this calculation was set at a very low level. Therefore, even the weak compression waves entering the chamber are still captured (at least one level of refinement).

The computation was continued to t=5.0 ms, long after the system of shocks cleared the grill. Only four levels of refinement were used at this time, with a minimum normal of 0.2 mm (200 μm). The results at t=1.9 ms (Figure 2-8) demonstrate that: a) All shocks had propagated very long distances, but were still captured as sharp, nonoscillatory discontinuities; and b) The captured shocks' thickness did not change over several thousand steps, as all shocks were still captured over two to three elements, while the element size around the shock remained unchanged, due to the adaptive procedure. These results demonstrate, at least for the present application, the advantage of adaptive-mesh schemes over fixed-grid schemes. Achieving similar shock resolution with a fixed-mesh methodology would have required maintaining a fine grid virtually everywhere in the computational domain, at a significantly (perhaps prohibitively) higher computational cost. Grid refinement was observed as the shocks propagated into new areas, while grid coarsening was observed in areas already traversed by the shocks; a) The system of compression waves entering the enclosure had steepened, as should be expected from traveling, finite-amplitude compression waves; b) While the pressure outside the chevrons is about 12 psi (red levels at this figure), the pressure inside was less than 1.5 psi; c) Vortices are observed to shed from all sharp corners; and d) The vortices shed from the first and second layers of chevrons have just about blocked the entire area between the first and second chevrons. Mach number contours data demonstrate that the flow through the passage between the chevrons in the first layers had accelerated to supersonic speeds and formed a normal shock ahead of the center of the second layer chevron. From there, the flow has to turn 90°, literally squeezing between vortices shed from the first and second layers of chevrons, accelerate to supersonic speeds again, and then turn again by about 135° to pass through the next opening restricted by the vortex shed from the third layer. The choking of the flow at two locations restricts the mass, momentum and energy flux into the enclosure. Thus, the designed shock-reflector appears to limit the high-energy flow outside the enclosure from entering. The pressure inside and outside the enclosure has to equalize eventually. However, the objective was to design a passive reflector that will slow this process to a rate that can be tolerated by the sensitive equipment inside the enclosure. This objective has been achieved.

A final note relating to the computational performance of the code: computation time for approximately 12,000 time steps consumed approximately 8 hours of CPU time on a Cray YMP 8/128 computer (single processor). Computation time per node per time step was approximately 30 microseconds.

2.2.1 Shock Wave Diffraction Processes.

After examining the overall success of this device in mitigating shock amplitude and harmonic content entering the chamber, we will examine, in detail, shock diffraction around the first bar and the first chevron. As noted above, the greatest advantage of the adaptive grid methodology is that while it enables us to obtain an engineering level solution (i.e., a correct solution obtained within reasonable CPU and memory expenditures at a fast turn-around pace), it also allows the examination of the most minute physical detail, enabled by the minimum mesh size of 25 μm.

2.2.2 Shock Wave Diffraction Around the Front Bar.

Figure 2-9 shows expanded views of Mach number, density and vorticity contours around the top of the front bar between t=0.1375 ms to t=0.21 ms. To better appreciate the resolution displayed in these figures, it is noted that the bar thickness is 1 cm (10000 μm). A minimum normal size of 25 μm would allow placing about 400 points across the bar, a sufficient resolution.

At t=0.1375 ms, about 60 micro-seconds after shock impact, and only about 28 micro-seconds after shock diffraction around the downstream corner, two fully rolled-up vortices are shown to be shed from both corners. The vortex shed from the upstream corner develops a classic Kelvin-Helmholtz instability, with growing amplitude in the downstream direction. The multiple shocklets shown at this time (Figure 2-9a at t=0.1375) to emanate from the downstream-side of this vortex resulted from the interaction of the supersonic flow above the vortex with the unstable shear-layer - a flow resembling an unsteady supersonic flow over a curved wavy wall. It is postulated that the system of sound waves originated from the roll-up process of the shear layer (it is well known that a roll-up vortex acts as a quadrupole) is amplified by the supersonic flow. This assumption is supported by the fact that similar simulations with lower (subsonic) Mach numbers flows (and lower shock over-pressures) did not produce the system of oriented (normal to the flow) shocklets observed here. This process will be further investigated in the future.

The two shed vortices continue to grow, almost self-similarly, as shown by the density and vorticity results at t=0.15 ms (Figures 2-9b and 2-9g, respectively). Eventually, down-stream convection of the sound produced by the multiple-shocklet system resulted in an instability growth at the downstream vortex at t=0.18 ms, with an identical frequency, as

shown by both the density and Mach number results, Figures 2-9c and 2-9d, respectively.

The growing upstream, unstable vortex reached the downstream corner at t=0.21 ms. Figures 2-9e, 2-9f and 2-9h show the Mach number and vorticity contours, at t=0.21 ms and 0.245 ms, respectively. These results show the growing instability of the shear layer originating from the upstream corner, the merging and lifting of the two vortices by the entrained flow below the downstream vortex, the strong shock attached to the lifting upstream vortex, the two recirculation bubbles within this vortex, and the system of shocklets (or flow instability) still attached to the bottom vortex.

2.2.3 Shock Wave Diffraction Around the First Chevron.

The incident shock diffracted around the first chevron upstream corner at about t=0.25 ms. The density contours at t=0.30 ms, only 50 μs after shock passage (Figure 2-10a), show a fully developed, rolled-up vortex sheet attached to this corner. This figure also shows part of the leading incident shock, and its reflection from the bottom plane. The reflected shock has been broken by the chevron. Notice that the reflected shock under the chevron has propagated further than the shock on the left, as it has been accelerated by the vortex. In addition, the reflected shock from both faces of the chevron should have been continuous. Instead, on the underside of the chevron, the reflected shock has been broken by the different-direction velocities in the different segments of the vortex.

Figure 2-10b at t=0.35 ms, and Figures 2-10c and 2-10d, at t=0.40 ms, respectively, show the growth of the vortex and the downstream propagation of the Kelvin-Helmholtz instability originated near the corner. The system of unstable shocks that resulted from the interaction of the mean supersonic flow with the convoluted vortex attached to the upstream bar (Figure 2-5c at t=0.45 ms), has reached this corner, as shown in Figures 2-11a. In addition, the primary shock reflected from the center of the first chevron (Figures 2-4 and 2-5) has diffracted around the corner. The results show the break-up of this shock into two primary elements: the down-propagating part outside the vortex, and the part that has diffracted around the corner into the vortex. This part has been decelerated by the vortex since it was propagating against the flow near the wall. The shock between these cuts has been diffused, or sheared, by the local strong gradient (i.e., the subsonic to supersonic transition) across the vortex sheet (Figure 2-11a_2). In addition, another shock, which has previously reflected from the bottom plane, is shown at this time to pass through the vortex, and is located exactly at the corner. When traced through the vortex, it is shown that the shock has been stretched or compressed depending on the propagation direction relative to the local flow; the shock immediately outside the vortex has been accelerated downstream; inside the vortex the shock was either accelerated or decelerated, depending on the local mean flow direction.

Figures 2-11a through 2-11g show a series of density, Mach number and vorticity contours at times of 0.45, 0.48, 0.49, 0.50, 0.51, 0.55 and 0.60 ms, respectively. This series clearly shows: a) continuous growth of the unstable vortex; b) multiple shock-vortex interactions that resulted in partial break-up of the vortex; and c) shock acceleration-deceleration by the local flow within and outside the vortex. Notice, for instance, the pair of shocks that appeared on the right side at t=0.49 ms. These shocks reflected from the second chevron (Figure 2-5b). The curvature of these shock changed in time since different parts of the shock were convected at different local velocities; the shock portion near the bottom plane was convected against mean flow Mach number significantly lower than at the circumference of the vortex (Figure 2-6d). Another example is shown in Figure 2-11c through g as the shock that has reflected from the bottom plane and propagated upward near the edge of the chevron was partially transmitted and partially reflected by the vortex. The portion outside had propagated upward slower than the shock portion inside the vortex (Figure 2-11f_1), simply because the mean flow outside was transonic and in the opposite direction, while the flow inside the vortex was almost stagnant. Still another example is the second reflected shock from the second chevron, moving in the observed frames from right to left. Comparison of the results at t=0.55 and t=0.60 ms (Figures 2-11f and g, respectively) shows the stretching and compression of this shock as it passes through the vortex. While at t=0.55 ms this shock was almost continuous (at the right side of the figure), at t=0.60 ms the broken shock is clearly traceable through the vortex, up to the reflection from the bottom face of the first chevron; d) shock-induced vortex instability. Shock interaction with the unstable vortex is shown to induce further instability, and some directionality in the vortex break-up process. Notice, for instance, vortex break-up due to the interaction with the upstream moving shock shown in Figures 2-11f_1 through 2-11f_3, and 2-11g_1 through 2-11g_3, with the strongest effect immediately after shock passage (compare, for instance, Figures 2-11f_2 and 2-11g_2).

2.3 SUMMARY AND CONCLUSIONS.

A recently developed transient, two-dimensional, finite-element, shock-capturing scheme on unstructured grids was applied to the study of a shock interaction with a passive shock-reflector placed at an opening of a vented enclosure. The objective of this effort was to design a passive device which, while allowing the normal ventilation of the enclosure under steady conditions, will prevent blast-waves impinging on the wall from entering the enclosure. Shock wave attenuation resulted here from the shock diffraction processes around the chevrons, that damped the incident shock wave amplitude and harmonic content, and eventually transformed the shock to a low- amplitude compression wave by the time it entered the enclosure. In addition, the sharp corners of the grill were relied on to produce vortices which significantly reduced the effective flow area (a self- choking device) to slow

the outside quasi-steady high-pressure flow behind the shock from entering the chamber.

From the numerical point of view, the results demonstrate the capability of the developed adaptive refinement/coarsening algorithm to properly adapt to weak shocks, rarefaction waves and contact discontinuities and the resultant excellent resolution of the captured flow features. All shocks had propagated very long distances, but were still captured as sharp, nonoscillatory discontinuities. Grid refinement was observed as the shocks propagated into new areas, while grid coarsening was observed in areas already traversed by the shocks. In addition, the captured shocks' thickness did not change over several thousand steps, as all shocks were still captured over two to three elements, while the element size around the shock has been unchanged, thanks to the adaptive procedure.

Among the many interesting physical processes monitored in this computation were the growth of unstable shear layers, transient shock interaction with unstable shear layers, shock-shock interaction, shock-rarefaction interaction, etc. Vortices are observed to shed from all sharp corners. The vortex roll-up process was enhanced by vortex interaction with the system of curved reflected shocks reverberating in the system. Since vortex dynamics is a phenomenon normally associated with viscous flow processes while the present numerical scheme only solves the Euler equations, we have investigated this phenomenon and concluded that vorticity production immediately after shock passage resulted from the "Bjerknes Effect." The shed vortices resulted in effective flow-area restrictions. Specifically, the vortices shed from the first and second layers of chevrons almost completely blocked the flow between the first and second chevrons, choking the flow and restricting the mass, momentum and energy flux into the enclosure. Thus, the designed shock-reflector appears to limit the high-energy flow outside the enclosure from entering. The pressure inside and outside the enclosure has to equalize eventually. However, the objective was to design a passive reflector that will slow down this process to a rate that can be tolerated by the sensitive equipment inside the enclosure. This objective has been achieved.

2.4 REFERENCES.

[1] P. Woodward and P. Colella - The Numerical Simulation of Two-Dimensional Fluid Flow with Strong Shocks; *J. Comp. Phys.* 54, 115-173 (1984).

[2] H.M. Glaz, P. Colella, I.I. Glass and R.L. Deschambault - A Numerical Study of Oblique Shock-Wave Reflections with Experimental Comparisons; *Proc. Roy. Soc. Lond.* A 398, 117-140 (1985).

[3] M. Fry, J. Tittsworth, A. Kuhl, D.L. Book, J.P. Boris and M. Picone - Transport Algorithms with Adaptive Gridding; *Proc. 13th Int. Symp. on Shock Tubes and Waves* (C.E. Treanor and J.G. Hall eds.), 376-384 (1982).

[4] S.T. Zalesak - Fully Multidimensional Flux-Corrected Transport Algorithm for Fluids; *J. Comp. Phys.* 31, 335-362 (1979).

[5] J.P. Boris and D.L. Book - Flux-corrected Transport. I. SHASTA, a Transport Algorithm that works; *J. Comp. Phys.* 11, 38 (1973).

[6] J.P. Boris and D.L. Book - Flux-corrected Transport. III. Minimal-Error FCT Algorithms; *J. Comp. Phys.* 20, 397-431 (1976).

[7] P.L. Roe - Approximate Riemann Solvers, Parameter Vectors and Difference Schemes; *J. Comp. Phys.* 43, 357-372 (1981).

[8] A. Harten - High Resolution Schemes for Hyperbolic Conservation Laws; *J. Comp. Phys.* 49, 357-393 (1983).

[9] P.K. Sweby - High Resolution Schemes Using Flux Limiters for Hyperbolic Conservation Laws; *SIAM J. Num. Anal.* 21, 995-1011 (1984).

[10] A.K. Parrott and M.A. Christie - FCT Applied to the 2-D Finite Element Solution of Tracer Transport by Single Phase Flow in a Porous Medium; *Proceedings of the ICFD-Conf. on Numerical Methods in Fluid Dynamics*, Reading, Academic Press, 1986.

[11] R. Löhner, K. Morgan, M. Vahdati, J.P. Boris and D.L. Book - FEM-FCT: Combining Unstructured Grids with High Resolution; *Comm. Appl. Num. Meth.* 4, 717-730 (1988).

[12] R. Löhner, K. Morgan, J. Peraire and M. Vahdati - Finite Element Flux-Corrected Transport (FEM-FCT) for the Euler and Navier-Stokes Equations; *Int. J. Num. Meth. Fluids* 7, 1093-1109 (1987).

[13] I. Babuska et.al. (eds.) - *Accuracy Estimates and Adaptive Refinements in Finite Element Computations*; J. Wiley and Sons (1986).

[14] B. Palmerio and A. Dervieux - Application of a FEM Moving Node Adaptive Method to Accurate Shock Capturing; *Proc. First Int. Conf. on Numerical Grid Generation in CFD*, Landshut, W. Germany (1986).

[15] W. Schönauer, K. Raith and K. Glotz - The Principle of Difference Quotients as a Key to the Self-Adaptive Solution of Nonlinear Partial Differential Equations; *Comp. Meth. Appl. Mech. Eng.* 28, 327-359 (1981).

[16] J.F. Dannenhoffer and J.R. Baron - Robust Grid Adaptation for Complex Transonic Flows; AIAA-86-0495 (1986).

[17] R. Löhner, K. Morgan and O.C. Zienkiewicz - An Adaptive Finite Element Procedure for High Speed Flows; *Comp. Meth. Appl. Mech. Eng.* 51, 441-465 (1985).

[18] R. Löhner and K. Morgan - Improved Adaptive Refinement Strategies for Finite Element Aerodynamic Computations; AIAA-86-499 (1986).

[19] J. Peraire, M. Vahdati, K. Morgan and O.C. Zienkiewicz - Adaptive Remeshing for Compressible Flow Computations; *J. Comp. Phys.* 72, 449-466 (1987).

[20] M.J. Berger and J. Oliger - Adaptive Mesh Refinement for Hyperbolic Partial Differential Equations; *J. Comp. Phys.* 53,484-512 (1984).

[21] M.D. Smooke and M.L. Koszykowsky - Two-Dimensional Fully Adaptive Solutions of Solid-Solid Alloying Reactions; *J. Comp. Phys.* 62, 1-25 (1986).

[22] J.T. Oden, P. Devloo and T. Strouboulis - Adaptive Finite Element Methods for the Analysis of Inviscid Compressible Flow: I. Fast Refinement/Unrefinement and Moving Mesh Methods for Unstructured Meshes; *Comp. Math. Appl. Mech. Eng.* 59, 327-362 (1986).

[23] R. Löhner - An Adaptive Finite Element Scheme for Transient Problems in CFD; *Comp. Meth. Appl. Mech. Eng.* 61, 323-338 (1987).

[24] V. Bjerknes, J. Bjerknes, T. Bergeron and H. Solberg - *Physikalische Hydrodynamik*, Springer Verlag, Berlin, 1933.

[25] J.D. Baum, R. Löhner - Numerical Simulation of Shock-Elevated Train Interaction Using an Adaptive Finite Element Shock Capturing Scheme; AIAA-89-0653 (1989).

[26] S. Sivier, J.D. Baum, E. Loth and R. Löhner - Simulations of Shock Wave Generated Vorticity; AIAA-91-1668 (1991).

SECTION 3
NUMERICAL SIMULATION OF SHOCK INTERACTION WITH COMPLEX-GEOMETRY 3-D ABOVE-GROUND STRUCTURES

This section describes the application of a recently developed three-dimensional adaptive finite element shock capturing scheme on unstructured tetrahedral grids to the simulation of shock diffraction processes around typical complex geometry three-dimensional structures such as tanks and missiles. The 3-D surfaces were defined using a new CAD-CAM-like user-friendly solid-body generator (PREGEN3D). The advancing front method then generated the volume grid. The shock diffraction simulations were initiated by imposing the initial and boundary conditions; only two levels of refinement were used to refine the shock at its initial position. The resolution and fidelity of the simulated shock wave diffraction phenomena, performed via a solution of the transient compressible Euler equations, were enhanced by the application of the classic h-enrichment/coarsening grid adaptation scheme, with density as the critical adaptation parameter. A high degree of vectorization was achieved by pre-sorting the elements and then performing the refinement/coarsening on the assembled groups. Further reductions in CPU-requirements were realized by optimizing the identification and sorting of elements for refinement and deletion.

The computational results obtained demonstrate the successful application of the new 3-D adaptation procedure to shock interaction with curved surfaces - a new capability. Excellent shock adaptation and resolution are obtained at all times; all shocks are captured as sharp discontinuities, without producing pre- or post-shock oscillations. Several interesting three-dimensional shock diffraction processes are identified and discussed in detail. It is shown that the geometry must be described precisely in order to obtain the correct lift and drag forces on the vehicle. Finally, the results demonstrate the robust performance of the method and show, at least for the simulation of strongly unsteady flows, considerable savings in both CPU-time and storage over fixed-mesh structured grid schemes.

3.1 INTRODUCTION.

The solution of large-scale transient problems around complex geometries is a common problem to many areas of computational fluid dynamics. Before developing a numerical methodology to simulate these flows, one must choose between structured or unstructured grid schemes. Both have their advantages and disadvantages. The biggest disadvantages of the structured grid approach are: a) the gridding of a reasonably complex, engineering type 3-D structure may require many man-months, compared to days/weeks with the

unstructured grid approach; and b) the complexity involved in developing adaptation algorithms on structured grids for strongly transient features. The advantages of the structured grid methodology over unstructured grids are: a) significantly reduced memory overhead requirements (about 5-15 times lower); and b) reduced computation time per node per time step (about 3 times faster). Thus, for a typical 3-D computation, the unstructured, adaptive approach may be superior only for flow simulation around a complex geometry structure and/or shock-wave propagation over large temporal and spatial domains.

Past attempts to simulate transient shock interaction with complex geometry 3-D bodies have been limited. Some experience was gained applying a structured, non-adaptive grid approach to simulate shock interaction with 3-D semi-submerged structures. One approach prescribed the sloped surfaces of the body as "staircases" [1,2], which would naturally yield a somewhat erroneous solution. Another disadvantage of this approach is that numerical boundary layers are developed whenever shocks climbing along the staircases represent curved boundaries.

The objective of the present research was to numerically simulate shock diffraction processes about complex-geometry 3-D structures. Under a separate project, we recently developed a numerical methodology capable of efficiently simulating transient shock-shock and shock-structure interactions for realistic, complex, engineering-type three-dimensional geometries. The unstructured grid approach [3] was the most suitable for generating surface and volume grids for complex-geometry bodies. In addition, since our typical areas of interest require the simulation of strong shocks, both steady and transient, a high-resolution monotonicity-preserving algorithm for unstructured grids was developed. The method, called FEM-FCT [4], is based on Zalesak's [5] generalization of the Flux-Corrected Transport (FCT) algorithms [6,7] to multidimensional problems. Extensive application of FEM-FCT to 2-D simulations [8,9], as well as limited experience with 3-D (shock wave propagation over simplified geometries [10]), has demonstrated excellent agreement with experimental data. With these schemes, both traveling as well as stationary shocks are captured within two-three gridpoints (for either 2-D or 3-D) without the over- and undershoots that appear in linear schemes. Finally, since the flowfields typically are smooth except for a few regions where strong gradients appear, efficient adaptive refinement techniques for transient problems are required.

As noted above, a major advantage of the unstructured over the structured grid approach is the ease with which each complex geometry structure can be discretized [11]. Generating the surface or volume grids for a typical airplane or vehicle may take several man-months using a structured grid approach, and only one to two weeks using an unstructured grid [11,12]. A second very attractive feature of unstructured grids is the ease with which adaptive refinement can be incorporated. Since additional degrees of freedom do

not destroy any previous structure, the flow solver requires no further modification when operating on an adapted grid. For many practical problems, the regions that need to be refined are extremely small as compared to the overall domain. Therefore, the savings in storage and CPU-requirements typically range between 50-100 as compared to an overall fine mesh [8,13,14]. Our experience in 2-D [8,9] indicates that for the majority of the daily production-type runs, adaptive refinement makes the difference in the ability or inability to run the problems to an acceptable accuracy in a reasonable time. Without it, we would be forced to use much coarser grids, with lower accuracy, for the same expense. Here we extend the 2-D capabilities to 3-D. Although more complex in coding, the rewards of a 3-D adaptive refinement capability are greater than those encountered in 2-D.

The meshes used for the present calculations were generated using FRGEN3D [12,17]. This unstructured grid generator is based on the advancing front method. After defining the surface description of the domain to be gridded, these surfaces are triangulated. Thereafter, the face forming the smallest new element is deleted from the front, and a new element is added. This process is repeated recursively until no more faces are left in the front. FRGEN3D generates approximately 25,000 tetrahedra per minute on the Cray-2. This number may increase for small meshes (less than 50,000 tetrahedra), as more front collapses per element generated. For very large meshes, a global h-refinement option is available. With it, the rate of generation is increased to about 200,000 tetrahedra per minute.

Over the past three years it became clear that FRGEN3D by itself was not sufficient to quickly generate the mesh required for an arbitrary 3-D problem. Although it solves the generation problem once and for all, the surface generation then becomes the dominant man-hour bottleneck. Therefore, under a separate research project we recently developed FECAD, a suite of tools that allows the user to produce FRGEN3D-compatible, error-free input in a faster way. FECAD not only allows the user to exercise basic CAD-CAM operations (shrinking, translations, rotations, surface lofting, etc.), but also eases the merging of several parts of the surface into one cohesive, well-defined input-file. This allows the merger of files produced by different users and/or different surface generators. FECAD has a whole series of built-in diagnostics to avoid such undesirable features as doubly defined points, isolated points or lines, and badly defined lines or surfaces. FECAD proved invaluable when trying to construct in a matter of days an error-free FRGEN3D-compatible input-file.

Another important capability that was developed over the past four years was PREBACK, a semi-structured 3-D background generator. Experience with the user community has shown that the preferred way of generating background grids is by lofting a 2-D triangulation in the third dimension or by rotation. PREBACK allows both operations. In

addition, it allows interactive operations to move background grid-points around (translation, rotation, shrinking, etc.), as well as to modify the grid-generation parameters in space (size, shape).

The flow solver employed was FEFLO74, a 3-D ALE hydro-solver based on FEM-FCT [10,15,16]. H-refinement [13,16] is the preferred approach for grid adaption. The high order scheme used is the consistent-mass Taylor-Galerkin algorithm. Combined with a modified second order Lapidus artificial viscosity scheme, the resulting scheme is second order accurate in space and fourth order accurate in phase. The spatio-temporal adaptation is based on local h-refinement, where the refinement/deletion criterion is a modified H2-seminorm [13]. Based on past experience with simulations of shock wave propagation processes in both 2-D and 3-D, density was chosen as the critical parameter for the refinement/deletion criterion.

Post-processing was performed with the FEPOST3D and MOVIESUBS packages. FEPOST3D is based on FEPLOT4D [18], but performs all the CPU-intensive filtering operations on the Cray. Only the plane- or surface-triangulations are sent back to the SGI-IRIS-4D/80GT for plotting. The user specifies before the run the planes and surfaces to be inspected. Although seemingly trivial, this step was in a large part responsible for the success of the present effort. It implied waiting 30 seconds for a plot-file (about 2.5-4Mbytes of information), instead of hours (about 130-160Mbytes for a complete flowfield mesh). In addition, it allowed the production of movies.

In the following sections we will briefly review some of the main schemes that are integrated into FEFLO74, such as the efficient error indicator and the FCT-FEM algorithm. More detailed analysis is found in Ref [19]. In addition, we include a description of some of the recent algorithm modifications and improvements that reduced CPU requirements and improved the performance of the methodology.

3.2 THE ERROR INDICATOR.

Many variants of an efficient error indicator had been investigated in the past [3-10]. Here, we seek a method that is efficient and reliable for *transient* compressible flow problems. This leads us to the following design criteria for the error indicator:

a) The error indicator should be fast.

b) The error indicator should be dimensionless, so that several key variables can be monitored simultaneously.

c) The error indicator should be bounded, so that no further user intervention becomes necessary as the solution evolves.

d) The error indicator should not only mark the regions with strong shocks to be refined, but also weak shocks, contact discontinuities and other weak features in the flow.

For the refinement method, the design criteria are as follows:

a) The method should be conservative, i.e., a mesh change should not result in the production or loss of mass, momentum or energy.

b) The method should not produce elements that are too small, as this would reduce too severely the allowable timestep of the explicit flow solvers employed.

c) The method should be fast. In particular, it should lend itself to some degree of parallelism.

d) The method should not involve a major storage overhead.

3.2.1 The Error Indicator.

An error indicator that meets the design criteria (a-d) was proposed in [3] as follows:

$$\text{error} = \frac{h^2 \; |\textit{second derivatives}|}{h \; |\textit{first derivatives}| + \epsilon \; |\textit{mean value}|} \; . \tag{3.1}$$

By dividing the second derivatives by the absolute value of the first derivatives, the error indicator becomes bounded, dimensionless, and the "eating up" effect of strong shocks is avoided. The terms following ϵ are added as a noise filter in order not to refine "wiggles" or "ripples" which may appear due to loss of monotonicity. The value for ϵ thus depends on the algorithm chosen to solve the PDEs describing the physical process at hand. The multidimensional form of this error indicator is given by

$$E^I = \sqrt{\frac{\sum_{k,l} (\int_\Omega N^I_{,k} N^J_{,l} d\Omega \cdot U_J)^2}{\sum_{k,l} (\int_\Omega |N^I_{,k}| \left[|N^J_{,l} U_J| + \epsilon \left(|N^J_{,l}| |U_J| \right) \right] d\Omega)^2}}, \tag{3.2}$$

where N^I denotes the shape-function of node I. This error indicator has performed very well in 2-D over the years [3,4]. However, when first used in 3-D, it proved unreliable. The source for this seemingly inconsistent behavior was found to originate from the large *local* variations in element size, shape, as well as the number of elements surrounding a point. These will produce large variations of the second term in the denominator that are not based on physics, but on the mesh structure itself. The solution was to modify the error indicator as follows:

$$E^I = \sqrt{\frac{\sum_{k,l}(\int_\Omega N^I_{,k} N^J_{,l} d\Omega \cdot U_J)^2}{\sum_{k,l}(\int_\Omega |N^I_{,k}||N^J_{,l} U_J| d\Omega)^2 + \epsilon MMAT_I h_I^{-2} |U_I|}}, \tag{3.3}$$

where $MMAT_I$ is the lumped mass-matrix at point I, and h_I the average element length at point I. This error indicator proved to be remarkably insensitive to local variations in element size and shape, while still yielding the correct indicator values for physical phenomena of interest. We attribute this robust performance to the smoothing effects of two averaging operations working simultaneously: the lumped mass-matrix and the point-lengths.

After determining the values of the error indicators in the elements, all elements lying above a preset threshold value $CTORE$ are refined, while all elements lying below a pr threshold value $CTODE$ are coarsened. Protective layers of elements are added to su nd the elements to be refined, so that the "feature" (e.g., a shock) always travels into an already refined region. The number of protective layers that are added depends on the Courant-number employed and the number of time steps taken between grid modifications. Usually the refinement is performed every 5-10 time steps, so that a Courant-number of C_n=0.2 is sufficient.

3.2.2 Adaptive Refinement Method.

Our previous experience in 2-D indicates that the only two refinement methods that are truly general and efficient for the class of problems considered here are h-refinement [3,5] and remeshing [7,8,10]. However, for ***strongly unsteady problems***, where a new grid is required every 5-10 time steps, local h-refinement seems to be preferable. Several reasons can be given for this choice:

a) Conservation presents no problem for h-refinement.

b) No interpolations other than the ones naturally given by the element shape-functions are required. Therefore, no numerical diffusion is introduced by the adaptive refinement procedure. This is in contrast to adaptive remeshing, where the grids before and after a mesh change may not have the same points in common. The required interpolations of the unknowns will result in an increased amount of numerical diffusion [9].

c) H-refinement is very well suited to vector- and parallel processors. This is of particular importance in the present context, where a mesh change is performed every seven time steps, and a large percentage of mesh points is affected in each mesh change.

d) H-refinement is more robust than remeshing.

As described above, we limit the number of refinement/coarsening levels per mesh change to one. Moreover, we only allow refinement of a tetrahedron into two (along a side), four (along a face) or eight new tetrahedra. We call these tetrahedra 1:2, 1:4 and 1:8 tetrahedra or refinement cases respectively. At the same time, a 1:2 or 1:4 tetrahedron can only be refined further to a 1:4 tetrahedron, or by first going back to a 1:8 tetrahedron with subsequent further refinement of the 8 sub-elements. We call these the 2:4, 2:8+ and 4:8+ refinement cases. The refinement cases are summarized in Figure 3-1. This restrictive set of refinement rules is necessary to avoid the appearance of ill-deformed elements. At the same time, it considerably simplifies the refinement/coarsening logic. An interesting phenomenon that does not appear in 2-D is the apparently free choice of the inner diagonal for the 1:8 refinement case. As shown in Figure 3-2, we can place the inner four elements around the inner diagonals 5-10, 6-8, or 7-9. In the present case, the shortest inner diagonal was chosen. This choice produces the smallest amount of distorted tetrahedra in the refined grid. When coarsening, we again only allow a limited number of cases that are compatible with the refinement. Thus, the coarsening cases become 8:4, 8:2, 8:1, 4:2, 4:1, 2:1. These coarsening cases are summarized in Figure 3-3.

When constructing the algorithm to refine or coarsen the grid, one faces the usual decision of speed versus storage. The more information from the previous grid that is stored, the faster the new grid may be constructed. As storage requirement minimization was one of the goals of the present research, we tried to keep only the essential information needed between mesh changes while minimizing CPU time. This was accomplished by using a modified tree-structure which requires twelve integer locations per element in order to identify the parent and son elements of any element, as well as the element type.

The first seven integers store the new elements (sons) of an element that has been subdivided into eight (1:8). For the 1:4 and 1:2 cases, the sons are also stored in this allocated space, and the remaining integer locations are set to zero. In the eighth integer the element from which the present element originated (the parent element) is stored. The ninth integer denotes the position number in the parent element from which this element came. The tenth integer denotes the element type. We can either have parents or sons of 1:8, 1:4 or 1:2 tetrahedra. We mark these with a positive value of the element type for the parents, and a negative value for the sons. Thus, for example, the son of a 1:8 element would be marked as -8. Finally, in the eleventh and twelfth integer locations the local and global refinement levels are remembered. These twelve integer locations per element are sufficient to construct further refinements or to reconstruct the original grid.

3.2.3 Algorithmic Implementation.

Having outlined the basic refinement/coarsening strategy, we can now describe in more

depth its algorithmic implementation. One complete grid change algorithmically requires the following five steps:

1) Construction of the missing grid information needed for a mesh change.

2) Identification of the elements to be refined.

3) Identification of the elements to be deleted.

4) Refinement of the grid where needed.

5) Coarsening of the grid where needed.

1. Construction of Missing Grid Information. The missing information consists of the sides of the mesh and the sides belonging to each element. The sides are dynamically stored in two arrays, one containing the two points each side connects and the other one (a pointer-array) containing the lowest side-number reaching out of a point. The formation of these two arrays is accomplished in three main loops over the elements, which are partially vectorizable. After having formed these two side-arrays, a further loop over the elements is performed, identifying which sides belong to each element.

2. Identification of Elements to be Refined. The aim of this sub-step is to determine on which *sides* further gridpoints need to be introduced, so that the resulting refinement patterns on an element-level belong to the allowed cases listed above, thus producing a compatible, valid new mesh. Five main steps are necessary to achieve this goal:

a) Mark elements that require refinement;

b) Add protective layers of elements to be refined;

c) Avoid elements that become too small, or that have been refined too often.

d) Obtain preliminary list of sides where new points will be introduced;

e) Add further sides to this list until an admissible refinement pattern is achieved.

a) Mark elements that require refinement

Using the modified error indicator given by Eq. (1.3) and the prescribed refinement tolerance ***CTORE***, those elements that require further refinement are marked using the array ***LELEM(1:NELEM)***. This array is marked as ***LELEM(IE)=1*** $\Rightarrow$ element is to be refined, ***LELEM(IE)=0*** $\Rightarrow$ element is not to be refined.

b) Add protective layers of elements to be refined

If protective layers of elements are to be added ahead of the feature to be refined, we perform, for each additional layer, the following set of operations:

- Zero an integer point-array (e.g., *LPOIN(1;NPOIN)=0*);
- Loop over the elements to be refined, marking (e.g., *LPOIN(IP)=1*) all points connected to these elements;
- Zero the integer element-array (e.g., *LELEM(1;NELEM)=0*);
- Loop over all elements; if at least one point of a given element has been marked, refine this element (e.g., *LELEM(IE)=1*)

c) Avoid elements that become too small, or that have been refined too often

A sharp feature in the flow domain, like a shock, will tend to produce error indicator values that always lie above the refinement tolerance *CTORE*. As a consequence, elements close to such a feature will be refined every time the mesh is adapted. In order to avoid this "refinement ad infinitum," one has to impose either a maximum permissible number of refinement levels per element, or/and a minimum allowable element size. Given these constraints, those elements which are already too small (if a minimum allowed element size has been given), or have already been refined too many times (if a maximum allowed number of refinement levels has been prescribed), are deleted from the list of elements to be refined.

d) Obtain preliminary list of sides for new points

Given the side/element information obtained above, we can now determine a first set of sides on which new gridpoints need to be introduced. This set of sides is still preliminary, as we only allow certain types of refinement.

e) Add further sides to this list until an admissible refinement pattern is achieved

The list of sides marked for the introduction of new points is still preliminary at this point. In most cases, it will not lead to an admissible refinement pattern to construct a new mesh. Therefore, further sides are marked for the introduction of new points until an admissible refinement pattern is reached. This is accomplished by looping several times over the elements, checking on an element level whether the set of sides marked can lead to an admissible new set of sub-elements. The algorithm used is based on the observation that the admissible cases are based on the introduction of new points along one side (1:2), three contiguous sides (1:4), or six contiguous sides (1:8). These admissible cases can be obtained from the following element-by-element algorithm:

- Set the node-array LNODE(1:4)=0;
- Loop over the sides of the element: if the side has been marked for the introduction of a new point, set LNODE(IP1)=1, LNODE(IP2)=1, where IP1, IP2 are the end-nodes corresponding to this side;
- Loop over the sides of the element: if LNODE(IP1)=1 and LNODE(IP2)=1, mark

the side marked for the introduction of a new point.

Practical calculations with several admissible layers of refinement and large grids revealed that sometimes up to 15 passes over the mesh were required to obtain an admissible set of sides. A considerable reduction in CPU was achieved by presorting the elements as follows:

- Add up all the sides marked for refinement in an element;
- If 0,1 or 6 sides were marked: do not consider further;
- If 4 or 5 sides were marked: mark all sides of this element to be refined;
- If 2 or 3 sides were marked: analyze in depth.

This then yields the final set of sides on which new gridpoints are introduced.

3. Identification of Elements to be Deleted. The aim of this sub-step is to determine which *points* are to be deleted, so that the resulting coarsening patterns on an element-level belong to the allowed cases listed above, thus producing a compatible, valid new mesh. Four main steps are necessary to achieve this goal:

a) Mark elements to be deleted;

b) Filter out elements where the parent and all sons are to be deleted;

c) Obtain preliminary list of points to be deleted;

d) Delete points from this list until an admissible coarsening pattern is achieved.

a) Mark elements to be deleted

As before, we start by determining from the modified error indicator given by Eq. (1.3) and the prescribed deletion tolerance $CTODE$, those elements that should be coarsened. Thus, we mark an element array $LELEM(1:NELEM)$ as follows: $LELEM(IE)=-1 \Rightarrow$ element is to be deleted, $LELEM(IE)=0 \Rightarrow$ element is not to be deleted.

b) Filter out elements where parent and all sons are to be deleted

It is clear that only those elements should be deleted, for which both the parent as well as all its sons have been marked for deletion. Therefore, only the parent elements to be coarsened are considered further. For these elements, a check is performed whether their respective son elements have also been marked for deletion. If any of the son elements have not been marked for deletion, neither the parent-element nor any of its sons are considered further.

c) Obtain preliminary list of points to be deleted

Given the list of parent-elements to be coarsened, we can now determine a preliminary list of points to be deleted. Thus, all the points that would be deleted if all the elements contained in this list were coarsened are marked as "total deletion points".

d) Delete points from this list until an admissible coarsening pattern is achieved

The list of total deletion points obtained in the previous step is only preliminary, as unallowed coarsening cases may appear on an element level. We therefore perform loops over the elements, deleting all those total deletion points that would result in allowed coarsening cases for the elements adjoining them. This process is stopped when no incompatible total deletion points are left.

4. Refinement of the Grid Where Needed. The introduction of further points and elements is performed in two independent steps, which in principle could be performed in parallel.

1) Points: To add further points, the sides marked for refinement in sub-step 2 are grouped together. For each of these sides a new grid-point will be introduced. The interpolation of the coordinates and unknowns is then performed using the side/point information obtained in sub-step 1. These new coordinates and unknowns are added to their respective arrays. In the same way new boundary conditions are introduced where required.

2) Elements: In order to add further elements, the sides marked for refinement are labelled with their new gridpoint-number. Thereafter, the element/side information obtained in sub-step 1 above is employed to add the new elements. The elements to be refined are grouped together according to the refinement cases shown in Figure 3-1. Each case is treated in block fashion in a separate subroutine. Perhaps the major breakthrough of the present work was the reduction of the many possible refinement cases to only six. In order to accomplish this, some information for the 2:8+ and the 4:8+ cases is stored ahead in scratch arrays. After these elements have been refined according to the 2:8 and 4:8 cases, their sons are screened for further refinement using this information. All sons that require further refinement are then grouped together as 1:2 or 1:4 cases, and processed in turn.

5. Coarsening of the Grid Where Needed. The deletion of points and elements is again performed in two independent steps, which in principle could be performed in parallel.

a) Points: The points to be deleted having been marked in sub-step 3 above, all that remains to be done is to fill up the voids in the coordinate-, unknown- and boundary condition-arrays by renumbering points and boundary conditions.

b) Elements: The deletion of elements is again performed blockwise, by grouping together all elements corresponding to the coarsening cases shown in Figure 3-3. Thereafter, the elements are also renumbered (in order to fill up the gaps left by the deleted elements), and the point-renumbering is taken into consideration within the connectivity-arrays.

3.2.4 Recent Algorithm Modifications.

We have recently significantly modified the adaptive finite element methodology for transient problems in 3-D [6]. Since for typical shock calculations, mesh adaption takes

place every 5-10 time steps, we concluded that every stage of the adaption process must be thoroughly optimized. The two areas that required the most intense optimization efforts were:

a) Error indicators for grids with large local variations of element size and shape, and

b) Faster construction of the new mesh.

Improved error indicators: As an error indicator we use a modified interpolation theory error indicator:

$$E^I = \sqrt{\frac{\sum_{k,l}(\int_\Omega N^I_{,k} N^J_{,l} d\Omega \cdot U_J)^2}{\sum_{k,l}(\int_\Omega |N^I_{,k}| \left[|N^J_{,l} U_J| + \epsilon \left(|N^J_{,l}||U_J|\right)\right] d\Omega)^2}}, \tag{3.4}$$

where N^I denotes the shape-function of node I. By dividing the second derivatives by the absolute value of the first derivatives the error indicator becomes bounded, dimensionless, and the 'eating up' effect of strong shocks is avoided. This error indicator has performed very well in 2-D over the years [2]. However, when first used in 3-D, it proved unreliable. The source for this seemingly inconsistent behavior was found to stem from the large *local* variations in element size, shape, as well as the number of elements surrounding a point encountered in typical 3-D unstructured grids. These will produce large variations of the second term in the denominator, which are not based on physics but on the mesh structure itself. The solution was to modify this error indicator as follows:

$$E^I = \sqrt{\frac{\sum_{k,l}(\int_\Omega N^I_{,k} N^J_{,l} d\Omega \cdot U_J)^2}{\sum_{k,l}(\int_\Omega |N^I_{,k}||N^J_{,l} U_J| d\Omega)^2 + \epsilon MMAT_I h_I^{-2} |U_I|}}, \tag{3.5}$$

where $MMAT_I$ is the lumped mass-matrix at point I, and h_I the average element length at point I. This error indicator proved to be remarkably insensitive to local variations in element size and shape, while still yielding the correct indicator values for physical phenomena of interest. We attribute this good performance to the smoothing effects of two averaging operations working simultaneously: the lumped mass-matrix and the point-lengths.

Faster construction of the new mesh.

The main CPU-intensive operations performed during one mesh change are finding the sides and the faces of each element, determining the refinement and coarsening patterns, correcting boundary points, and renumbering the elements. Although seemingly trivial, these operations account for a significant percentage of total CPU time. We developed new, optimal algorithms for them. Two examples are described here in more depth:

1) Determining the list of sides for new points

Given the side/element information, and a list of elements to be refined, a first set of sides on which new gridpoints need to be introduced is determined. In most cases, it will not lead to an admissible refinement pattern. Therefore, further sides are marked for the introduction of new points until an admissible refinement pattern is reached. This is done by looping several times over the elements, checking on an element level whether the set of sides marked can lead to an admissible new set of sub-elements. Practical calculations revealed that sometimes up to 15 passes over the mesh where required to obtain an admissible set of sides. An 80%-90% reduction in CPU was achieved by presorting the elements as follows:

- Add up all the sides marked for refinement in an element;
- If 0,1 or 6 sides were marked: do not consider further;
- If 4 or 5 sides were marked: mark all sides of this element to be refined;
- If 2 or 3 sides were marked: analyze in depth.

2) Element renumbering

In order to vectorize the element assembly as much as possible, the elements are renumbered, such that within each assembly pass a point is accessed only once by the elements. This renumbering has to take place after every mesh change. Before optimization, it took over 10% of the *total* CPU time for typical runs. The renumbering subroutine was optimized by working only on the remaining elements, and extensive scalar optimization, minimizing the number of operations and memory access. With the new renumbering algorithm, the CPU-time required for this operation dropped to less than 1%.

3.2.5 Recent Modifications to the H-Refinement Algorithm.

Over the past two years, we have significantly modified the adaptive finite element methodology for transient problems in 3-D [10]. Since for typical shock calculations mesh adaption takes place every 5 to 10 time steps, it has been concluded that every stage of the adaption process must be thoroughly optimized. The two areas that required the most intense optimization efforts were error indicators for grids with large local variations of element size and shape, and faster construction of the new mesh.

Improved error indicators.

As an error indicator we use a modified interpolation theory error indicator:

$$E^I = \sqrt{\frac{\sum_{k,l}(\int_\Omega N^I_{,k} N^J_{,l} d\Omega \cdot U_J)^2}{\sum_{k,l}(\int_\Omega |N^I_{,k}| \left[|N^J_{,l} U_J| + \epsilon \left(|N^J_{,l}||U_J|\right)\right] d\Omega)^2}}, \tag{3.6}$$

where N^I denotes the shape-function of node I. By dividing the second derivatives by the absolute value of the first derivatives, the error indicator becomes bounded, dimensionless, and the "eating up" effect of strong shocks is avoided. This error indicator has performed very well in 2-D over the years [8]. However, when first used in 3-D, it proved unreliable. The source of this seemingly inconsistent behavior was found to stem from the large *local* variations in element size and shape, as well as the number of elements surrounding a point encountered in typical 3-D unstructured grids. These wil produce large variations of the second term in the denominator that are not based on physics, but on the mesh structure itself. The solution was to modify this error indicator as follows:

$$E^I = \sqrt{\frac{\sum_{k,l}(\int_\Omega N^I_{,k} N^J_{,l} d\Omega \cdot U_J)^2}{\sum_{k,l}(\int_\Omega |N^I_{,k}||N^J_{,l} U_J| d\Omega)^2 + \epsilon MMAT_I h_I^{-2} |U_I|}}, \tag{3.7}$$

where $MMAT_I$ is the lumped mass-matrix at point I, and h_I the average element length at point I. This error indicator proved to be remarkably insensitive to local variations in element size and shape, while still yielding the correct indicator values for physical phenomena of interest. We attribute this good performance to the smoothing effects of two averaging operations working simultaneously: the lumped mass-matrix and the point-lengths.

Faster construction of the new mesh.

The main CPU-intensive operations performed during one mesh change are finding the sides and the faces of each element, determining the refinement and coarsening patterns, correcting boundary points, and renumbering the elements. Although seemingly trivial, these operations account for a significant percentage of total CPU time. We developed new, optimal algorithms for them. Two examples are described here in more depth:

a) Determining the List of Sides for New Points

Given the side/element information, and a list of elements to be refined, a first set of sides on which new gridpoints need to be introduced is determined. In most cases, it will not lead to an admissible refinement pattern. Therefore, further sides are marked for the introduction of new points until an admissible refinement pattern is reached. This is done by looping several times over the elements, checking on an element level whether the set of sides marked can lead to an admissible new set of sub-elements. Practical calculations revealed that sometimes up to 15 passes over the mesh were

required to obtain an admissible set of sides. An 80%-90% reduction in CPU was achieved by presorting the elements as follows:

- Add up all the sides marked for refinement in an element;
- If 0,1 or 6 sides were marked; do not consider further;
- If 4 or 5 sides were marked; mark all sides of this element to be refined;
- If 2 or 3 sides were marked; analyze in depth.

b) Element Renumbering

In order to vectorize the element assembly as much as possible, the elements are renumbered such that within each assembly pass a point is accessed only once by the elements. This renumbering has to take place after every mesh change. Before optimization, it took over 10% of the *total* CPU time for typical runs. The renumbering subroutine was optimized by working only on the remaining elements, and extensive scalar optimization by minimizing the number of operations and memory access. With the new renumbering algorithm, the CPU-time required for this operation dropped to less than 1%.

3.3 SHOCK INTERACTION WITH A GENERIC TANK.

The first simulation of shock diffraction about a complex-geometry three-dimensional structure conducted under this project was a simulation of shock interaction with a generic tank configuration (closely resembling the West German Leopard). Since the shock impinged head-on on the tank, a plane of symmetry exists and only half of the domain can be modelled.

Initial tests with the new three-dimensional code described above demonstrated its ability to capture moving and stationary shocks over three elements without loss of monotonicity. For this class of problems and the algorithm employed it was found that the following choice of refinement/coarsening parameters produced nonoscillatory shocks and rarefactions:

- refinement tolerance: $CTORE$=0.18
- coarsening tolerance: $CTODE$=0.09
- noise parameter: ϵ =0.12
- key variable: density
- refinement frequency: every 7 time steps
- number of protective layers: none
- Courant number of the hydro-solver: C = 0.45.

Figures 3-4 through 3-12 show the adapted computational grid and pressure contours at several times during the computation. Since it is difficult to visualize results in the computational volume, results will be presented only on the boundaries or on specified planes. The +X direction, the shock propagation direction (Figure 3-4), will be referred to as the axial direction, the +Y direction as the vertical direction, and the +Z direction as the cross-stream direction. Plane X-Y is the plane of symmetry, as shown in Figure 3-4. Since it was intended to integrate the solution to t=50 ms, the computational domain had to be significantly larger than shown in this figure: 20 m upstream of the tank (to allow for shock reflection), 25 m downstream of the tank, 15 m in the vertical direction and 20 m in the cross-stream direction. Past experience with 2-D simulations [4] demonstrated that advantage of the adaptive, unstructured grid approach vs. the structured grid approach when applied to shock propagation over large distances. The ability to adapt and refine only where needed was shown to be even more important for the 3-D simulations. The shocks developed in the computational domain are always captured as sharp discontinuities, demonstrating the effectiveness of the new methodology. The results (especially at later times) demonstrate the advantage of using an adaptive scheme, as the reflected 3-D shocks were sharply captured even after propagating significant distances. A similarly resolved shock computed with a fixed, structured mesh would have required maintaining a fine grid resolution everywhere in the computational volume, at a prohibitively high computational cost. Grid refinement is observed as the shocks propagate into new volumes, while grid coarsening is observed in areas already traversed by the shocks. As expected, the later time results exhibit significantly weaker shocks than observed in the past for corresponding 2-D simulations, due to three-dimensional expansion processes.

Figure 3-4 shows a superimposition of the pressure contours and the adapted mesh on the boundaries at t=0. A shock with an amplitude of 10 psi overpressure and low supersonic Mach number (1.14) was placed approximately 1.0 m upstream of the cannon. The initial mesh consisted of 71,219 points and 405,400 elements. Later in the computation, the average computational mesh consisted of approximately 230,000 points and 1.3 million tetrahedra.

The shock impinged on the cannon at t=3.0 ms (Figure 3-5), at which time a basically planar reflection was observed. Three-dimensional expansion processes would immediately relieve the high pressure reflected shock. Thus, at t=4.2 ms (Figure 3-6b), the three-dimensionally expanded shock was observed at a X-Y plane located 0.5 m from the plane of symmetry, while the amplitude of the reflected shock has been drastically reduced and was considerably lower than predicted by 2-D models. The computational mesh, demonstrated excellent adaptation to the 3-D shock (Figures 3-6a and 3-7a, at t=4.2 and 5.5 ms, respectively). Three levels of refinement are observed, with a minimum normal height of 0.6 cm. The shock is about to impinge on the front chassis of the tank at t=5.5 ms.

Nevertheless, the large tetrahedra ahead of the shock (Figure 3-7a), between the shock and the treads, were refined in preparation for shock arrival, and thus the refined mesh on the front chassis and treads. The pressure contours at this time (Figure 3-7b) show further expansion of the reflected shock from the cannon, although the reflected shock has not yet arrived to a X-Y plane located 1.5 m from the plane of symmetry.

The propagating shock hits the front chassis at t=5.9 ms. The adapted mesh and pressure contours on the tank surface, shown in Figures 3-8a and 3-8b, respectively, demonstrate the grid adaptation to flow gradients. In addition to the well-refined incident and reflected shocks, strong expansions are observed around all sharp corners. The incident shock is shown on the chassis and the sides of the tank. Several 3-D reflected shocks are observed. Figures 3-8c and 3-8d show pressure contours on three X-Y planes, located at Z=0.5 m, Z=1.5 m and Z=2.75 m, respectively. The results at all planes exhibit an almost spherical reflection (shock 1) from the slanted front of the chassis (shown in Figure 3-8a). The reflected shock has impacted on the ground. Figure 3-8e shows a superimposition of the pressure contours on the boundaries and two X-Y planes located at Z=1.5 m and Z=2.75 m from the plane of symmetry (shown in the figure on the left and right sides, respectively). Although the incident shock was planar and the reflection in the vertical direction was fairly uniform above the chassis, the reflection pattern below the chassis is more complex. While the incident shock passed under the tank unimpeded (Figures 3-8c and 3-8d), strong reflections from the treads are observed (Figure 3-8e). The higher stagnation pressures ahead of the treads resulted in greater upstream reflection distances than near the plane of symmetry, where the incident shock was free to propagate under the tank and the observed upstream reflection is from the chassis. It should be noted that the outline of the shocks shown in Figure 3-8e represent the outer surface of a single, very complex three-dimensional reflected shock (called shock 1). New graphic tools are needed to exhibit the three-dimensional nature of these shocks. We intend to develop such capabilities in the near future.

The reflected shocks from the treads are three-dimensional and later expand to fill the space under the chassis. Thus, at later times, a more uniform (i.e., planar) reflection front was observed to propagate upstream (Figure 3-10b). The reflection of shock 1 from the ground (shock 2) impinged on the treads and reflected (shock 3 in Figure 3-8b). While the incident shock propagated past the sloped-down panel of the front chassis, a downward propagating shock reflected and tailed the incident shock (shock D in Figure 3-8c). A strong expansion around this corner is shown in Figures 3-8c and 3-8d. Examination of these figures (note Figures 3-8b and 3-8e) indicates that the reflected shock from the chassis (shock 1), with a fairly high pressure amplitude, impinged on the cannon, exerting additional bending moments.

The incident shock impacted on the turret at about t=11.9 ms (Figure 3-9a). Strong reflection from the turret (shock T_1) is observed at t=12.87 (Figure 3-9b). Since the rarefaction waves propagated from the turret edges to the center, the largest pressure amplitude, and hence furthest upstream reflection distance, was observed on the chassis at the plane of symmetry (Figure 3-9b). Notice that at this time the incident shock continued forward propagation in the narrow spacing between the turret and the chassis, and has almost impacted on the cylindrical turret base.

The complex system of three-dimensional shocks shown in Figures 3-8 continued their evolution. The primary reflected shock (shock 1) continued expanding, while the pressure rise across the shock continued to decrease. The decay rate was significantly higher than for corresponding 2-D calculations, no doubt due to the added expansion around the tank in the cross-stream (Z) direction. While shock 3 continued expanding ahead of the treads (Figure 3-9b), shock 2 (under the chassis) reflected from the chassis (shock 2a in Figure 3-9c), and shock D reflected from the ground, propagated up and was about to impact on the bottom of the tank.

The incident shock reflected from the front of the cylindrical turret base at t=13.0 ms. The adapted mesh and pressure contours figures at t=15.53 ms, Figures 3-10a and 3-10b, respectively, demonstrate continued mesh adaptation to all flow gradients, shocks as well as rarefactions. Figures 3-10b and 3-11 (and many others not shown here) demonstrate strong reflection (shock T_2) from the turret base at the plane of symmetry. The shock amplitude and reflection distance decreased with increased angle from the plane of symmetry, as predicted by previous simulations of planar shock interaction with a cylinder [4]. Similarly, the reflection from the turret (shock T_1) expanded spherically. Figure 3-11 (at t=15.53 ms) attempts to present the spherical expansion of shock T_1, as demonstrated by the pressure contours on the plane of symmetry (an X-Y plane), the tank chassis (an X-Z plane), and a Y-Z plane at 2.0 m (shock T_{1a}). Meanwhile, complex shock evolution continued under the tank, as shown in Figure 3-10c, for a X-Y plane at Z=0.5 m. While the primary reflected shock (shock 1) continued upstream reflection, shock 2 expanded in the vertical direction. Its reflection, combined with the reflection of shock D, from the down-sloped surface at the front of the tank, is shock 2b. The reflection of the curved shock 2a (Figure 3-9c) from the ground is shock 2c, while shock 2d is the reflection of shock D from the bottom of the tank and the ground.

The calculation was continued to later times. Due to the complexity of the evolved solution, the latest results presented are for t=19.69 ms, when the shock was still propagating over the turret (Figure 3-12a). The back-view (Figure 3-12b) shows a nice expansion of the shock behind the circular turret base, and demonstrates the sharp, nonoscillatory incident and reflected shocks.

Total computation time (to t=25 ms real time) was approximately 23-25 CPU hours on a 128 MWords Cray 2 computer. Computation time per node per time step was approximately 180 microseconds, including the refinement/deletion process, which added approximately 20-25 percent to the overall computation time.

Finally, it is noted that a deficiency of the unstructured grid schemes is the large memory overhead required for the three-dimensional algorithm: approximately 380 words per node. As noted above, this overhead can be reduced to less than 250 words per node by re-computing certain geometric variables rather than storing them. Nevertheless, such an overhead necessitates the usage of the large static-memory, relatively slow, Cray 2 (128 MWords) supercomputer for most practical 3-D simulations. To alleviate this problem, a new dynamic domain-splitting type algorithm will be developed in the near future. In this algorithm, the computational domain will be split at each refinement/deletion cycle to multiple domains. This will allow the usage of faster, smaller static-memory computers with a solid-state-disc, such as the Cray Y-MP.

3.4 SHOCK INTERACTION WITH A T-62 TANK.

The second simulation conducted under this project was the simulation of 3-D shock diffraction phenomena around a modern main battlefield tank, in this case a T-62 tank. For this class of problems and the algorithm employed, past experience (and experience gained during this study) indicated that the following choice of refinement/coarsening parameters produced the best results:

- refinement tolerance: $CTORE$=0.095
- coarsening tolerance: $CTODE$=0.0675
- noise parameter: $\epsilon = 0.28$
- key variable: density
- refinement frequency: every 5-7 time steps
- number of protective layers: none
- Courant number of the hydro-solver: $C = 0.8$.

The results of the two simulations conducted in which a strong shock impacted either back-on or side-on a T-62 modern main battlefield tank, are shown in Figures 3-13 – 3-19. The pressure contour results are shown on the surfaces only in the immediate vicinity of the tank, in order to reduce the dump-files size (dumped every 10 time steps), and hence reduce field transfer and post-processing time.

Figures 3-13a-d show several views of the solid body model and the surface triangulation. While the turret data were available from a CAD-CAM system (BRL-CAD), all other

data were measured directly from the tank. The generation of the surface and volume grids took three days, demonstrating the versatility of the grid generation package (FRGEN3D, PREGEN3D, PREBACK). It should be noted that once the surface triangulation is performed, the generation of the volume mesh, using the advancing front algorithm [12,17] is completely automatic. Generating such a grid with a structured grid approach would have taken significantly longer.

3.5 BACK IMPACT.

The first simulation modeled shock impact on the tank from the back. Taking advantage of the symmetry of this problem, the X-Y plane was defined as a plane of symmetry. The initial grid included only 20,591 points, 100,343 elements, and 7,816 surface points. The incident shock was placed (t=0) 1.5 meters behind the tank. After adapting to the initial shock using only two levels of refinement, the number of points increased to 41,846, the number of elements to 221,482 and the number of surface points to 9,159. During the computation, the number of grid points increased to about 285,000 (the maximum we could fit in a Cray-2 with an allowable memory usage of 100 million words), the number of elements to about 1.8 million, and the number of surface points to about 40,000.

Supersonic boundary conditions were imposed on all outflow boundaries due to the high Mach number of the flow behind the shock. Flow conditions on the upstream boundary were prescribed. Symmetric conditions were posed at the plane of symmetry. Tangential boundary conditions were imposed on the tank. The computational domain stretched a distance of 100 m in the axial direction (+X), 25 m in the transverse direction (+Z), and 25 m in the vertical direction (+Y). The minimum tetrahedron normal size allowed after two refinements was 0.5 cm. Maintaining this resolution with a structured, fixed-mesh algorithm on such a large computational volume, even for a multi-zone (multi-block) approach, would have required a significantly larger (100 times larger) computational grid, thus significantly increasing computational costs and memory requirements.

Shock evolution around the tank during the diffraction phase is shown in Figures 3-14a through i. Figure 3-14a shows pressure contours on the tank's surface and the plane of symmetry after 200 time steps. Figures 3-15a and b show pressure contours at this time on two X-Y planes located at Z=0.5 and 1.5 meters, respectively. The results show the almost-planar reflection of the shock from the tail of the back-deck. Very little pressure relief through the expansion of rarefaction waves emanating from the corners is observed, due to the very short time after shock impact (Figure 3-15a). Thus, the reflected pressure amplitude at the center of the back-plane was in excellent agreement with the corresponding value obtained via the solution of the 1-D Riemann problem. Strong planar shock reflection is also observed from the back of the ammunition train. A significantly

weaker spherical reflection was observed from the curved back of the treads (Figure 3-15b). Shock propagation over the back-deck shows no increase in pressure (from the incident pressure value) as the incident shock is normal to the back-deck and passed the sharp 90° back-deck corner without producing a Mach-stem.

Figure 3-14b at 400 steps shows a mirror imaged view of pressure contours on the surface of the tank. Pressure contours on the ground show the reflected shock from the back-plane (still very weak due to the mostly planar reflection), spherical shock reflection from the back of the treads, and shock wave focusing between the treads and the ground. This focusing effect produced the highest overpressure values obtained in this computation. This figure also exhibits one of the more interesting processes observed in this computation: shock diffraction and focusing around and between the wheels. High overpressure values were obtained whenever the shock wave, which propagated normal to the primary axis of the wheels, was focused between the treads and a wheel. Hence a system of reverberating shocks between the wheels and between the wheels/treads/wheel cover assembly was formed. Similarly, high overpressure values were obtained as the shocks converged within the downstream arcs of the cylindrical reams. Conversely, low overpressures were obtained within the upstream arcs of the reams, contributing to a high torque force on the wheels. Figures 3-14c and 3-15c show this phenomenon at t=600 steps. These results also show the (by now) almost cylindrical shock reflection from the back-plane with a large pressure imprint on the ground (Figure 3-15c). We observe here the initiation of a Mach stem, with the stem, the original reflected shock, its reflection from the ground and the resulting triple point, all clearly defined.

The incident shock impacted on the turret at t=800 steps (Figure 3-14d). The planar data at Z=1.0 m (Figure 3-15d) demonstrate the rise (off the ground) of the triple point and the truly three-dimensional character of the Mach stem, as the pressure is observed to decay behind the stem with increased distance in the transverse direction. Analysis of pressure data at other planes showed that the overpressure value behind the stem was fairly uniform in the +Z direction up to Z=1.2 m, about the width of the back-deck, and decayed rapidly afterwards. This conclusion was supported by later results (Figure 3-14e at 1000 steps, and Figures 3-15e-g at 1200 steps). Another interesting 3-D shock reflection phenomenon was the reflection from the treads-ground corner. The high pressure relief is again truly three-dimensional, as seen in the pressure contours data on the ground, the treads, and the different planar data (Figures 3-15c through 3-15f at t=1200 steps).

Complex shock diffraction processes were observed due to the shock interaction with the turret. Figure 3-14e at 1000 steps, and Figures 3-14g, 3-15e, f and g at 1200 steps and later results demonstrate that large amplitude reflections were obtained on turret surfaces normal or almost normal to the flow, while weak reflections and rarefactions were observed

at turret surfaces parallel or inclined at small angles to the flow. The initial reflection from the turret looked like a bow shock at and near the plane of symmetry (Figures 3-14e and 3-15e), while no reflection was observed near the edge (in the +Z direction) of the turret, where the incident shock was parallel to the turret surface (Figures 3-15g and h at Z=1.0 m and 1.5 m, respectively). At later times (Figures 3-14f through h), pressure relief near the top inhibited the upstream propagation of the reflected shock, while the shock immediately above the back-deck propagated a much larger distance upstream, forming a very complex 3-D shock with a strong spatial dependence. Indeed, pressure data at points on top of the back-deck located only about 40-60 cm apart experienced significantly different reflected shock amplitudes, as will be shown later.

These results demonstrate that a precise geometric description of the complex geometry 3-D body is required to obtain the correct load on the structure. A simplified simulation of this process using a block to represent the turret would yield erroneous loading on the deck top: a critical requirement.

The primary reflected shock from the back-deck has reached an apparent "quasi-steady" stand-off distance after about 2,200 time steps. This stand-off distance is critically dependent on the exact geometric description of the deck-treads-side traines assembly that determines the percentage of blocked area. The stand-off distance, in turn, determines the lift and drag forces on the tank during the diffraction and drag phases.

The results at later times (after the shock propagated past the turret) are shown in Figure 3-14i (2,800 time steps). These results (and others not shown here) indicate that the shock that emerged from under the deck (up-front), led the shock that propagated above and around the turret by as much as one meter. This higher propagation velocity and stagnation pressure under the tank resulted from the propagation of the incident shock across a sloped surface at the bottom back of the deck, a surface that acted as a (2-D) compression ramp. The results also show the complex quasi-steady reflected 3-D shock upstream of the turret. Flow expansion downstream of the tank's back-plane has accelerated the flow to transonic speeds near the back-deck, and to supersonic speeds high above the deck. Thus the observed compression wave near the bottom of the turret, and the oblique shock near the top. Naturally, this phenomena varied in the transverse direction due to the reduced blockage by the turret.

Figures 3-16a through d show superpositions of the pressure contours and adpated mesh after 200, 400, 600, and 1000 time steps, respectively. These results demonstrate the excellent shock adaption capability of the new algorithm, as observed on all surfaces. Investigation of several planar surfaces demonstrated equally successful adaption in the volume. Only two levels of refinement were utilized here. All shocks are observed to be

fully refined and are captured over two to three elements. No wiggles are observed in the solution.

The results presented here show the shock evolution around the tank only during the diffraction phase. The computation was actually continued to a later time, when the shock has propagated a long distance (about 30 meters) downstream. Even after propagating such a long distance, all shocks, reflected or transmitted, were still captured as sharp, nonoscillatory discontinuities, with a minimum tetrahedron normal size of less than 1.5 cm. These results demonstrate the advantage of the adaptive, unstructured grid approach over fixed-grid, structured codes (i.e., significant reductions of CPU time and memory requirements). Utilizing these schemes to propagate a shock over such long distances with the presecribed resolution may be prohibitively expensive.

The computation of more than 7,000 time steps consumed approximately 60 CPU hours on a Cray-2.

3.6 SIDE IMPACT.

The third computation simulated shock impingement side-on on the same tank. Figures 3-17a through c show the superimposed mesh and pressure contours at 0, 300, and 600 time steps. Excellent grid adaption was obtained. The Gourard shaded pressure contours at 300, 600, and 800 time steps (Figures 3-18a, c and d, respectively), and the enlarged view of the pressure contours results between wheels three and four at 300 steps (Figure 3-18b) demonstrate, in addition to the high fidelity of the computations, many interesting shock diffraction phenomena. Among them:

a) The stand-off distance of the quasi-steady reflected shock was significantly smaller than for the back-on impingement. This reduction results from the large spacing between the wheels that allows the transmission of a significant portion of the incident shock energy. This phenomenon points out the importance of the accurate description of the complex geometry wheels-treads-deck-cover assembly. Improper geometric modeling that, for instance, will over-restrict the flow (i.e., smaller spacing), will result in higher percentage of reflected energy, and hence higher reflected pressure amplitude; this, in turn, will result in higher drag force exerted on the vehicle.

b) Higher stagnation pressure under the deck than above the turret resulted in higher propagation speed below, and hence, generated a lift force on the tank.

c) The integrated drag force on the turret was higher than for the back-on attack. The combined higher lift and drag forces will increase the probability of the tank overturning. Nevertheless, the load exerted on the top of the back-deck was significantly diminished, as the reflected shock amplitude decreased; very little reflection from the turret was observed on the back-deck near the centerplane after 800 steps.

d) Due to shock reflection from the turret and its impingement on the cannon, a large bending moment was exerted on the cannon.

e) Full stagnation was obtained in front of the blocked wheels (Figures 3-18c and d). The shock traversed the outside of the wheels at grazing angles and was only partially stagnated on the side of the main deck.

Pressure-time histories at several stations were compared to experimental data obtained in a field test. The agreement between the measured and predicted data was very good.

The computation of the diffraction phase for the side-on impingement consumed approximately 16 CPU hours on a Cray-2.

3.7 COMPARISON OF PRESSURE-TIME HISTORIES.

Comparisons of pressure-time histories between the results obtained for the back-and side-impact simulations are shown in Figures 3-19a-i for several locations around the tank. All pressure and time data shown are nondimensional. Figure 3-19a shows pressure-time histories at the back-end of the tank. The initial back-impact shock completely stagnated to a value that was in very good agreement with both 1-D analytical analysis and the experimental data. The small pressure increase at about t=5 is the reflected wave from the turret. *In comparison, the shock for the side impact traversed the back-plate at a* grazing angle and no reflection or pressure increase was observed.

The next four figures show pressure-time histories at four stations on the back-deck. The pressures-contours data (Figures 3-14 and 3-15) demonstrate the large spatial pressure variation on the back-deck due to the reflected shock from the turret. Figures 3-19b and c show pressure-time histories at two stations on the centerline, one (station 29) fairly close to the turret, the other (station 34) only 0.8 m further upstream. For the back-impact shock, the reflected shock amplitude was reduced by about a factor of three over this distance (18.2 at station 29 vs. 6.5 at station 34). For the side-impact, the differences are not as significant, and in fact, the station further from the turret demonstrates a second shock that resulted from shock diffraction through the spacing between the ammunition traines and the back-deck. Stations off the centerline demonstrate shock overpressure dependence on distance from both the turret and the centerline. Pressure data at station 43, located 30 cm upstream of station 34, and 50 cm off centerline, demonstrate a significant reduction in reflected shock overpressure; the peak value was about 4.5 times lower than that obtained at a station located on the centerline at identical distance from the turret. Pressure results at station 57 (Figure 3-19e), located about 1.0 m further upstream and 20 cm closer to C.L., show further reduction of the reflected shock amplitude. The results for the side-impact show a second compression resulting from shock diffraction through the

spacing between the ammunition traines and the back-deck. These results, combined with the pressure-contour results (Figures 3-14 and 3-15), demonstrate the need to accurately model the turret. Modeling of the turret as a square block would have resulted in erroneous load distribution on the back-deck, and hence, erroneous damage assessment.

Figure 3-19f shows pressure-time histories at a station located close to the commander's hatch (on the turret) on a surface almost normal to the side-impact shock, but about parallel to the back-impact shock. The geometry hence dictates a reflected shock with a fairly large amplitude for the side-impact case, in contrast to an almost grazing angle and zero reflection for the back-impact shock.

Pressure data at station 10 (Figure 3-19g), located on the front forward-sloping portion of the turret on the centerline, show expansion of the shock coming from the back, with a lower pressure than the incident pressure. The data for the side-impact show that although the station was located on a plane almost parallel to the flow, shock diffraction around the rounded turret increased the pressure due to the formation of a Mach stem. Figure 3-19h, for station 3, located on the down-sloped front deck just below the cannon, shows a fairly significant shock reflection from the cannon for the side-impact case. The results for the back-impact only show the arrival of the incident, expanding shock.

Finally, pressure-time histories for station 84 (Figure 3-19i), located under the tank on the centerline at about two-thirds the length from the front, show (for the back-impact case) the arrival of the increased-amplitude shock, and a smooth decay afterwards. The shock amplitude increased due to the compression by the sloped portion of the back-deck and the formation of a Mach stem as the shock propagated along the bottom of the tank. For the side-impact the solution is even more complex. Since this station was located behind a wheel, it was not directly influenced by the incident shock but rather by the diffracted shocks between the wheels. The predicted oscillations that followed were the diffraction of the incident shock entering the cavity under the deck through openings between other wheels. Finally, the large pressure increase at about t=8 was the shock reflection from the downstream wheels.

3.8 SHOCK INTERACTION WITH A MISSILE IN FLIGHT.

The last 3-D shock diffraction computation conducted under this project simulated shock interaction at an angle of 45° with a missile in flight (at an angle of 2°). The results are shown in Figure 3-18. Here we note that: a) due to the 3-D nature of the shock diffraction process, strong 3-D rarefaction effects are observed on the surface of the missile; b) the slope discontinuities between the stages produced rarefaction waves; c) strong overpressure relief was observed at angles higher than 30°; d) high overpressure values were limited to the cone zone; and e) excellent shock adaption and resolution were

obtained at all times; all shocks were captured as sharp discontinuities, without producing pre- or post-shock oscillations.

3.9 SUMMARY AND CONCLUSIONS.

This section describes experience gained in applying a recently developed three-dimensional adaptive finite element shock capturing scheme on unstructured tetrahedral grids, to the simulation of shock wave diffraction phenomena around complex-geometry three-dimensional structures. The 3-D surfaces were defined using a new CAD-CAM-like user-friendly solid body generator (PREGEN3D) that includes a new automatic background-grid generator. The volumetric grid generation (tetrahedra) from the surface triangulation was accomplished using the advancing front method, and was rated at about 25,000 tetraheda per minute on the Cray-2. The computation was initiated by imposing the boundary and initial conditions; only two levels of refinement were used to refine the shock at its initial position. The resolution and fidelity of the simulated shock wave diffraction phenomena, performed via the solution of the transient compressible Euler equations, were enhanced by the application of the classic h-enrichment/coarsening grid adaptation scheme, with density as the critical adaptation parameter.

The 3-D methodology was applied in this project to the simulation of shock diffraction processes around several three-dimensional structures: a generic modern main battlefield tank, a T-62 tank, and a typical missile in flight. The results shown in this section demonstrate the successful application of the new 3-D adaptation procedure to shock interaction with curved surfaces: a new capability. Excellent shock adaptation and resolution were obtained at all times. All shocks were captured as sharp discontinuities, without producing pre- or post-shock oscillations. Several interesting three-dimensional shock diffraction processes were identified and discussed. Among them are the time evolution of three-dimensional Mach-stems, 3-D shock wave focusing and diffraction within corners and within/between the wheels and wheels/treads/cover assembly, etc. The results demonstrate that correct load determination requires the precise geometric description; simplified 2-D simulations or even 3-D computations that use a simplified geometric description (such as representing the turret as a square block) would yield erroneous results. Among the practical results obtained and discussed were the increased roll-over probability for a side-impact over a back-impact, and the very high instantaneous forces exerted on some surfaces due to the high-amplitude reflected shocks. Finally, the results demonstrate the robust performance of the method and show, at least for the present application and probably for other strongly unsteady flows as well, considerable savings in both CPU-time and storage over fixed-mesh structured grid schemes.

3.10 REFERENCES.

[1] J.D. Baum, S. Eidelman and D.L. Book - Numerical Modeling of Shock Wave Interaction with Conical Blast Shields; Proceedings of the 9th *International Symposium on Military Applications of Blast Simulation*, Oxford, U.K., (1985).

[2] J.D. Baum and S. Eidelman - Time-Dependent Three-Dimensional Simulation of Shock Wave Interaction with a Cylindrical Cavity; Proceedings of the *International Symposium on Computational Fluid Dynamics*, Sydney, Australia, August 24-27, (1987).

[3] R. Löhner, K. Morgan, J. Peraire and O.C. Zienkiewicz - Finite Element Methods for High Speed Flows; AIAA-85-1531-CP (1985).

[4] R. Löhner, K. Morgan, J. Peraire and M. Vahdati - Finite Element Flux-Corrected Transport (FEM-FCT) for the Euler and Navier-Stokes Equations; ICASE Rep. 87-4, *Int. J. Num. Meth. Fluids* 7, 1093-1109 (1987).

[5] S.T. Zalesak - Fully Multidimensional Flux-Corrected Transport Algorithm for Fluids; *J. Comp. Phys.* 31, 335-362 (1979).

[6] D.L. Book, J.P. Boris and K. Hain - Flux-Corrected Transport. II. Generalizations of the Method; *J. Comp. Phys.* 18, 248 (1975).

[7] J.P. Boris and D.L. Book - Flux-Corrected Transport. III. Minimal-Error FCT Algorithms; *J. Comp. Phys.* 20, 397-431 (1976).

[8] J.D. Baum and R. Löhner - Numerical Simulation of Shock-Elevated Train Interaction Using an Adaptive Finite Element Shock Capturing Scheme; AIAA-89-0653 (1989).

[9] J.D. Baum, R. Löhner and E. Loth - Numerical Simulation of Shock Interaction with Complex Geometry Canisters; in *Current Topies in Shock Waves*; American Institute of Physics (Y. Kim ed.), New York (1989).

[10] R. Löhner and J.D. Baum - Numerical Simulation of Shock Interaction with Complex Geometry Three-Dimensional Structures Using A New Adaptive H-Refinement Scheme on Unstructured Grids; AIAA-90-0700 (1990).

[11] A.S. Arcilla, J. Häuser, P.R. Eiseman and J.F. Thompson eds. - *Numerical Grid Generation in CFD and Related Fields*; Elsevier (1991).

[12] R. Löhner and P. Parikh - Three-Dimensional Grid Generation by the Advancing Front Method; *Int. J. Num. Meth. Fluids* 8. 1135-1149 (1988).

[13] R. Löhner - An Adaptive Finite Element Scheme for Transient Problems in CFD; *Comp. Meth. Appl. Mech. Eng.* 61, 323-338 (1987).

[14] J. Peraire, J. Peiro, L. Formaggia, K. Morgan and O.C. Zienkiewicz - Finite Element Euler Computations in Three Dimensions; AIAA-88-0032 (1988).

[15] R. Löhner and J.D. Baum - Adaptive H-Refinement on 3-D Unstructured Grids; submitted to *Int. J. Num. Meth. Fluids* (1991).

[16] R. Löhner - Adaptive H-Refinement on 3-D Unstructured Grids for Transient Problems; AIAA-89-0365 (1989).

[17] R. Löhner - Some Useful Data Structures for the Generation of Unstructured Grids; *Comm. Appl. Num. Meth.* 4, 123-135 (1988).

[18] R. Löhner, P. Parikh and C. Gumbert - Some Algorithmic Problems of Plotting Codes for Unstructured Grids; AIAA-89-1981-CP (1989).

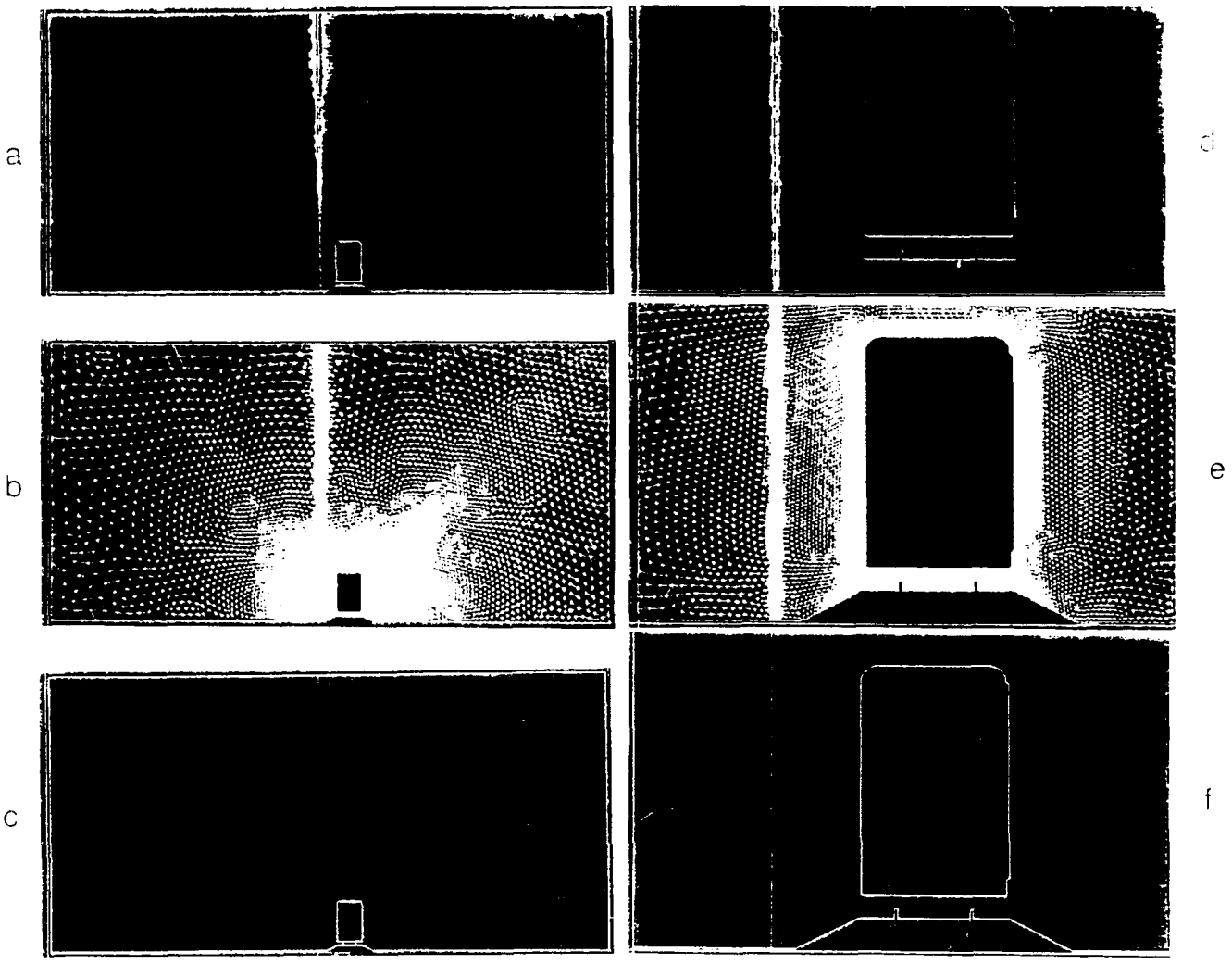

Figure 1-1. Initial Mesh Refinement Levels, Computational Grid and Pressure Contours for the Complete Computational Domain (Figures 1a to 1c), and for an Expanded Zone Near the Box (Figures 1d to 1f).

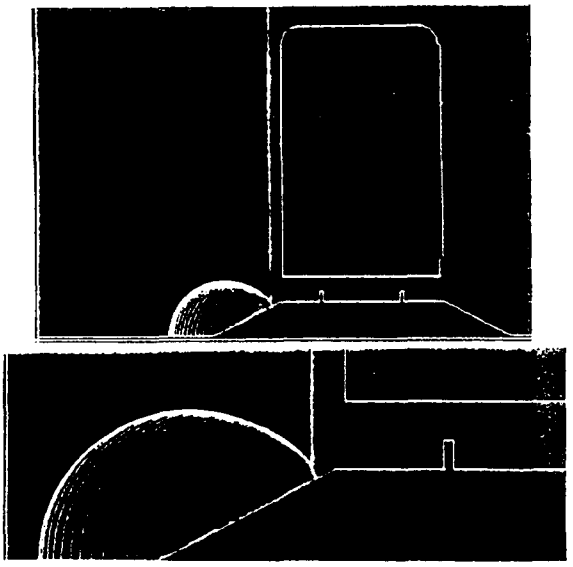

Figure 1-2. Expanded Views of Pressure and Density Contours Around the Box. t=0.4.

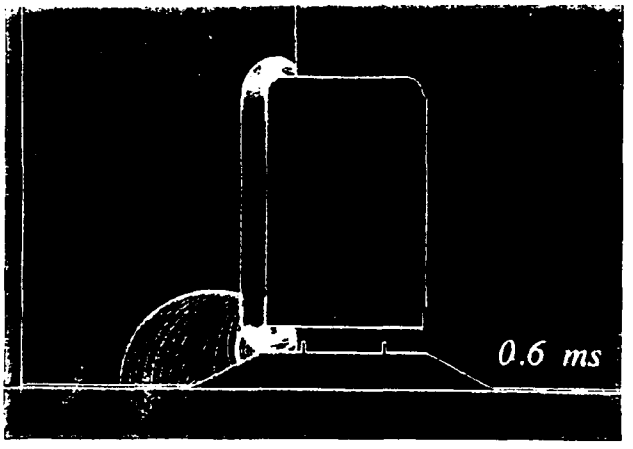

Figure 1-3. Expanded View of Pressure Contours Around the Box, t=0.6.

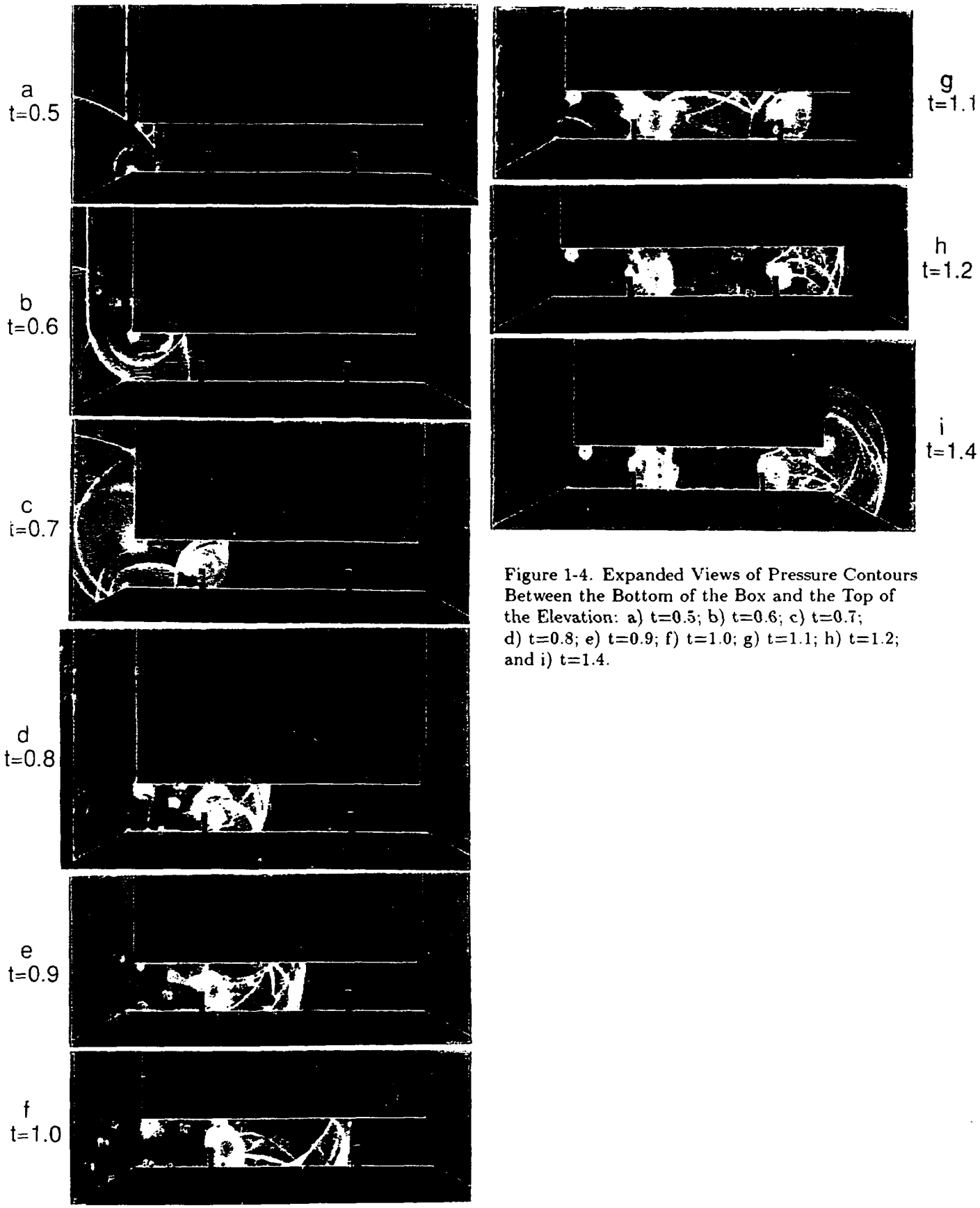

Figure 1-4. Expanded Views of Pressure Contours Between the Bottom of the Box and the Top of the Elevation: a) t=0.5; b) t=0.6; c) t=0.7; d) t=0.8; e) t=0.9; f) t=1.0; g) t=1.1; h) t=1.2; and i) t=1.4.

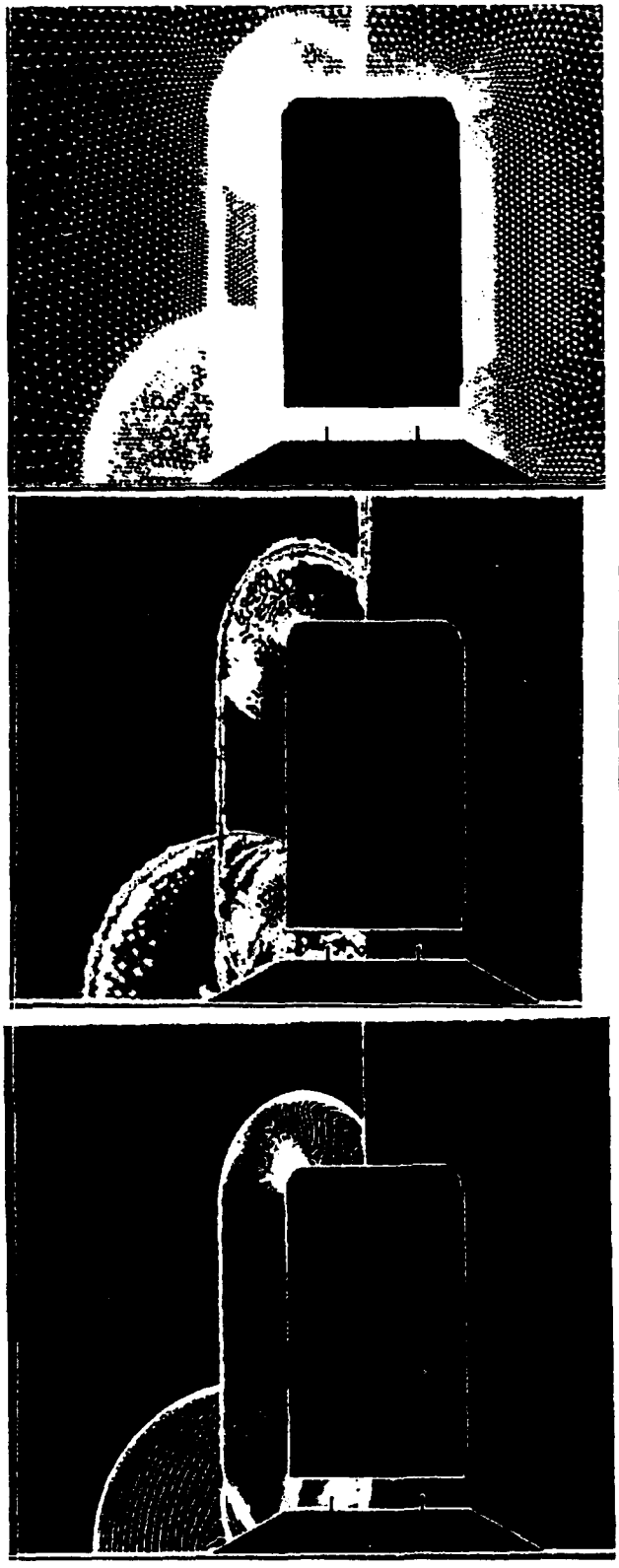

Figure 1-5. Expanded Views of Computational Grid, Mesh Refinement Levels, and Pressure Contours Around the Box, t=0.8.

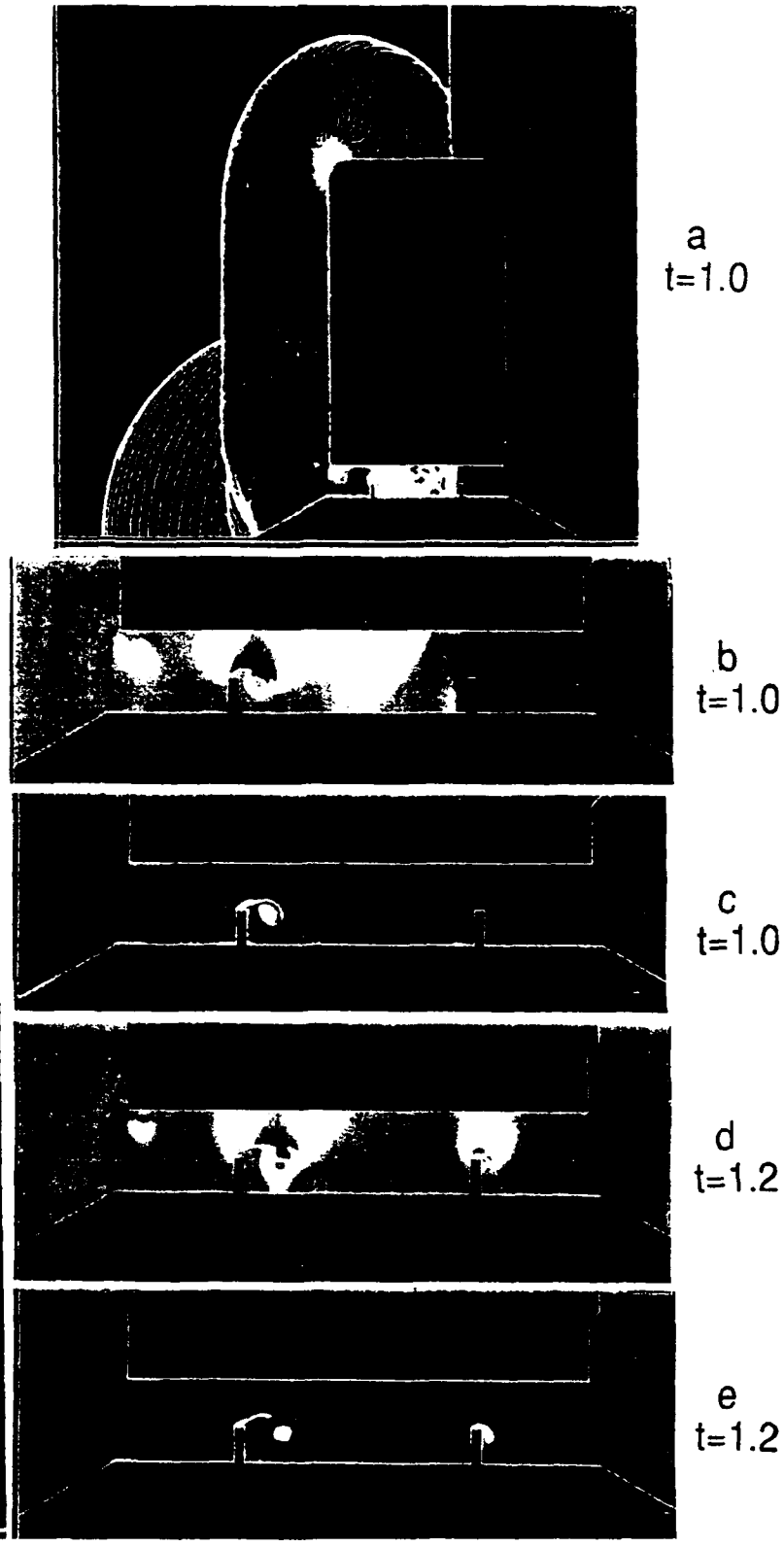

Figure 1-6. Expanded Views of Pressure (a), Mach Number (b) and Vorticity Contours (c) Around the Box at t=1.0, and Mach Number (d) and Vorticity Contours (e) at t=1.2.

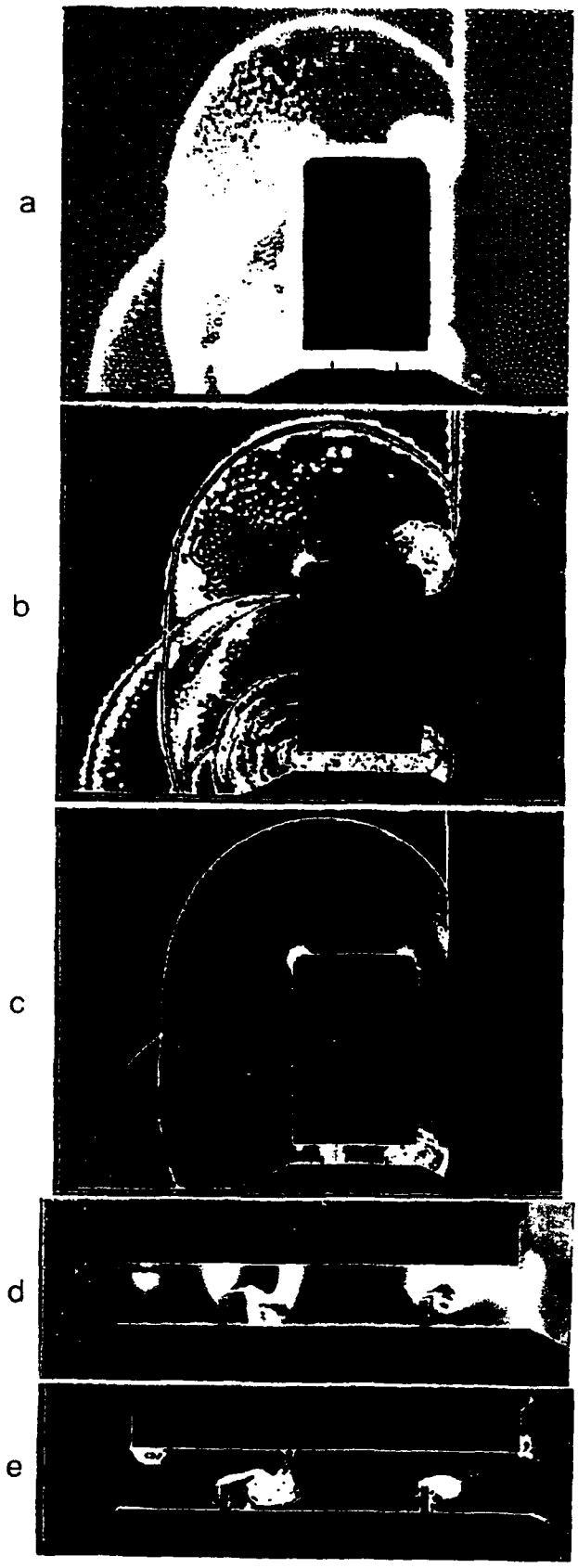

Figure 1-7. Expanded Views of Computational Grid (a), Mesh Refinement Levels (b), Pressure (c), Mach Number (d), and Vorticity Contours (e) Around the Box, t=1.4.

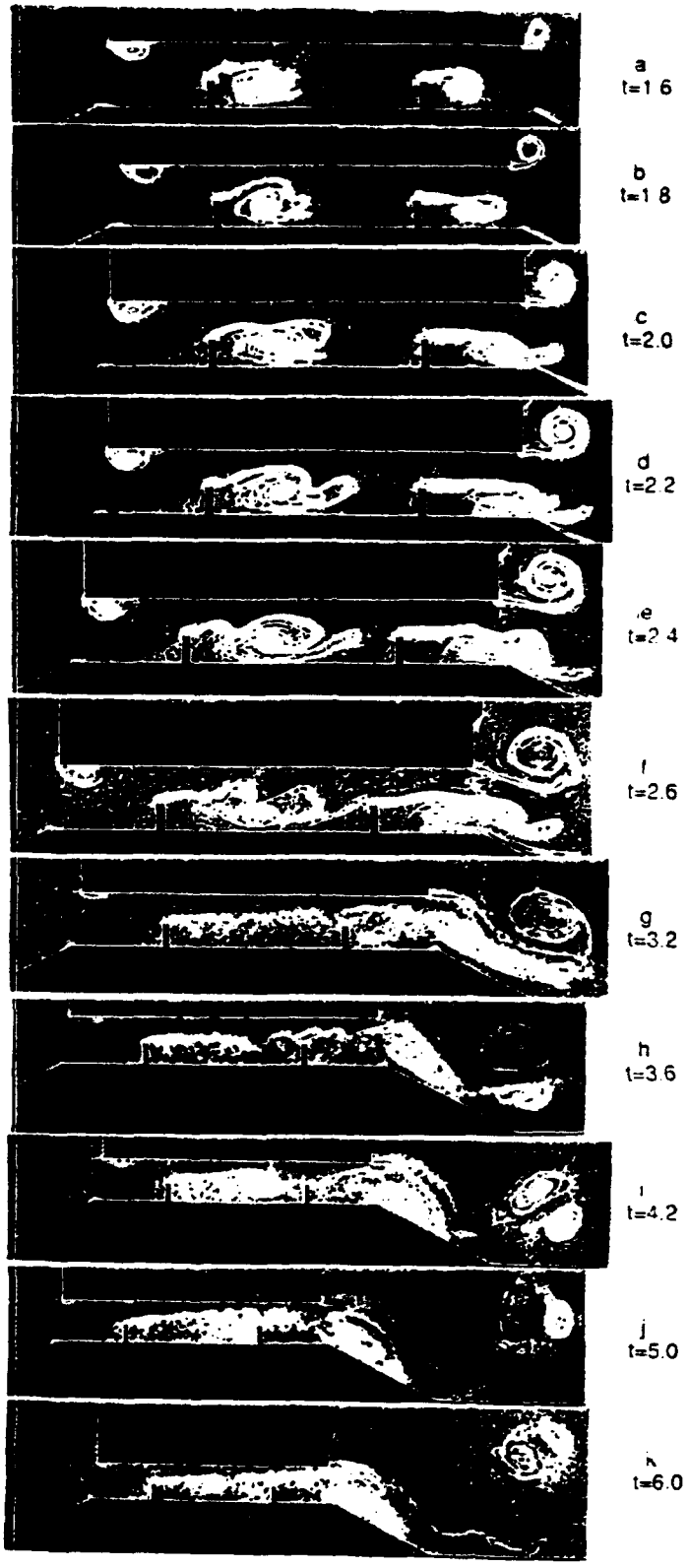

Figure 1-8. Expanded Views of Vorticity Contours Between the Bottom of the Box and Top of the Elevation; a) t=1.6; b) t=1.8; c) t=2.0; d) t=2.2; e) t=2.4; f) t=2.6; g) t=3.2; h) t=3.6; i) t=4.2; j) t=5.0; and k) t=6.0.

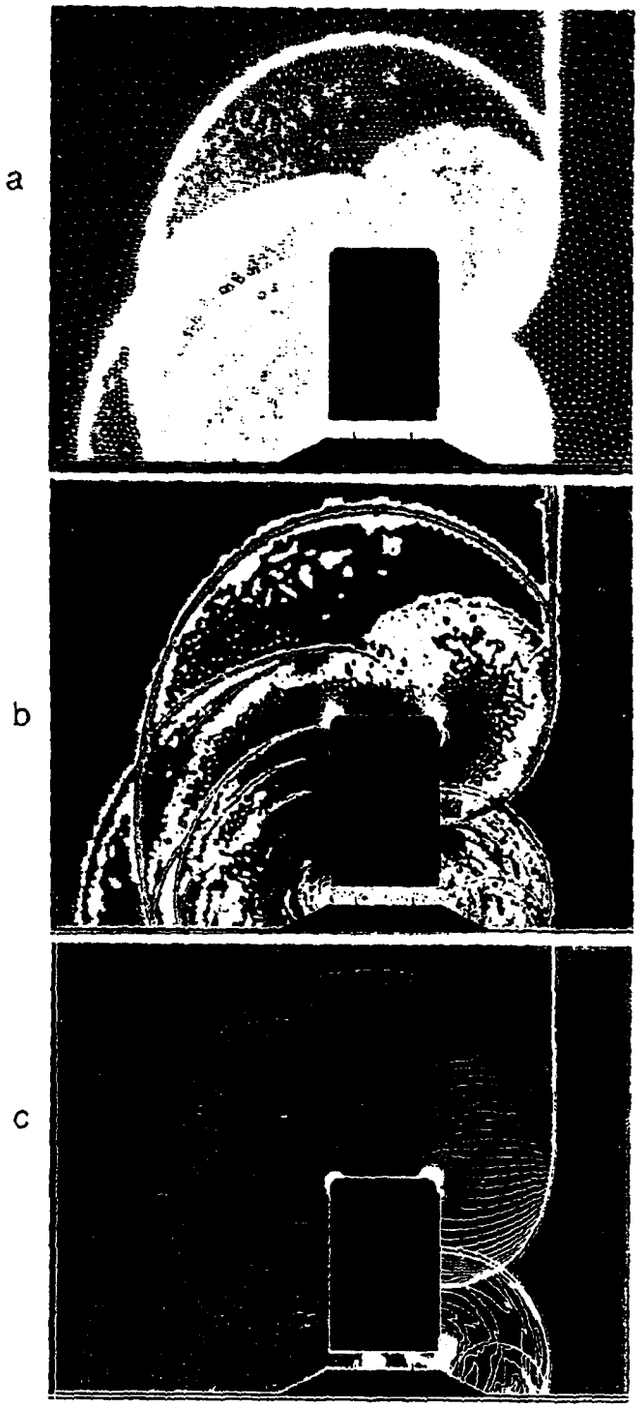

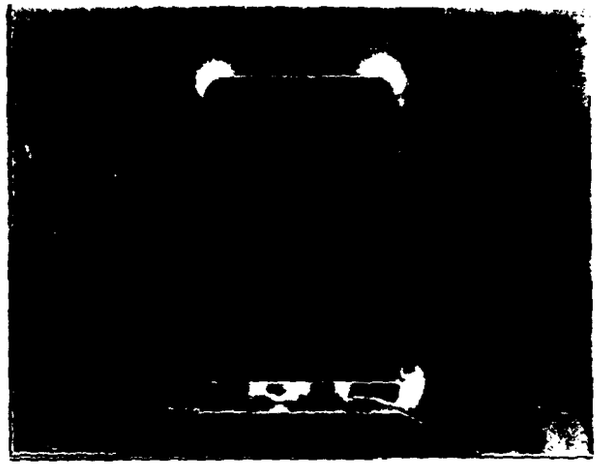

Figure 1-9. Expanded Views of Computational Grid (a), Mesh Refinement Levels (b), and Pressure (c) and Mach Number Contours (d) Around the Box, t=2.4.

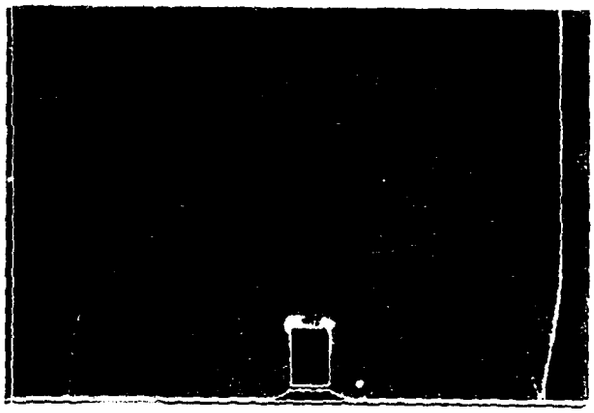

Figure 1-10. Pressure Contours Around the Box, t=6.0.

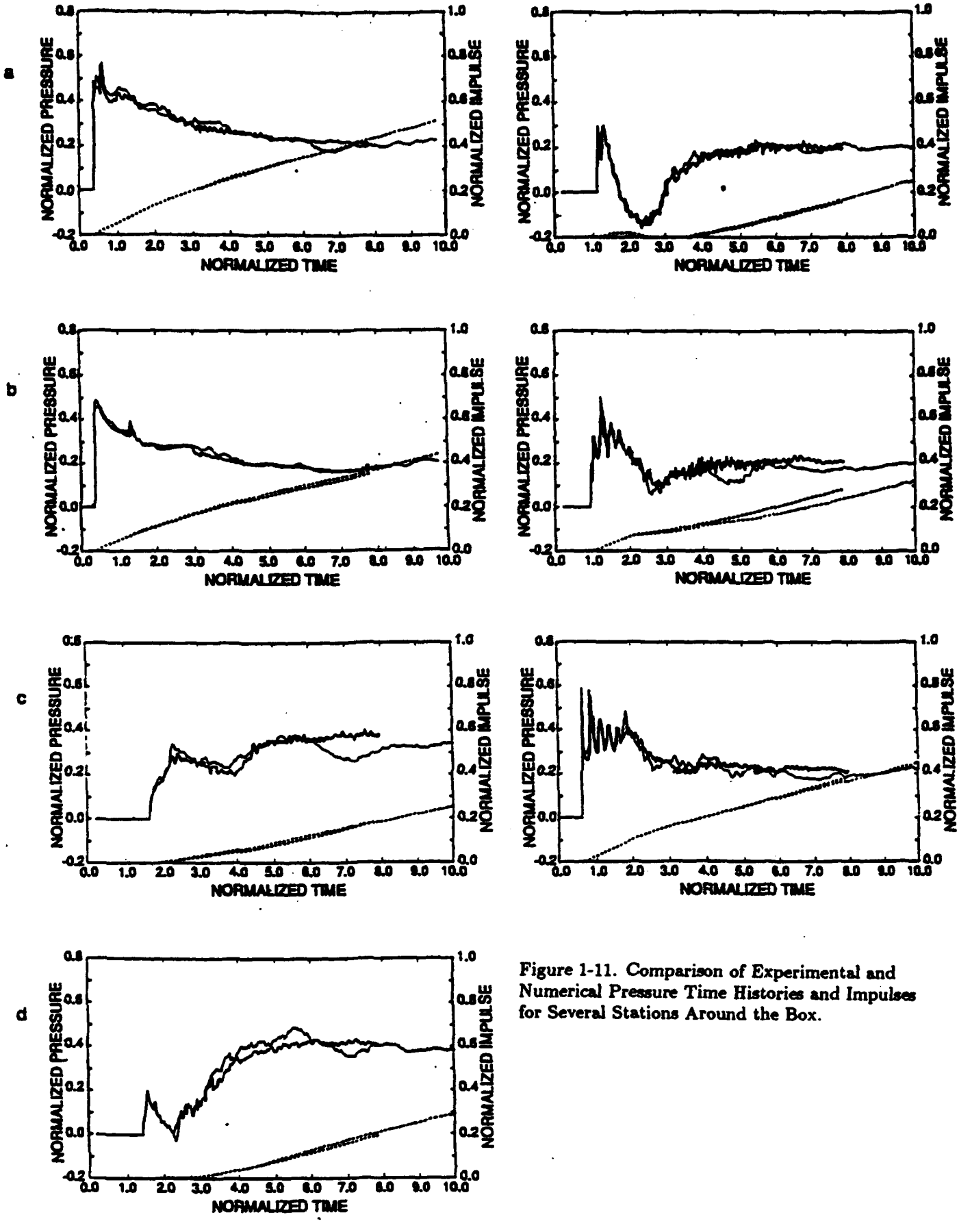

Figure 1-11. Comparison of Experimental and Numerical Pressure Time Histories and Impulses for Several Stations Around the Box.

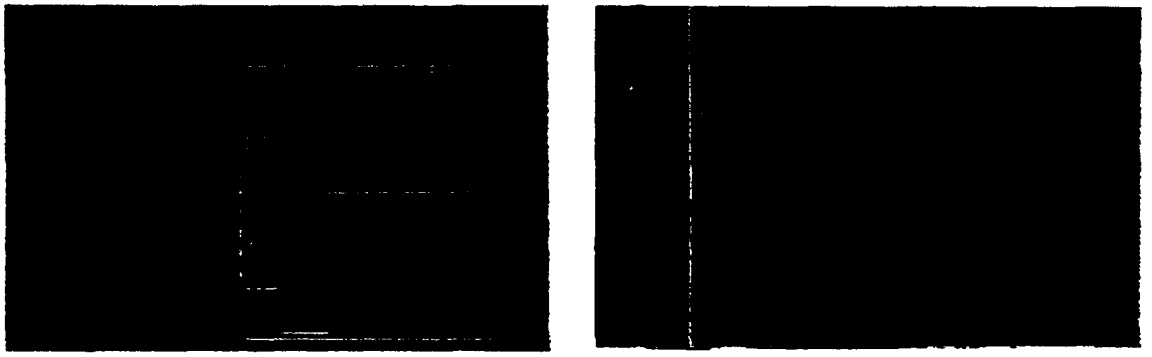

Figure 2-1a-b. Pressure Contours at t=0.0 for the Complete Computational Domain and for an Expanded View of Two Grills.

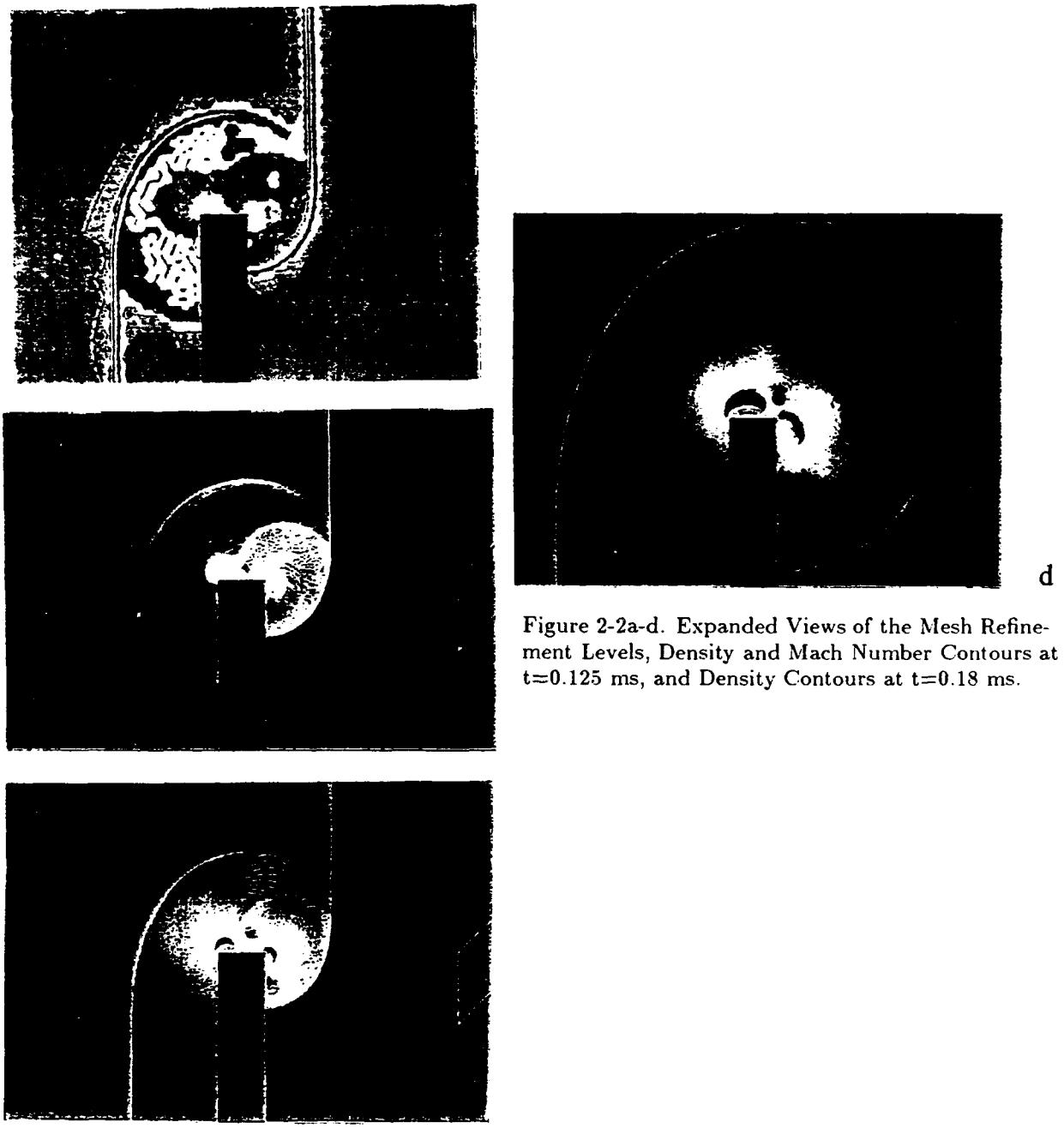

Figure 2-2a-d. Expanded Views of the Mesh Refinement Levels, Density and Mach Number Contours at t=0.125 ms, and Density Contours at t=0.18 ms.

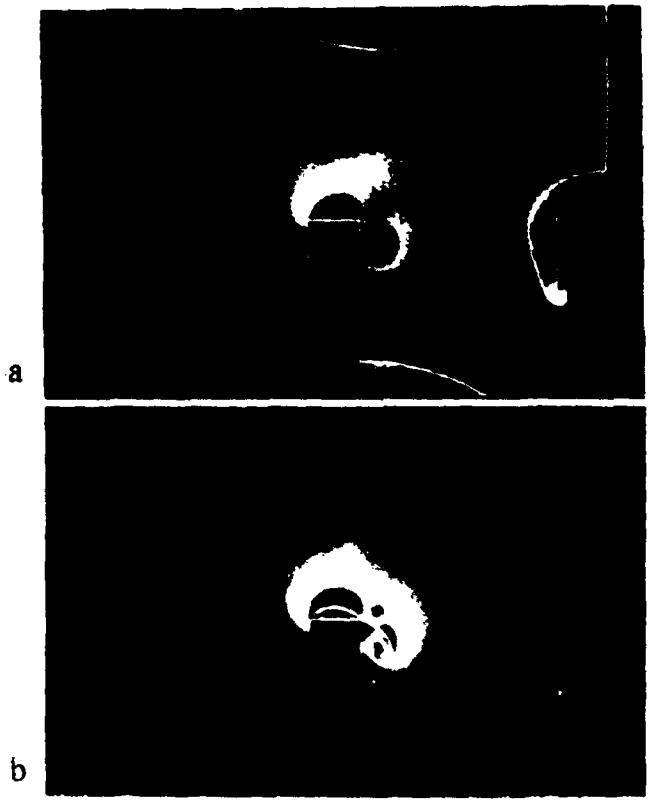

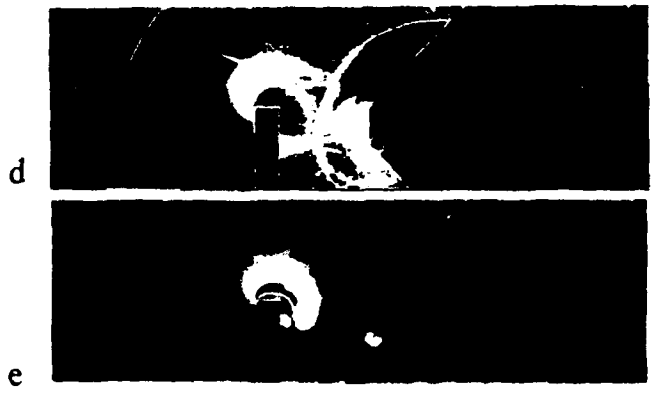

Figure 2-3a-e. Expanded Views of the Density and Mach Number Contours at t=0.21 ms, Density Contours at t=0.245 ms, and Density and Mach Number Contours at t=0.27 ms.

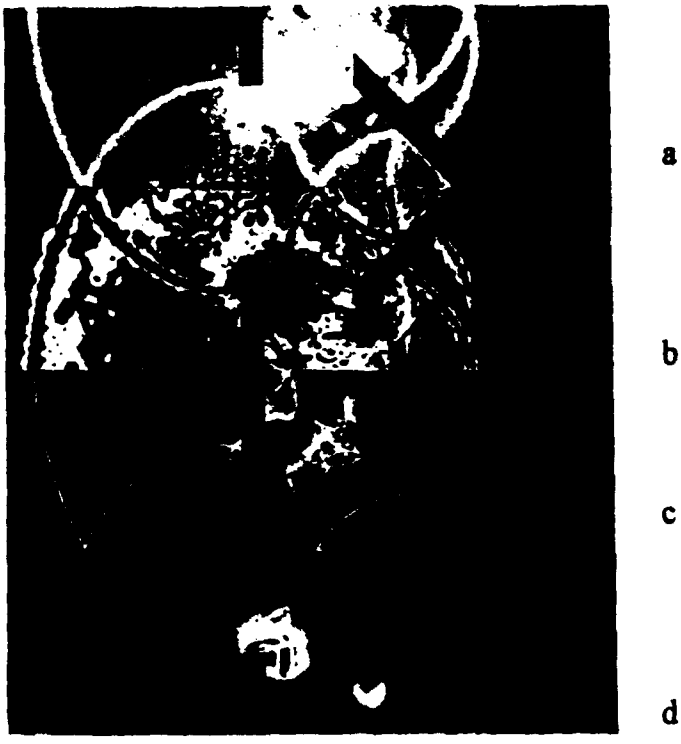

Figure 2-4a-d. Expanded Views of the Computational Mesh, Mesh Refinement Levels, Density and Mach Number Contours at t=0.35 ms.

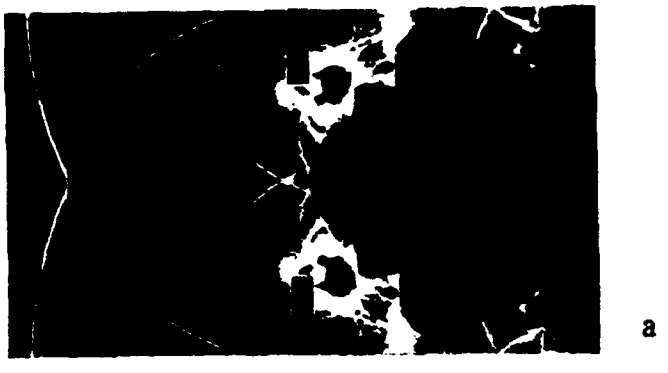

Figure 2-5a. Expanded Views of the Density Contours at t=0.45 ms.

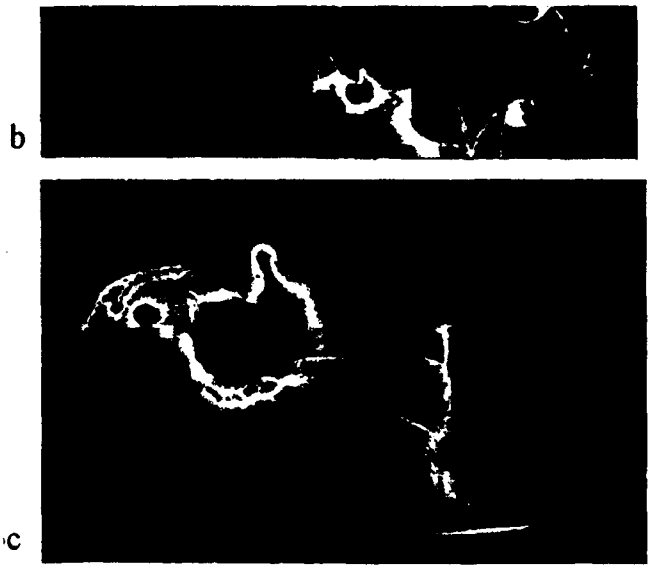

Figure 2-5b-c. Density Contours at t=0.50 ms, and Close Up Density Contours at t=0.50 ms.

Figure 2-6a-d. Expanded Views of the Computational Mesh, Mesh Refinement Levels, Density and Mach Number Contours at t=0.60 ms.

Figure 2-7. Expanded View of the Density Contours at t=0.65 ms.

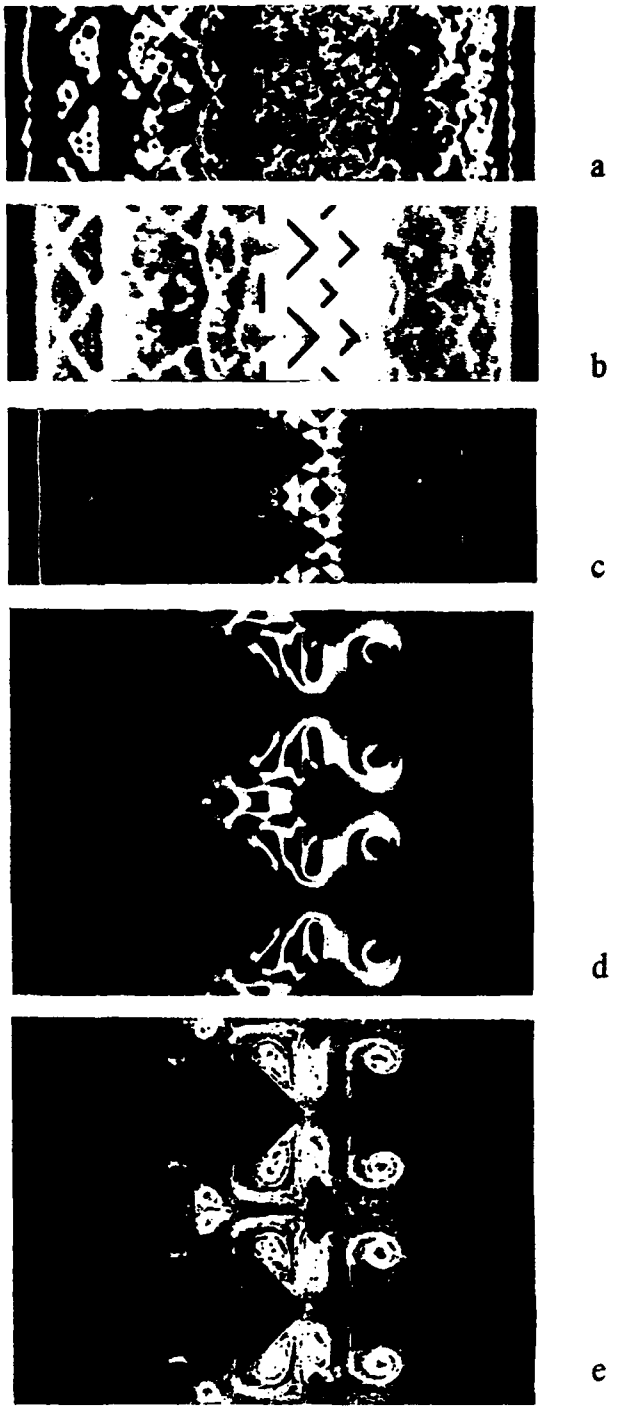

Figure 2-8a-e. Expanded Views of the Mesh Refinement Levels, Computational Mesh, Density, Mach Number and Vorticity Contours at t=1.90 ms.

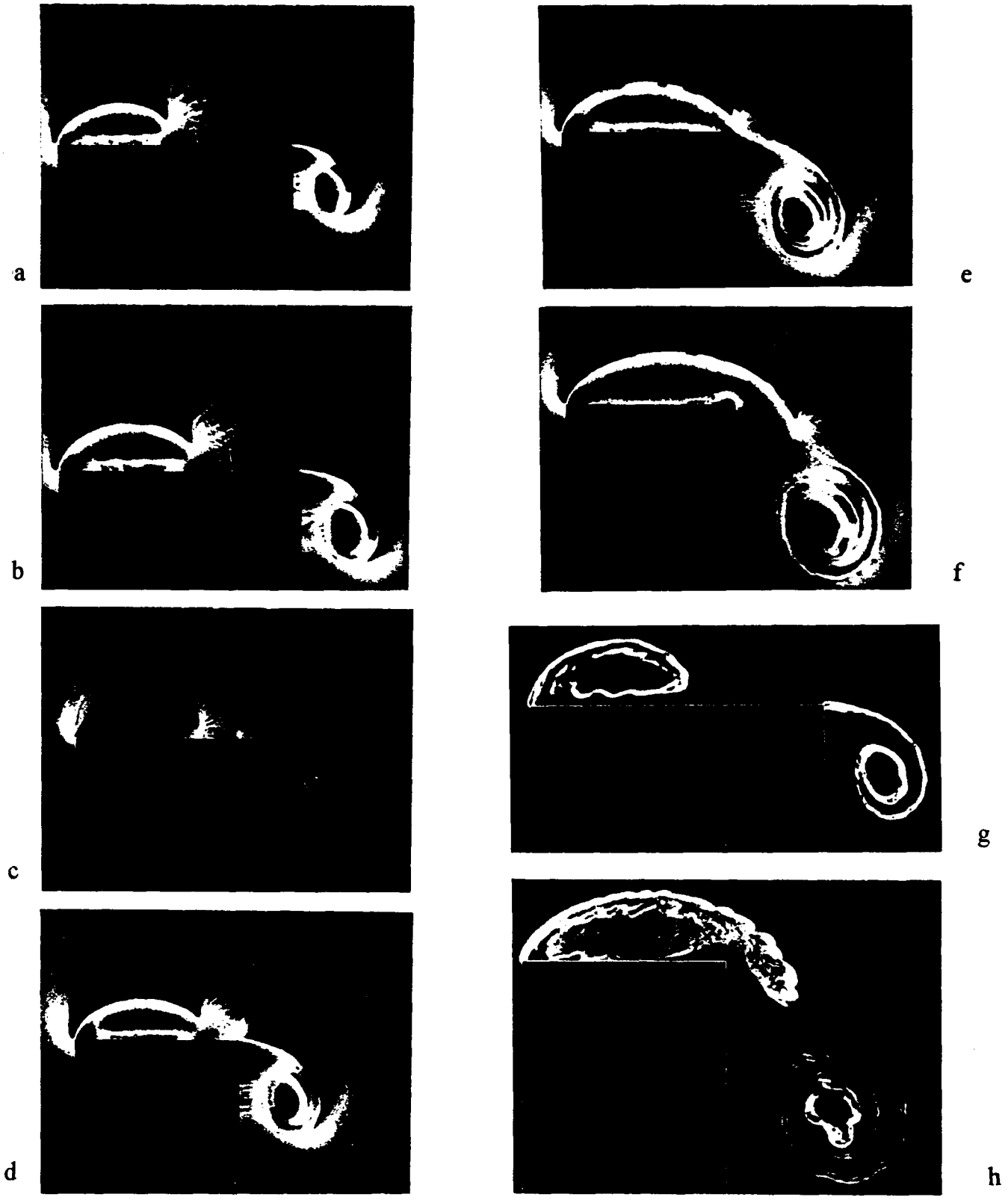

Figure 2-9a-h. Expanded Views of the Flow Near the Tip of the Front Bar: Mach Number Contours at t=0.1375 ms and t=0.15 ms.

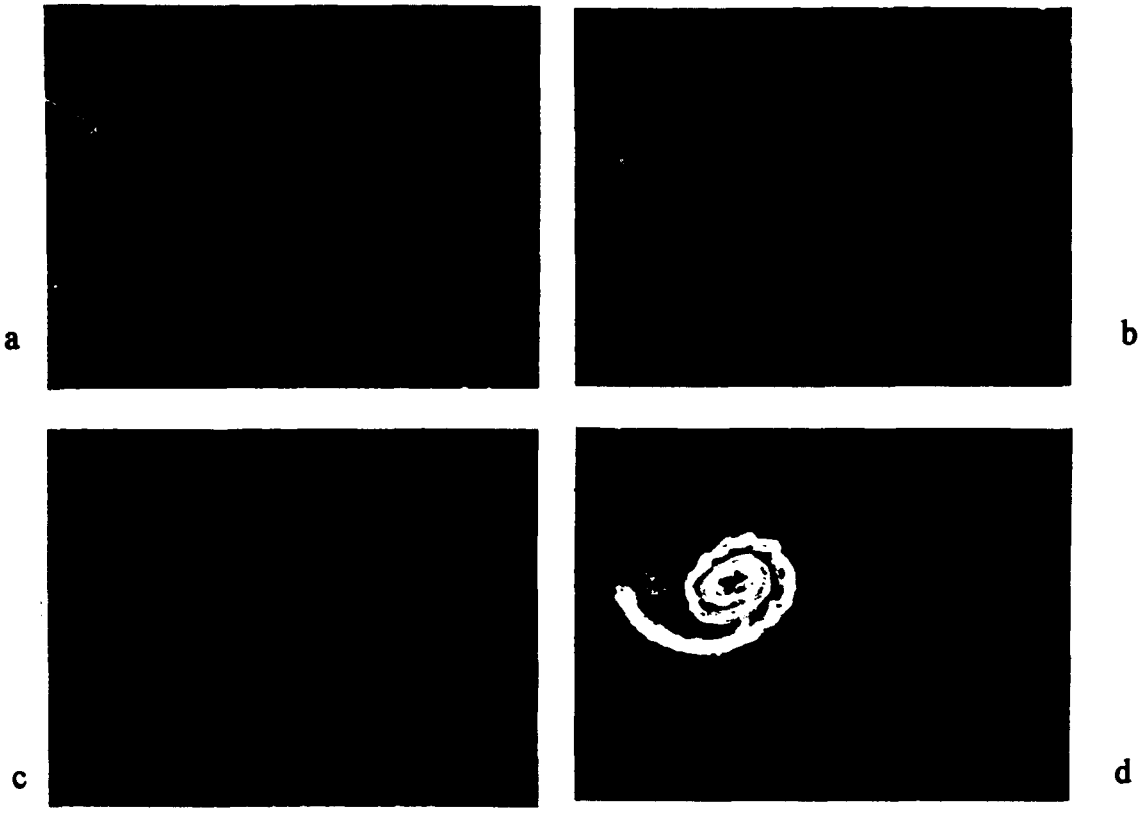

Figure 2-10a-d. Expanded Views of the Flow Near the Upstream Corner of the First Chevron: Density Contours at t=0.30 ms, t=0.35 ms, and Density and Vorticity Contours at t=0.50 ms.

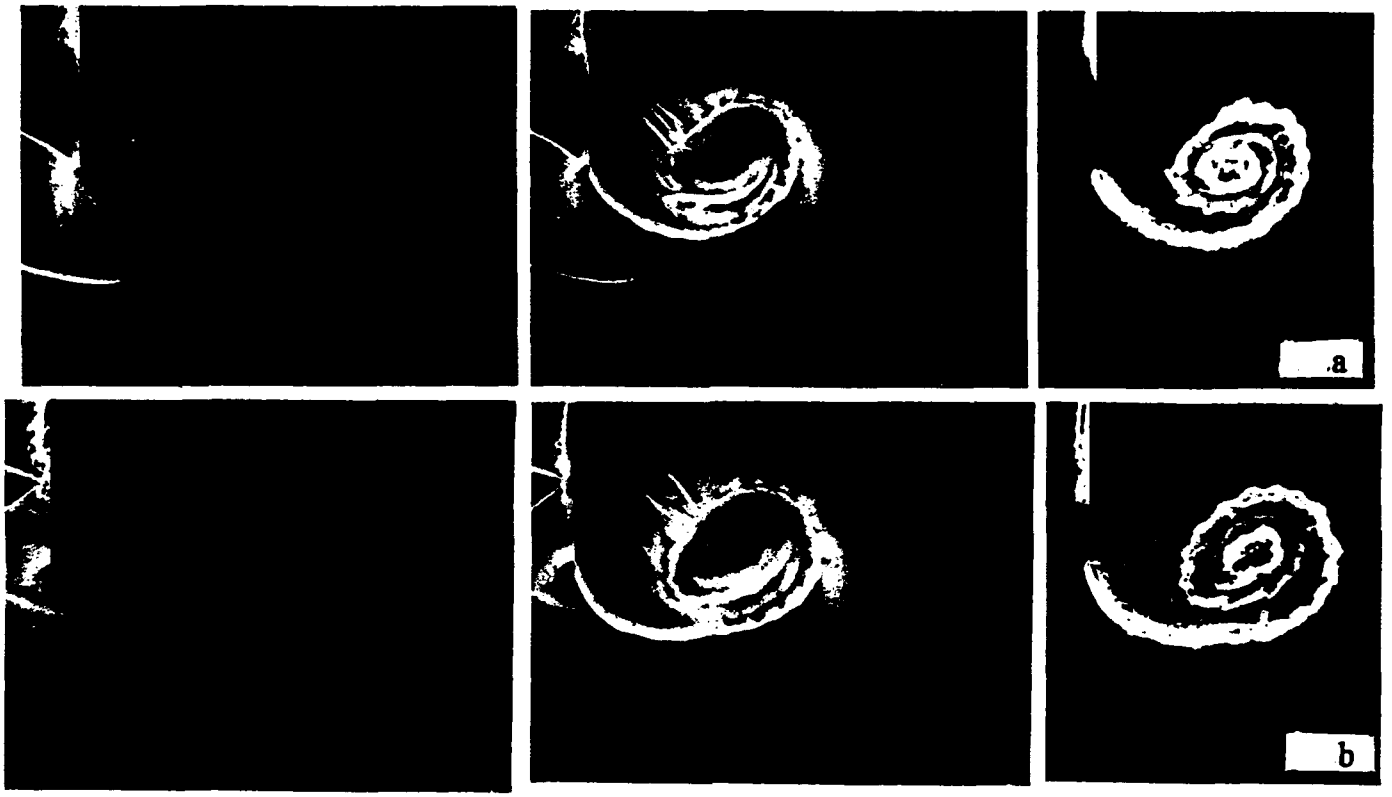

Figure 2-11a-g. Expanded Views of the Flow Near the Upstream Corner of the First Chevron: Density, Mach Number and Vorticity Contours at t=0.45 ms, t=0.48 ms, t=0.49 ms, t=0.50 ms, t=0.51 ms, t=0.55 ms, and t=0.60 ms.

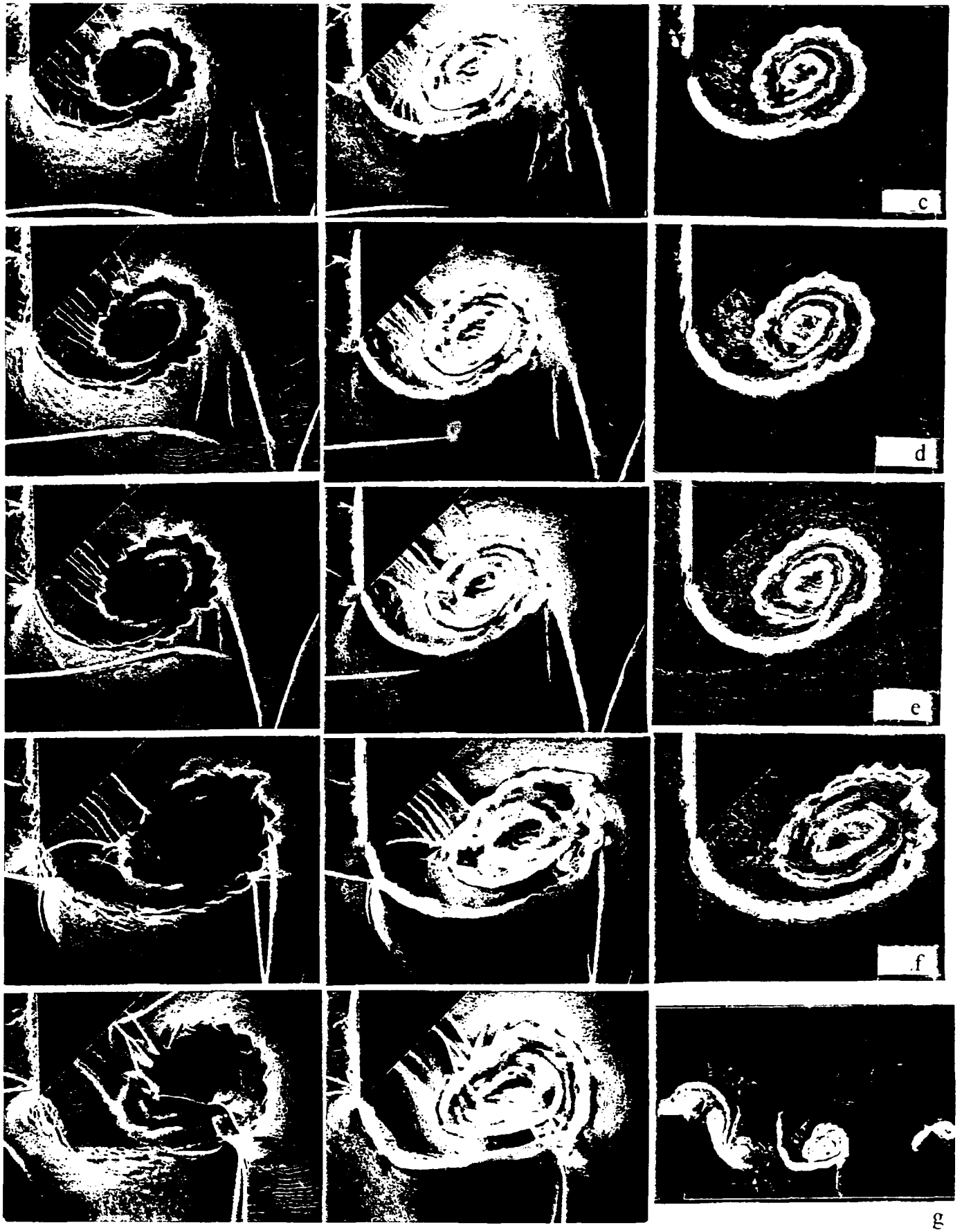

Figure 2 11a-g (Continued)

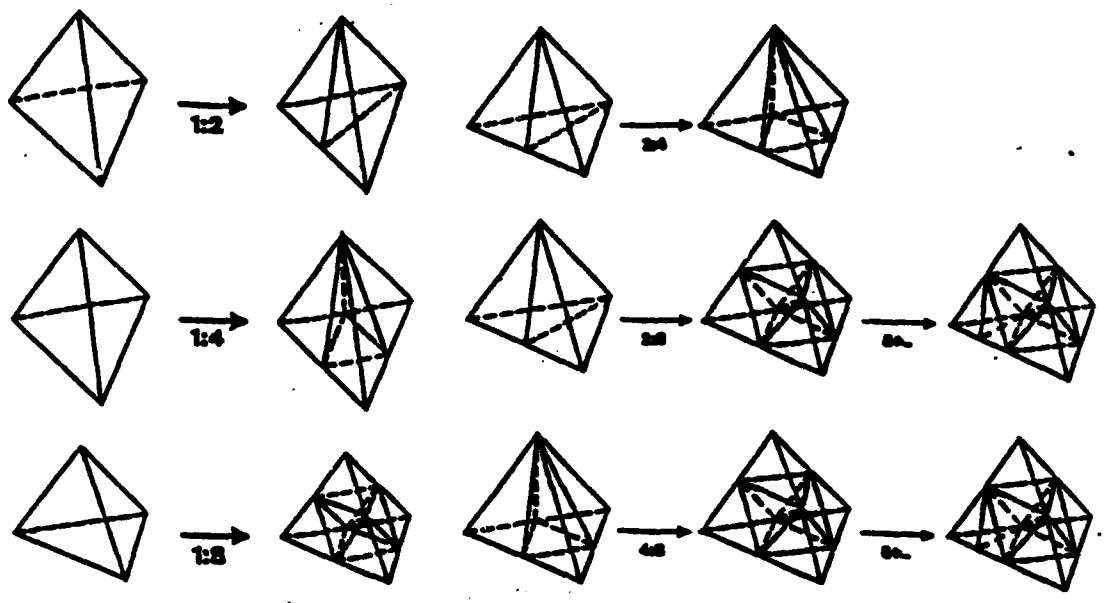

Figure 3-1. Refinement Cases

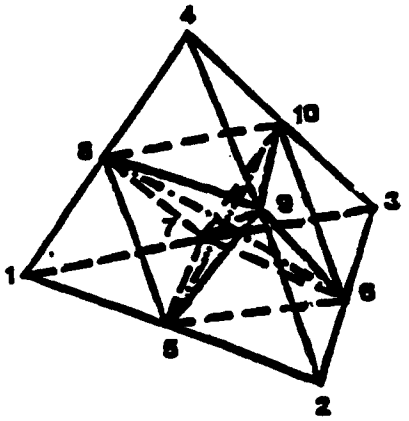

Figure 3-2. Possible Choices for 'Inner Diagonals'

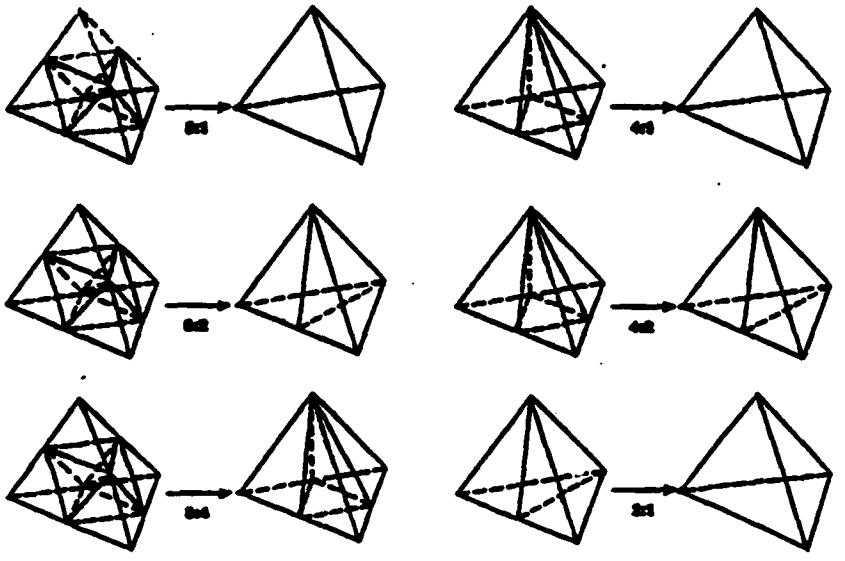

Figure 3-3. De-Refinement Cases

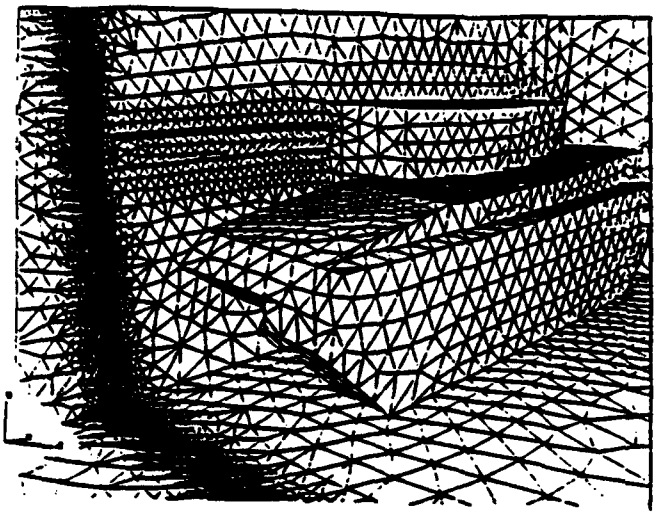

Figure 3-4. Expanded View of Superimposed Adapted Computational Mesh and Pressure Contours on the Boundaries, t=0.0 ms.

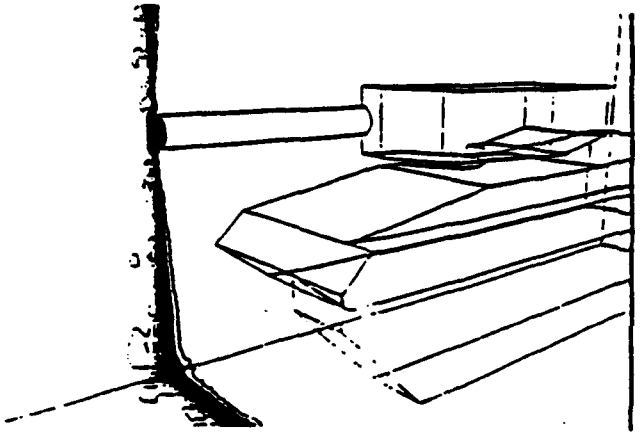

Figure 3-5. Expanded View of Pressure Contours on the Boundaries, t=3.0.

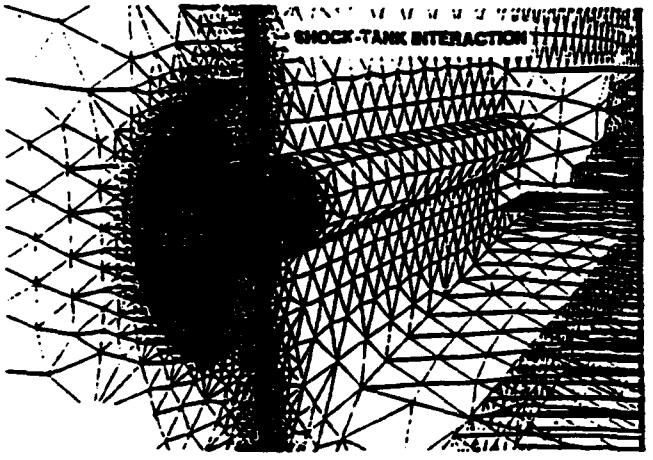

Figure 3-6a. Expanded View of Superimposed Adapted Computational Mesh and Pressure Contours on the Plane of Symmetry, t=4.2 ms.

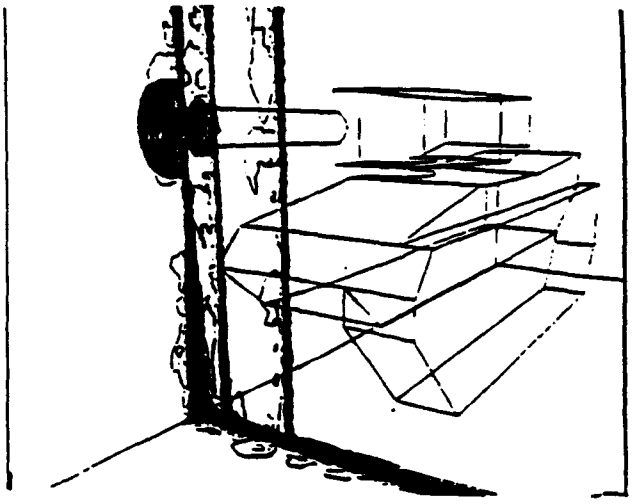

Figure 3-6b. Superimposed Pressure Contours on the Boundaries with Pressure Contours on Two X-Y Planes (at Z=0.5 m and Z=1.5 m), t=4.2 ms.

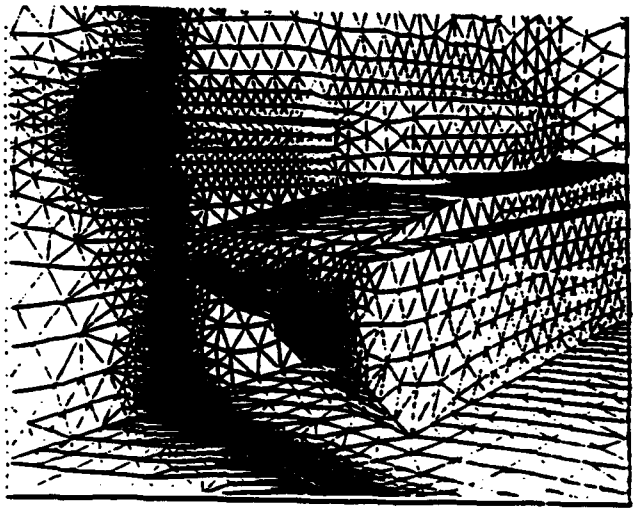

Figure 3-7a. Expanded View of Superimposed Adapated Computational Mesh and Pressure Contours on the Boundaries, t=5.5 ms.

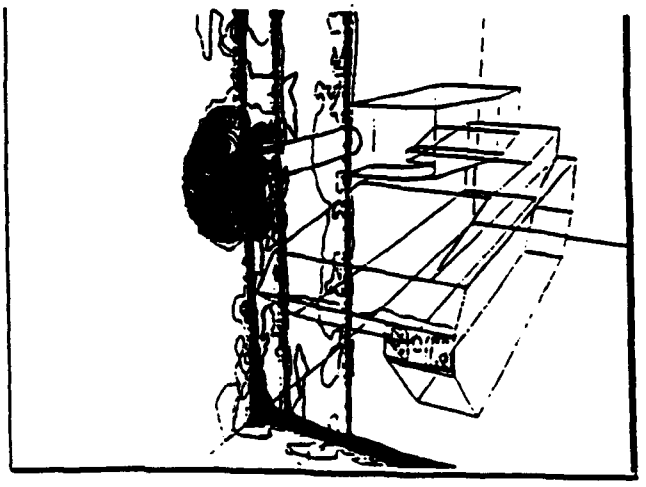

Figure 3-7b. Superimposed Pressure Contours on the Boundaries with Pressure Contours on Two X-Y Planes (at Z=0.5 m and Z=1.5 m), t=5.5 ms.

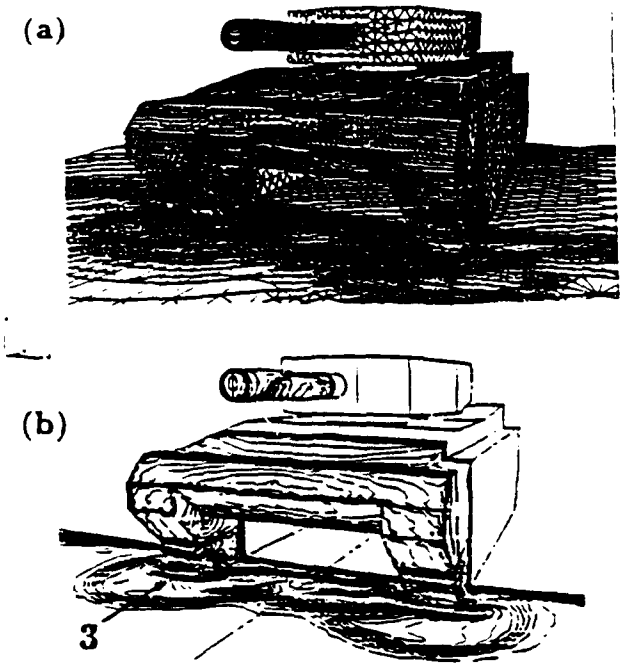

Figure 3-8a-b. Adapted Computational Mesh (a) and Pressure Contours (b) on the Tank Surface, t=9.67 ms.

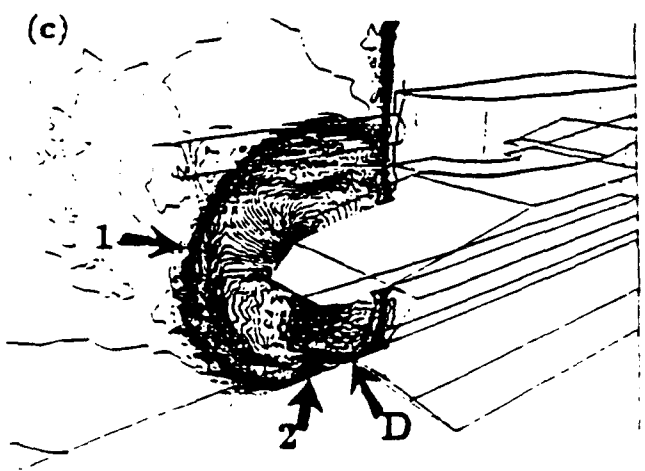

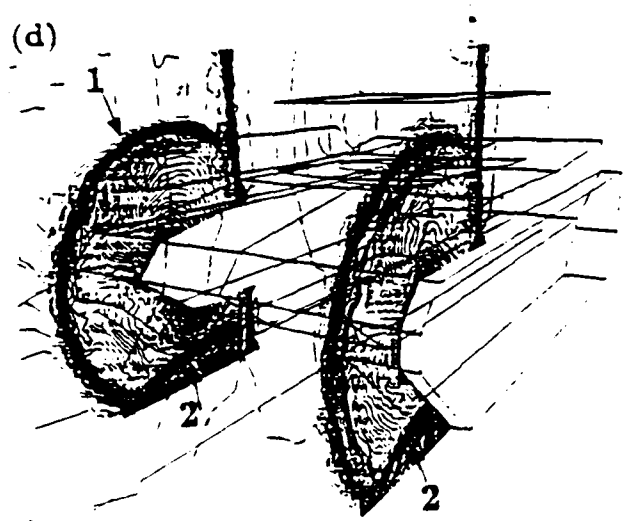

Figure 3-8c-d. Pressure Contours on X-Y Planes Located at: (c) Z=0.5 m, (d) Z=1.5 m (left) and Z=2.75 m (right), t=9.67 ms.

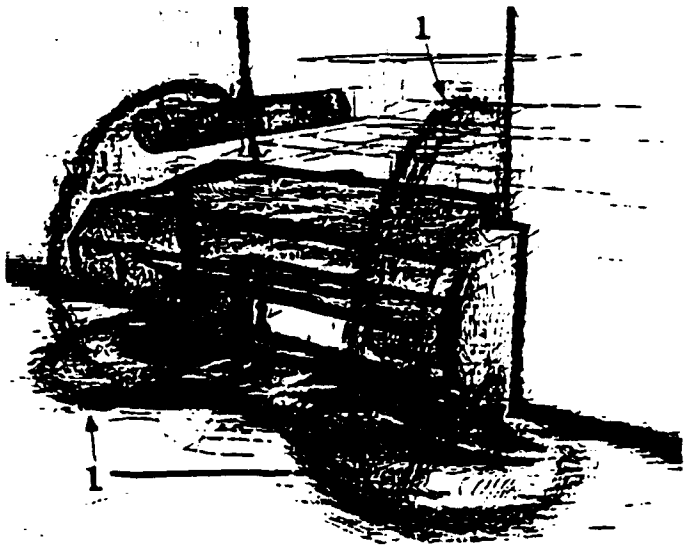

Figure 3-8e. Superimposed Pressure Contours on the Tank Surface with Pressure Contours on Two X-Y Planes at Z=1.5 m (left) and Z=2.75 m (right), t=9.67 ms.

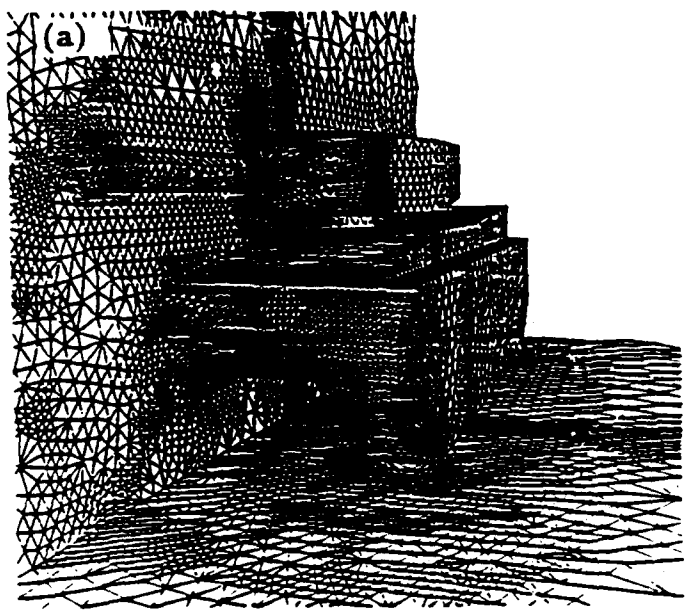

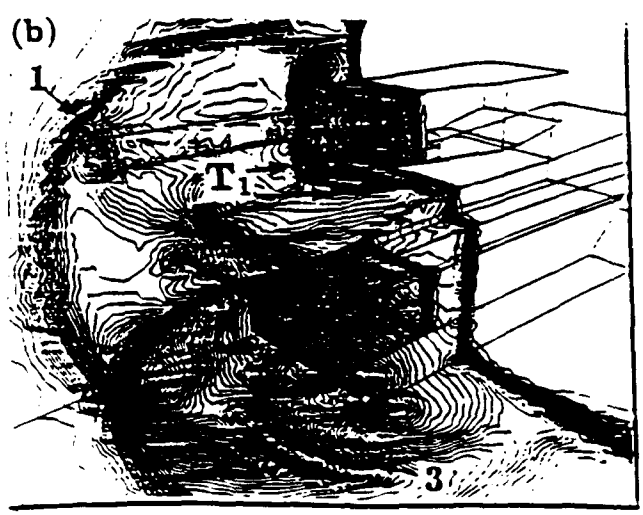

Figure 3-9a-b. Adapted Computational Mesh (a) and Pressure Contours (b) on the Tank Surface, t=12.87 ms.

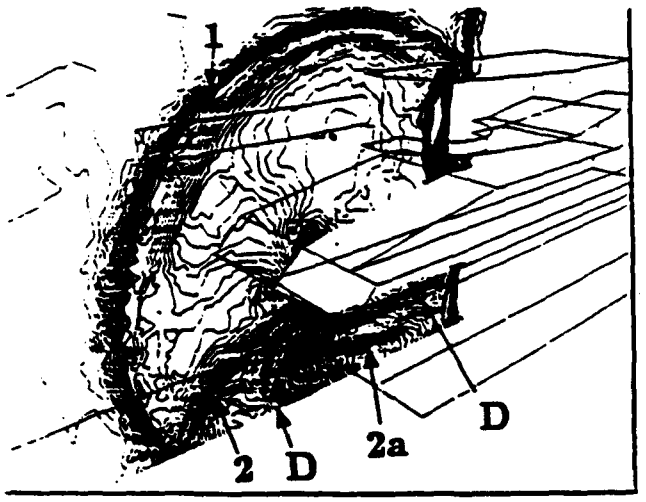

Figure 3-9c. Pressure Contours on a X-Y Plane, Z=0.5 m, t=12.87 ms.

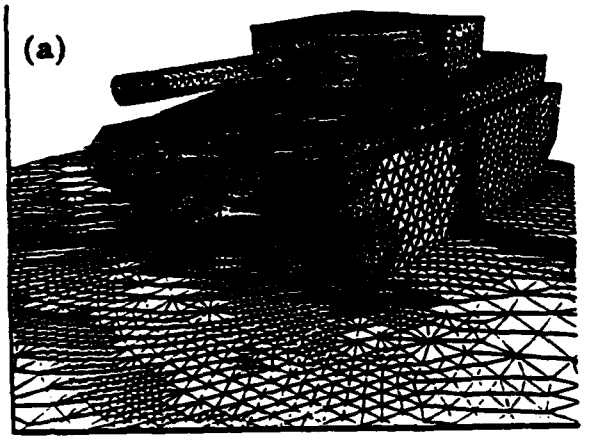

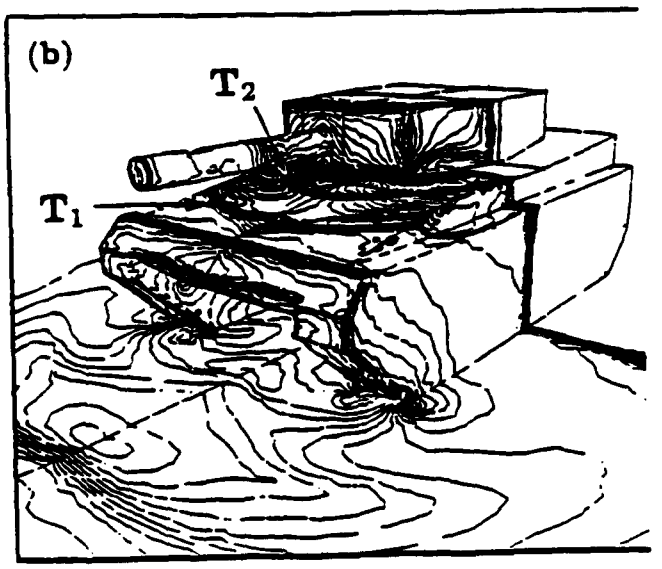

Figure 3-10a-b. Adapted Computational Mesh (a) and Pressure Contours (b) on the Tank Surface, t=15.53 ms.

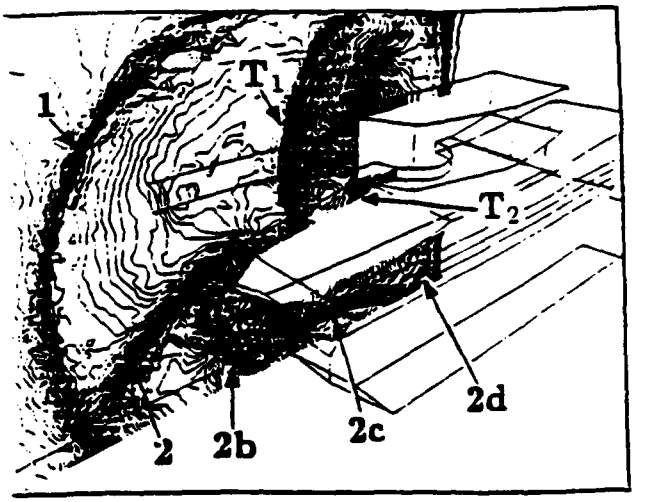

Figure 3-10c. Pressure Contours on a X-Y Plane, Z=0.5 m, t=15.53 ms.

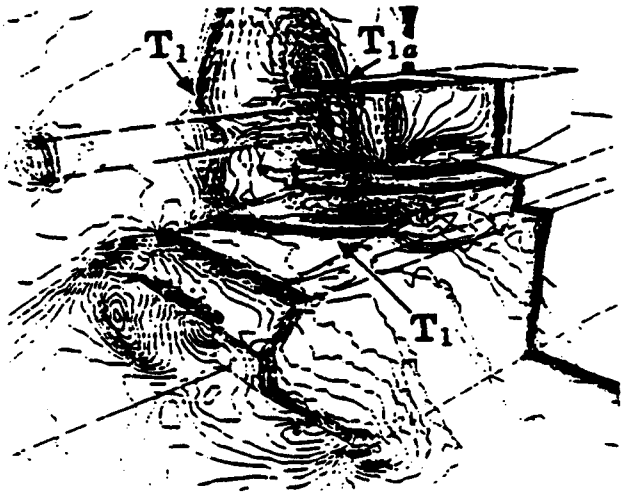

Figure 3-11. Superimposed Pressure Contours on the Tank Surface and Pressure Contours on a Y-Z Plane at Z=2.0 m, t=15.53 ms.

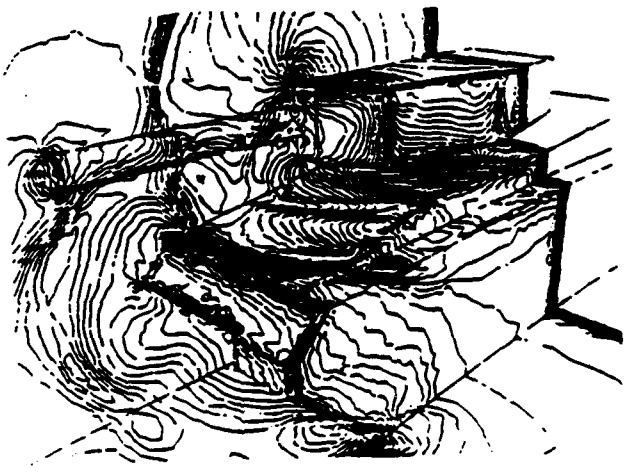

Figure 3-12a. Pressure Contours on the Tank Surface, t=19.69 ms.

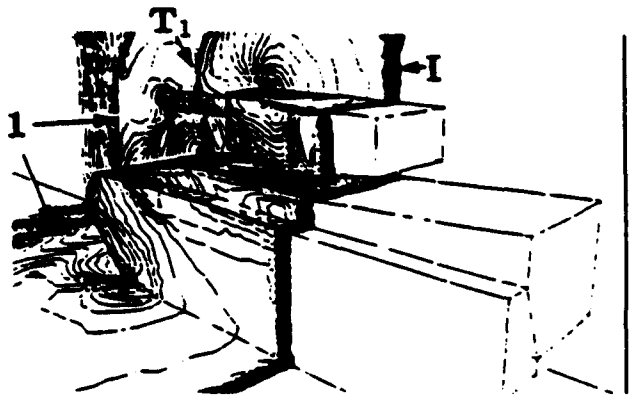

Figure 3-12b. Pressure Contours on the Boundaries, a View from the Back, t=19.69 ms.

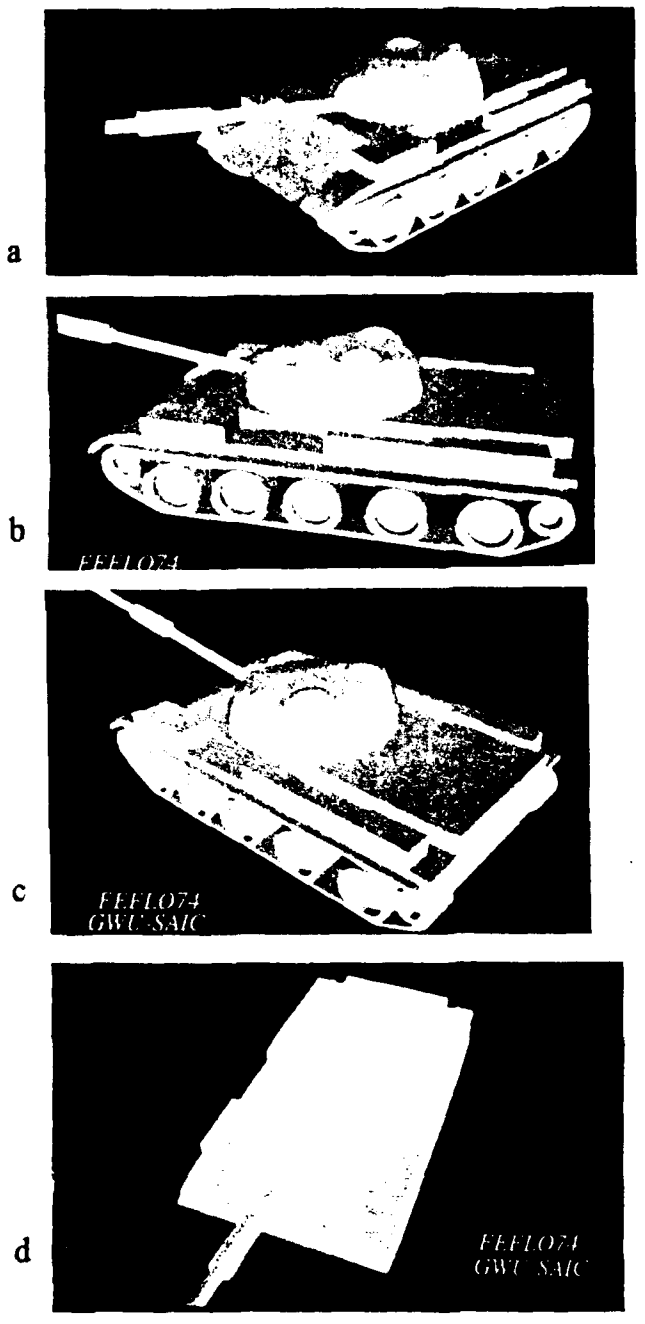

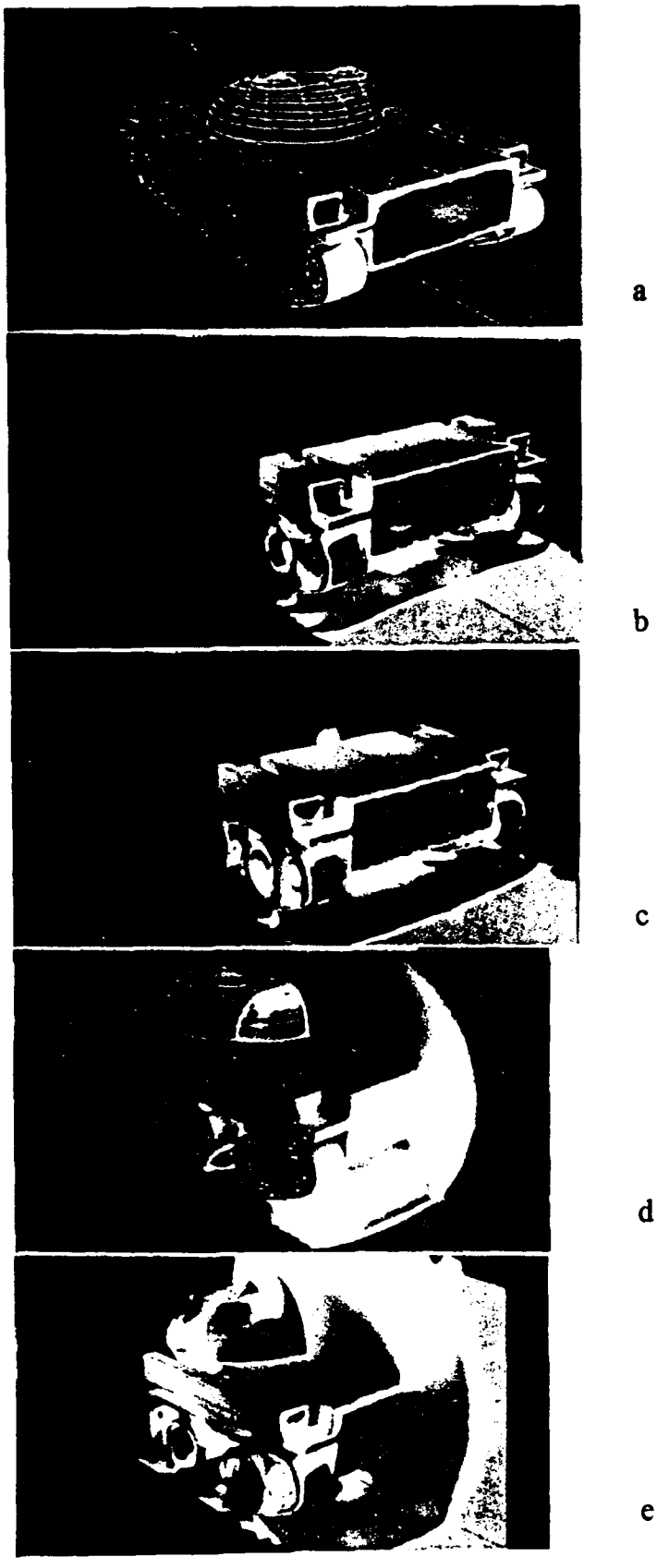

Figure 3-13a-c. Solid Body Modeling of a Modern Main Battlefield Tank; Several Views Around the Tank. Figure 3-13d. Surface Triangulation of the Tank.

Figure 3-14a-e. Pressure Contours on the Tank Surfaces at 200, 400, 600, 800, and 1000 Time Steps, Respectively.

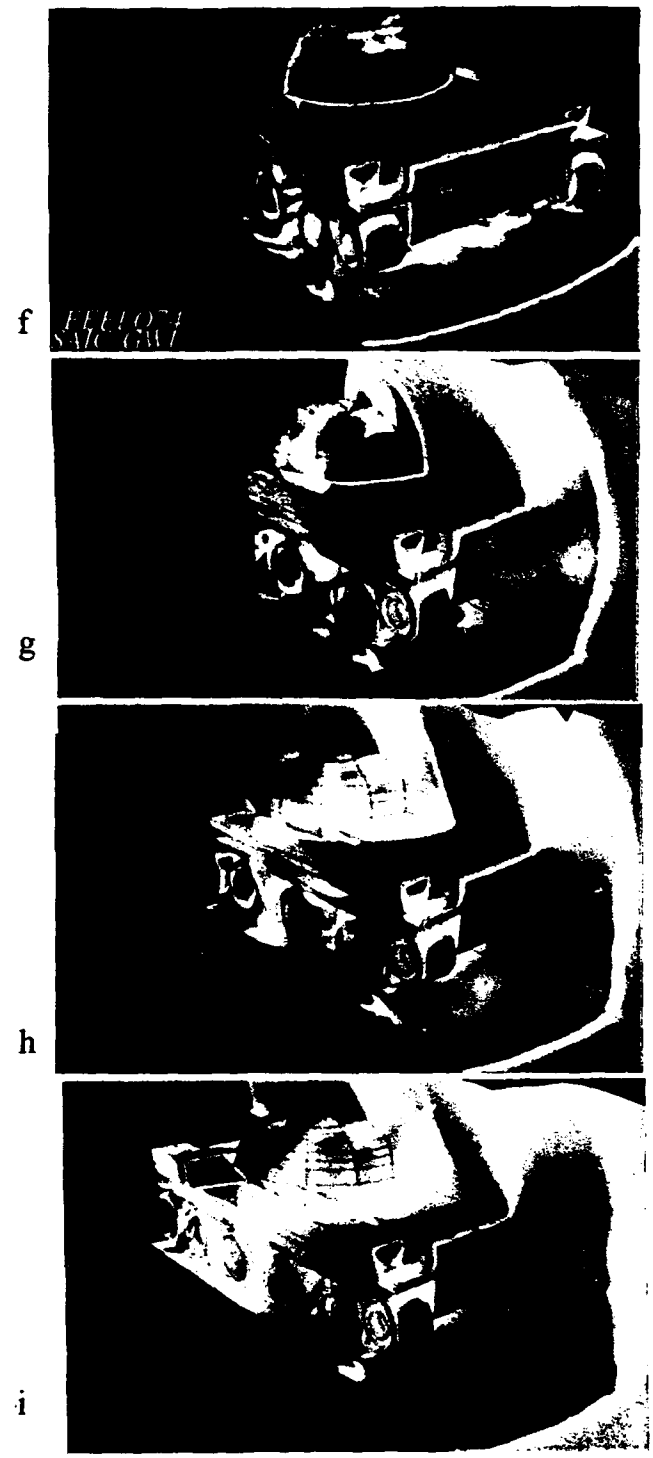

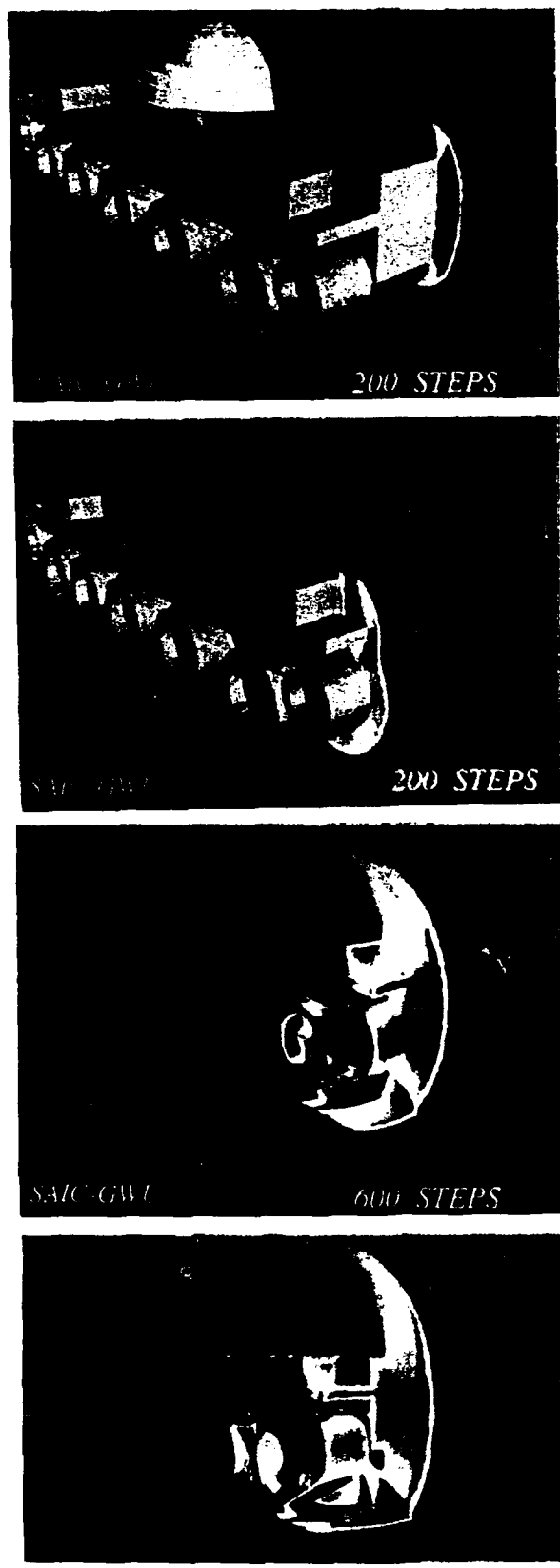

Figure 3-14f-i. Pressure Contours on the Tank Surfaces at 1200, 1400, 2000 and 2800 Time Steps, Respectively.

Figure 3-15a-d. Pressure Contours on Several X-Y Planes: a) Z=0.5 m, 200 Steps; b) Z=1.5 m, 200 Steps; c) Z=1.5 m, 600 Steps; d) Z=1.0 m, 800 Steps.

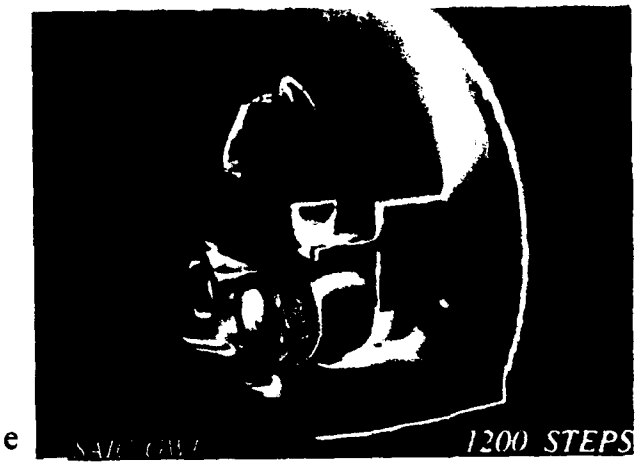

e

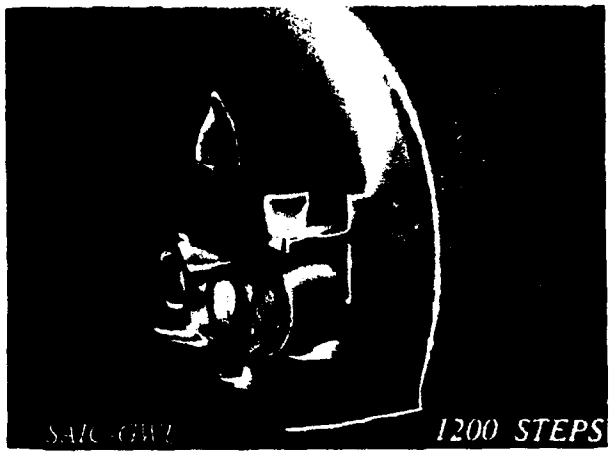

f

g

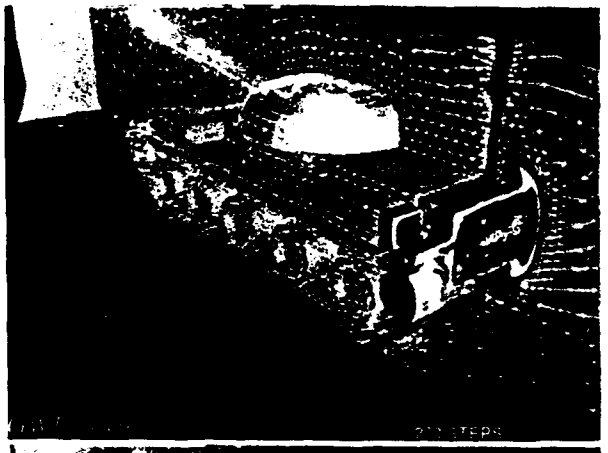

a

b

c

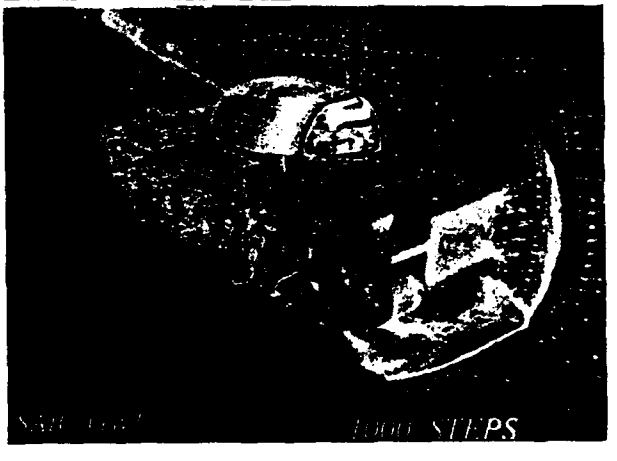

d

Figure 3-15e-g. Pressure Contours on Several X-Y Planes: e) Z=0.5 m, 1200 Steps; f) Z=1.0 m, 1200 Steps; g) Z=1.5 m, 1200 Steps.

Figure 3-16a-d. Superposition of Pressure Contours and Adapted Grids on the Tank Surface, Back Impact, at 200, 400, 600 and 1000 Time Steps, Respectively.

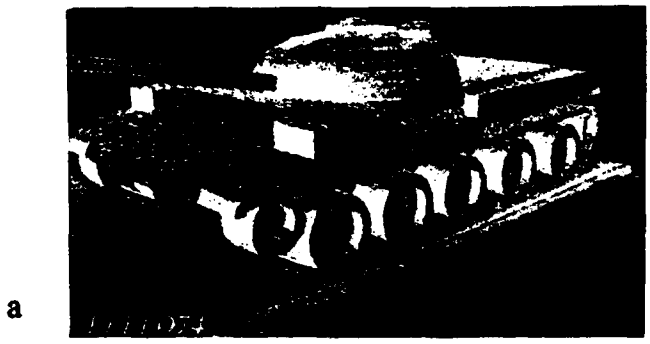

a

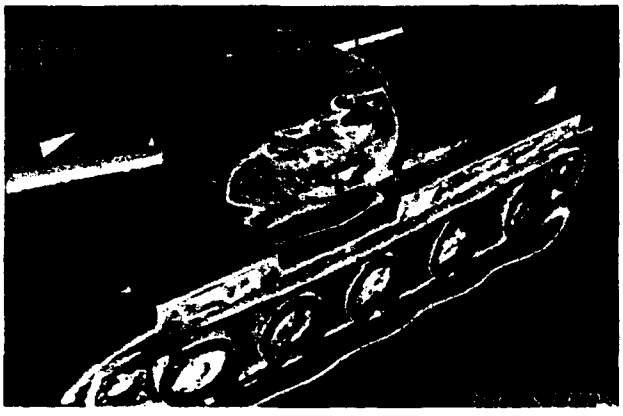

b

c

Figure 3-17a-c. Superposition of Pressure Contours and Adapted Grids on the Tank Surface, Side Impact, at 0, 300, and 600 Time Steps, Respectively.

a

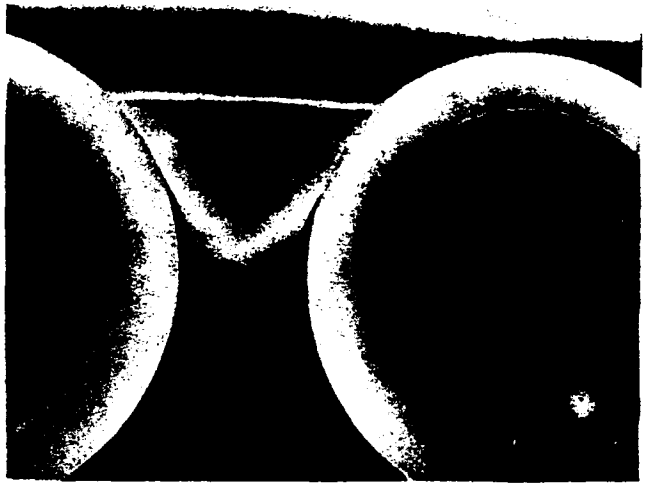

b

c

d

Figure 3-18a-d. Pressure Contours on the Tank Surfaces: a) Tank, 300 Time Steps; b) Expanded View Between the Wheels, 300 Time Steps; c) Tank, 600 Time Steps; d) Tank, 800 Time Steps.

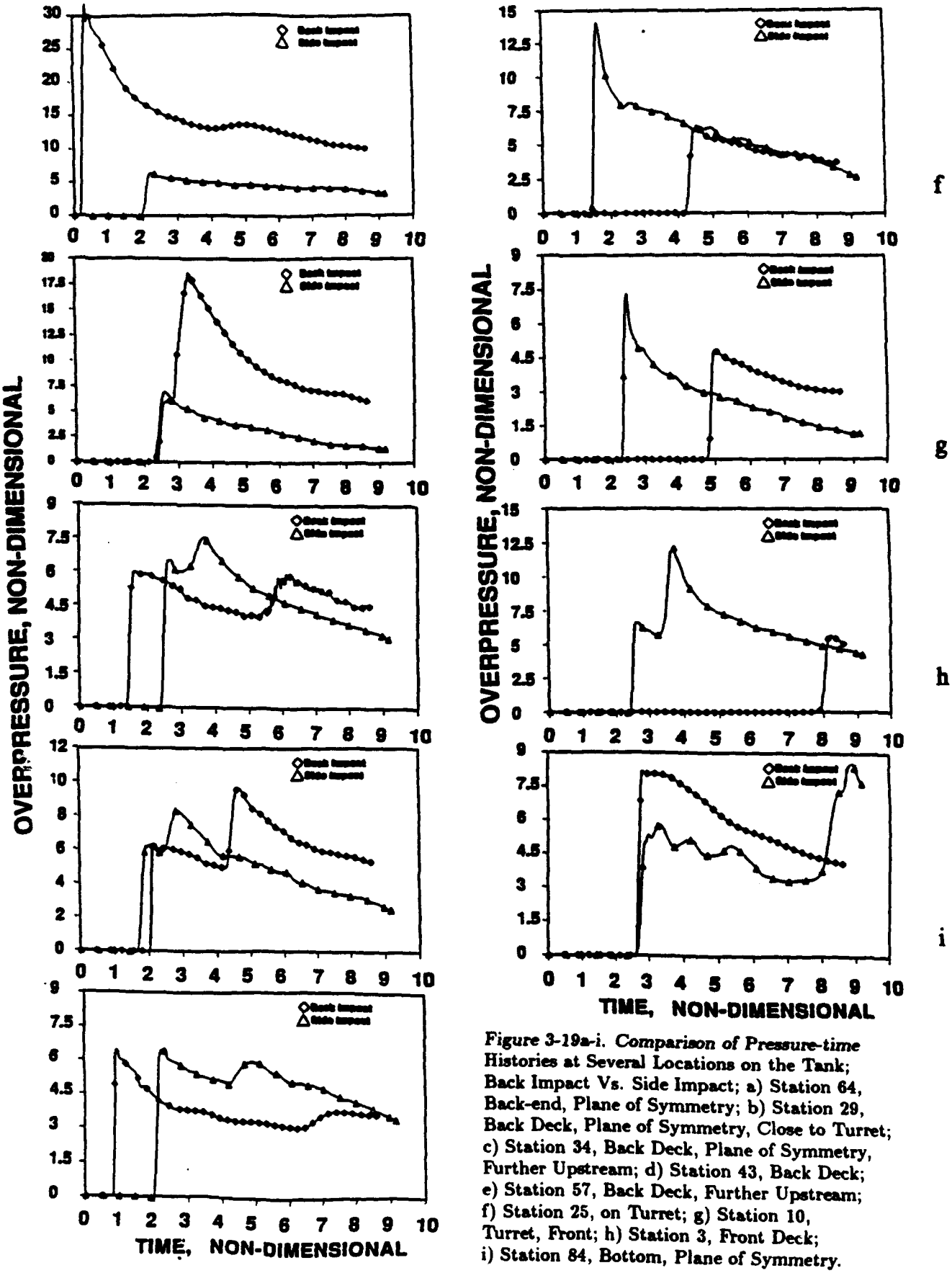

Figure 3-19a-i. Comparison of Pressure-time Histories at Several Locations on the Tank; Back Impact Vs. Side Impact; a) Station 64, Back-end, Plane of Symmetry; b) Station 29, Back Deck, Plane of Symmetry, Close to Turret; c) Station 34, Back Deck, Plane of Symmetry, Further Upstream; d) Station 43, Back Deck; e) Station 57, Back Deck, Further Upstream; f) Station 25, on Turret; g) Station 10, Turret, Front; h) Station 3, Front Deck; i) Station 84, Bottom, Plane of Symmetry.

DISTRIBUTION LIST

DNA-TR-93-4

DEPARTMENT OF DEFENSE

ASSISTANT TO THE SECRETARY OF DEFENSE
ATTN: EXECUTIVE ASSISTANT

DEFENSE INTELLIGENCE AGENCY
ATTN: DIW-4
ATTN: PAA-1A G WEBER

DEFENSE NUCLEAR AGENCY
ATTN: SPSD
ATTN: SPWE DR C GALLOWAY
ATTN: TDTR
2 CY ATTN: TITL

DEFENSE TECHNICAL INFORMATION CENTER
2 CY ATTN: DTIC/OC

FIELD COMMAND DEFENSE NUCLEAR AGENCY
ATTN: FCTO
ATTN: FCTT G BALADI
ATTN: W SUMMA

DEPARTMENT OF THE ARMY

ARMY RESEARCH LABORATORIES
ATTN: AMSRL-SL-CE

DEP CH OF STAFF FOR OPS & PLANS
ATTN: DAMO-NCZ

U S ARMY ATMOSPHERIC SCIENCES LAB
ATTN: SLCAS-AR-M R SUTHERLAND

U S ARMY BALLISTIC RESEARCH LAB
ATTN: SLCBR-SS-T
ATTN: SLCBR-TB-B G BULMASH

U S ARMY ENGR WATERWAYS EXPER STATION
ATTN: C WELCH CEWES-SE-R
ATTN: D RICKMAN CEWES-SE-R
ATTN: E JACKSON CEWES-SD-R
ATTN: F DALLRIVA CEWES-SS-R
ATTN: J BALSARA CEWES-SS-R

U S ARMY NUCLEAR & CHEMICAL AGENCY
ATTN: MONA-NU DR D BASH

DEPARTMENT OF THE NAVY

NAVAL RESEARCH LABORATORY
ATTN: CODE 5227 RESEARCH REPORT

NAVAL SURFACE WARFARE CENTER
ATTN: L VALGE

NAWCWPNSDIV DETACHMENT
ATTN: CLASSIFIED LIBRARY

OFFICE OF CHIEF OF NAVAL OPERATIONS
ATTN: NUC AFFAIRS & INT'L NEGOT BR

DEPARTMENT OF THE AIR FORCE

AERONAUTICAL SYSTEMS CENTER
ATTN: ENSSS H GRIFFIS

AIR UNIVERSITY LIBRARY
ATTN: AUL-LSE

HQ USAF/XOFN
ATTN: XOFN

PHILLIPS LABORATORY
ATTN: PL/WS MR SHARP

DEPARTMENT OF ENERGY

LAWRENCE LIVERMORE NATIONAL LAB
ATTN: PAUL GUDIKSEN
ATTN: R PERRETT

LOS ALAMOS NATIONAL LABORATORY
ATTN: A S MASON
ATTN: J NORMAN
ATTN: R W SELDEN
ATTN: R W WHITAKER
ATTN: B SHAFER

SANDIA NATIONAL LABORATORIES
ATTN: A CHABAI DIV 9311

OTHER GOVERNMENT

CENTRAL INTELLIGENCE AGENCY
ATTN: OSWR/NED
ATTN: OSWR S WALLENHORST

DEPARTMENT OF DEFENSE CONTRACTORS

AEROSPACE CORP
ATTN: P RAUSCH

AEROTHERM CORP
ATTN: C NARDO

APPLIED RESEARCH ASSOCIATES, INC
ATTN: J KEEFER

APTEK, INC
ATTN: T MEAGHER

CALSPAN CORP
ATTN: M DUNN
ATTN: M HOLDEN

CARPENTER RESEARCH CORP
ATTN: H J CARPENTER

G B LABORATORY, INC
ATTN: G BURGHART

GENERAL ATOMICS, INC
ATTN: CHARLES CHARMAN

GENERAL ELECTRIC CO
ATTN: B MAGUIRE

GENERAL RESEARCH CORP
ATTN: W ADLER

H & H CONSULTANTS, INC
ATTN: W HALL

HERCULES, INC, HERCULES
ATTN: P MCALLISTER

HORIZONS TECHNOLOGY, INC
ATTN: B KREISS
ATTN: B LEE

INSTITUTE FOR DEFENSE ANALYSES
ATTN: CLASSIFIED LIBRARY
ATTN: E BAUER

JAYCOR
ATTN: CYRUS P KNOWLES

KAMAN SCIENCES CORP
ATTN: T STAGLIANO

KAMAN SCIENCES CORP
ATTN: JOHN KEITH

KAMAN SCIENCES CORP
ATTN: D MOFFETT
ATTN: DASIAC
4 CY ATTN: J NYDEN

KAMAN SCIENCES CORPORATION
ATTN: DASIAC

LOCKHEED MISSILES & SPACE CO, INC
ATTN: R K JAMISON
ATTN: T J KELIHER

LOGICON R & D ASSOCIATES
ATTN: R ROSS
ATTN: T A MAZZOLA

LOGICON R & D ASSOCIATES
ATTN: G GANONG

LOGICON R & D ASSOCIATES
ATTN: J WEBSTER

PACIFIC-SIERRA RESEARCH CORP
ATTN: R SMALL

S-CUBED
ATTN: C NEEDHAM

SCIENCE APPLICATIONS INTL CORP
ATTN: J STODDARD

SCIENCE APPLICATIONS INTL CORP
ATTN: D BACON
ATTN: J COCKAYNE
2 CY ATTN: J D BAUM
ATTN: P VERSTEEGEN
ATTN: W LAYSON

SCIENCE APPLICATIONS INTL CORP
ATTN: A LAGANELLI
ATTN: A MARTELLUCCI
ATTN: J SONTOWSKI

SCIENCE APPLICATIONS INTL CORP
ATTN: J MANSHIP

SOUTHERN RESEARCH INSTITUTE
ATTN: C PEARS

SRI INTERNATIONAL
ATTN: J GIOVANOLA
ATTN: M SANAI

TECH REPS, INC
ATTN: F MCMULLAN

TITAN CORPORATION (THE)
ATTN: P HASIG

TOYON RESEARCH CORP
ATTN: J CUNNINGHAM

WEIDLINGER ASSOC, INC
ATTN: DARREN TENNANT
ATTN: H LEVINE

WEIDLINGER ASSOCIATES, INC
ATTN: M BARON